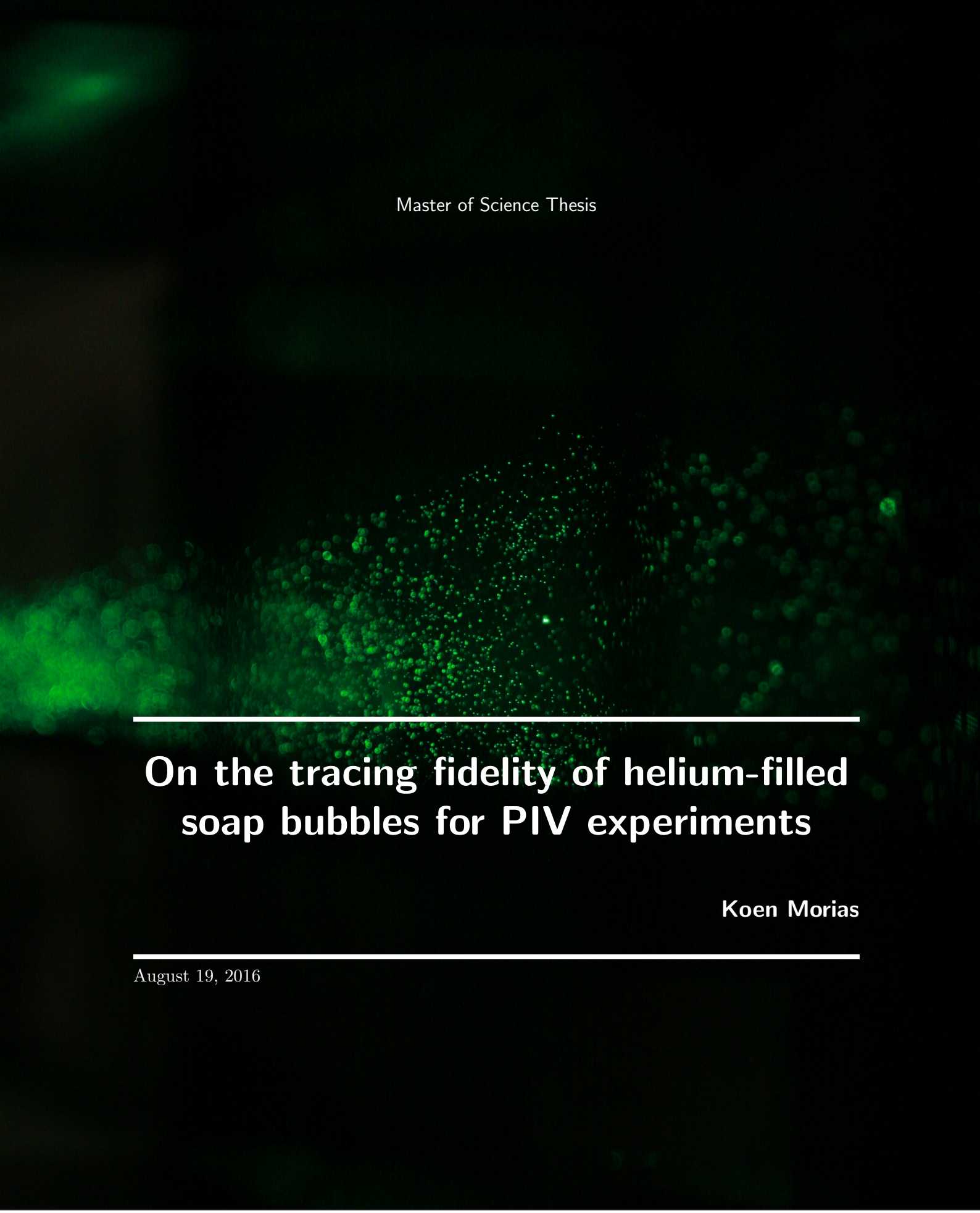

Master of Science Thesis

On the tracing fidelity of helium-filled soap bubbles for PIV experiments

Koen Morias

August 19, 2016

Aerodynamics

Faculty of Aerospace Engineering

TU Delft

Delft University of Technology

On the tracing fidelity of helium-filled soap bubbles for PIV experiments

Master of Science Thesis

For obtaining the degree of Master of Science in Aerospace Engineering
at Delft University of Technology

Koen Morias

August 19, 2016

Faculty of Aerospace Engineering · Delft University of Technology

Delft University of Technology

DELFT UNIVERSITY OF TECHNOLOGY
DEPARTMENT OF AERODYNAMICS

The undersigned hereby certify that they have read and recommend to the Faculty of Aerospace Engineering for acceptance the thesis entitled **"On the tracing fidelity of helium-filled soap bubbles for PIV experiments"** by **Koen Morias** in fulfillment of the requirements for the degree of **Master of Science**.

Dated: August 19, 2016

Supervisors:

Prof. Dr. F. Scarano

Dr. A. Sciachittano

Dr. D. Ragni

MSc. G. Caridi

Preface

This master thesis marks the end of six years of some hard labour, but most of all of many beautiful moments at TU Delft. I am relieved I can leave Delft with a master degree in Aerospace Engineering and an inexhaustible amount of life experience and wisdom.

This thesis report could not have been written without the support of many people. First of all, I want to thank my supervisor Andrea Sciacchitano. My search for the right thesis has definitely not been easy, but your passion for your work, your persuasiveness and flexibility were definitely decisive factors. One year later, I can say you are not only a great scientist, but also a very skilled teacher and more important a humble and sympathetic human-being. I enjoyed our journey together and admire you for bearing with me for more than a year. I am also very grateful for the support I received from Giuseppe Caridi. Your help was always very valuable and my experimental campaign would never have been the same without you. I wish you a lot of courage and perseverance in obtaining your PhD-degree and I am already looking forward to your graduation in two years from now. Another word of appreciation goes to all the members of the large-scale PIV research group for our informative and enjoyable weekly meetings. Also, I want to thank Peter Duyndam for his technical expertise in the fabrication of my wind tunnel models. During my thesis I spent many months in the basement of the high speed laboratory, but I was surrounded by great people. A warm thank you goes to all my fellow master students, 'the Souterrain legends', especially Edgar, Emel, Jaap, Jiggar, Remco, Thomas and William, for their company, (academic) help during the thesis and for the various conversations during our numerous coffee breaks. You all made last year definitely more enjoyable.

I would like to thank my friends Chabely, Christophe, Gert, Gert-Jan, Marly and Tim for their friendship, patience in turbulent times and support during the last six years. The best memories of my student life will forever be associated with you and I am excited to see what the future will bring for all of us. Another word of gratitude goes to Frederick: being roommates for five months in the USA was the start of some great adventures together. Thank you for all your support and wisdom of life. Finally, a very warm thank you goes to my parents, brother and family for their patience, unconditional love and support.

Koen Morias
Delft, August 2016

Summary

Since the introduction of Tomographic Particle Image Velocimetry (Tomo-PIV), the measurement volume has been recognized as a major bottleneck due to the limitation of laser pulse energy and the constraints on imaging depth of focus. The use of sub-millimeter helium-filled soap bubbles (HFSBs) as tracer particles has shown to overcome this limitation. With a diameter (300-500 μm) two orders of magnitude larger than conventional seeding particles, the amount of scattered light enables the measurement over a measurement volume several orders of magnitude larger. This thesis follows a previous study on the aerodynamic characterization of helium-filled soap bubbles (HFSBs) for large-scale PIV measurements and aims at characterizing statistically the tracing fidelity of HFSBs in PIV experiments. The tracing capability of the bubbles is studied considering the statistical distribution of the bubbles diameter, slip velocity, relaxation time and density.

A theoretical model is developed to determine the bubble density and production rate, based on the flow rates applied to the fluid supply unit (FSU). This model reveals that the bubble density is independent of the bubble diameter and is a function of solely the volume flow rate ratio of helium and bubble fluid solution. Numerical simulations of the equation of motion of particles at finite Reynolds numbers are performed. It is found that the fluid-stress force is dominant and that the drag force at finite Reynolds number cannot be represented by the Stokes drag force. The added-mass force is in general at least two orders of magnitude smaller than the fluid-stress force and has a negligible effect on the bubble trajectory for neutrally buoyant HFSBs.

High-speed visualizations identify two different operating regimes of the bubble generator. Two dedicated experiments are performed at a spatial resolution such to determine simultaneously the bubbles trajectory and their diameter. The velocity of the bubbles in the stagnation region ahead of a circular cylinder is evaluated by the PTV technique. The results are compared with micron-sized fog droplets taken as reference. The tracking error of individual trajectories is assessed by statistical analysis of the relative slip between the bubble and the airflow. The instantaneous particle relaxation time is retrieved from the ratio between slip velocity and local acceleration. Additional information on the bubble instantaneous properties is taken by inferring the diameter from the distance between the glare points. HFSBs were found to yield, on average, a time response of about 10 μs with a standard deviation that exceeds 30 μs when the nozzle is in a stable operating regime (bubbling). However, when the nozzle operates in an unstable operating regime (jetting), the standard deviation of the

bubble diameter and relaxation time can be as high as 70 μm and 50 μs, respectively. The HFSBs relative density to air is estimated using a modified Stokes drag law.

HFSBs as flow tracers in a laminar flat plate boundary layer feature a particle-free region close to the flat plate surface. The height of this region is a function of the particle diameter and can be partly explained by the conservation of mass principle of a streamtube far upstream that expands inside the boundary layer.

Table of Contents

Preface v

Summary vii

List of Figures xiii

List of Tables xvii

Nomenclature xix

1 Introduction 1

1.1 Aim of the thesis . . . 4

1.2 Thesis outline . . . 4

2 Particle image velocimetry and helium-filled soap bubbles 5

2.1 Particle image velocimetry . . . 5

2.2 Tomographic particle image velocimetry . . . 6

2.3 Particle-image intensity . . . 9

2.4 Tracer particles . . . 11

2.4.1 Particle dynamics . . . 12

2.4.2 Tracing fidelity . . . 16

2.4.3 Commonly used tracer particles . . . 18

2.5 Helium-filled soap bubbles . . . 18
2.5.1 Overview of earlier applications . . . 18
2.5.2 Bubble generator . . . 20
2.5.3 Tracing fidelity . . . 21
2.5.4 Optical properties . . . 22

3 Theoretical analysis 25

3.1 Bubble physics, production and behaviour . . . 25
3.1.1 Bubble physics: helium-filled soap bubbles . . . 26
3.1.2 Bubble physics: air-filled soap bubbles . . . 27
3.1.3 Bubble production . . . 27
3.1.4 Production rate . . . 29
3.1.5 Settling velocity . . . 30
3.2 Tracing fidelity . . . 32
3.2.1 Relaxation time . . . 32
3.2.2 Bubble trajectory simulator . . . 33
3.2.3 Simulation results . . . 34

4 Experimental methodology 41

4.1 Experimental techniques . . . 41
4.1.1 Particle Tracking Velocimetry (PTV) . . . 42
4.1.2 Particle Image Velocimetry (PIV) . . . 43
4.2 Cylinder experiment . . . 44
4.2.1 Bubble velocity and acceleration . . . 45
4.2.2 Reference velocity and acceleration . . . 45
4.2.3 Relaxation time . . . 46
4.2.4 Bubble diameter . . . 46
4.2.5 Bubble density . . . 47

4.2.6 Bubble soap film thickness . . . 48
4.3 Boundary layer experiment . . . 48
4.4 Data reduction techniques . . . 49

5 Experimental apparatus & set-up 53

5.1 Facility and models . . . 53
5.1.1 Wind tunnel facility . . . 53
5.1.2 Models . . . 54
5.2 Cylinder experiment . . . 54
5.2.1 Set-up . . . 54
5.2.2 Test matrix . . . 56
5.3 Boundary layer experiment . . . 57
5.3.1 Set-up . . . 57
5.3.2 Test matrix . . . 58
5.4 Image and data processing . . . 59
5.4.1 Image pre-processing . . . 60
5.4.2 Helium-filled soap bubbles . . . 60
5.4.3 Fog droplets . . . 61

6 Experimental results 63

6.1 Flow visualization of nozzle production . . . 63
6.2 Image recordings . . . 64
6.3 Mean velocity fields . . . 65
6.4 Individual bubble analysis . . . 67
6.4.1 Mean velocity and acceleration profiles along stagnation line . . . 67
6.4.2 Slip velocity, particle acceleration and relaxation time . . . 68
6.4.3 Bubble diameter statistics . . . 71
6.4.4 Bubble density statistics . . . 73

6.4.5 Bubble film thickness statistics 75

7 Experimental results: laminar boundary layer 77

7.1 Reference solution 77

7.2 Helium-filled soap bubbles inside a laminar boundary layer 79

8 Conclusion & Recommendations 85

8.1 Conclusion 85

8.2 Recommendations 86

Bibliography 89

A Matlab code of particle trajectory simulator 95

List of Figures

1.1 Applications of aerodynamics in daily life. From left to right: Wright flyer of the first human flight (1903), wing tip vortex visualisation, largest passenger airplane A380, cycling time trial optimization, Formula 1 race car and wind turbines. . . . 1

1.2 Experimental techniques for aerodynamics research. From left to right: Leonardo da Vinci drawings, turfs, smoke streamlines around sphere, wing tip vortex by bubbles streamlines, Pitot tube, hot-wire anemometer and Laser Doppler Anemometry. 2

2.1 *Left*: Schematic overview of the working principle and set-up of a PIV experiment (Raffel et al., 2007). *Right*: Schematic PTV and PIV analysis (reproduced from Lynch (2015)). 6

2.2 Principal of tomo-PIV (reproduced after Elsinga et al. (2006)). 7

2.3 Relevant tomo-PIV experiments in air of the last decade (reproduced and updated from Scarano et al. (2015)). 1 Elsinga et al. (2006), 2 Humble et al. (2007), 3 Atkinson et al. (2011), 4 Schröder et al. (2011), 5 Staack et al. (2010), 6 Fukuchi (2012), 7 Kühn et al. (2011), 8 Pröbsting et al. (2013), 9 Violato et al. (2011), 10 Ghaemi and Scarano (2011), 11 Schröder et al. (2009), 12 Michaelis et al. (2012), 13 Scarano et al. (2015), 14 Schneiders et al. (2016), 15 Caridi et al. (2015). . . 9

2.4 *Left*: Scattering behavior of particles approximated with power laws (after Adrian and Yao (1985)). *Right*: Schematic representation of PIV set-up (reproduced from Westerweel (1997)). 10

2.5 *Left*: Schematic description of a double-pass illumination system (reproduced from Scarano (2013a)). *Right*: Schematic description of a multi-pass illumination system (reproduced from Ghaemi and Scarano (2010)). 11

2.6 Sphere drag at finite particle Reynolds numbers with Stokes drag (Stokes), Oseen and Schiller and Naumann (SN). *Left*: Drag correction factor Φ. *Right*: Drag coefficient C_d. (Reproduced from Marshall and Li (2014).) 13

2.7 Exponential decay after velocity step change (reproduced after Scarano (2013b)). 17

2.8 HFSBs trajectories of the experiment by Kerho and Bragg (1994). 19

2.9 Initial nozzle design by Okuno et al. (1993). 20

2.10 Bubble Generator System. *Left*: Pitot type nozzle (reproduced from Bosbach et al. (2009)). *Right*: Schematic overview of the fluid supply unit (FSU). 21

2.11 Time averaged streamlines at $U_\infty = 30$ m/s obtained with micron-sized droplets and HFSBs with four different volume rates of BFS and two volume rates of helium: $Q_{He} = 4$ l/h (left) and $Q_{He} = 5$ l/h (right). Streamlines are determined by cross-correlation analysis (reproduced from Scarano et al. (2015)). 22

2.12 Glare points explained by light rays in a HFSB. *Left*: Schematic view of glare points (reproduced after Tropea (2011)). *Right*: Glare points as seen by eye (Machacek, 2003). 23

3.1 HFSB physics. *Left*: Soap film thickness (contour lines) in function of the bubble diameter d_p and specific density $\bar{\rho}$. *Right*: Mass of the soap film and helium inside a bubble in function of the bubble diameter d_p and the specific density $\bar{\rho}$ (contour lines). 27

3.2 AFSB physics. *Left*: Soap film thickness (contour lines) in function of the bubble diameter d_p and specific density $\bar{\rho}$. *Right*: Mass of the soap film and helium inside a bubble in function of the bubble diameter d_p and the specific density $\bar{\rho}$ (contour lines). 28

3.3 FSU flow rate ratios with solid lines as exact solution and dotted lines with surface tension influence neglected. *Left*: Specific density (contour lines) in function of the bubble diameter d_p and mass flow rate ratio $\dot{m}_{He}/\dot{m}_{bfs}$. *Right*: Specific density (contour lines) in function of the bubble diameter d_p and volume flow rate ratio Q_{He}/Q_{bfs}. 28

3.4 The specific density $\bar{\rho}$ of the HFSBs in function of the FSU volume flow rate ratio Q_{He}/Q_{bfs}. 29

3.5 Theoretical relation between the FSU supply volume flow rates of helium over BFS and the specific density $\bar{\rho}$ of the HFSBs. 30

3.6 Relaxation time τ_p (contour lines) based on the settling velocity of spherical particles in stagnant air under different accelerations. 31

3.7 Simplified equation of motion of a HFSB (d_p=400 μm and $\bar{\rho}$=1.02). Left: Ratio slip velocity over particle acceleration on the stagnation streamline ahead of the cylinder. Right: Influence of the time step Δt on the accuracy. 35

3.8 Simplified equation of motion. *Left:* fog droplet (d_p=1 μm and $\bar{\rho}$=816.33). *Right:* HFSB (d_p=400 μm and $\bar{\rho}$=1.02). 36

3.9 Influence of the drag correction factor on the ratio slip velocity over particle acceleration for HFSBs (d_p=400 μm and $\bar{\rho}$=1.02). 38

3.10 Full equation of motion of a HFSB (d_p=400 μm and $\bar{\rho}$=1.02). *Left:* ratio slip velocity over particle acceleration. *Right:* Forces. 39

3.11 Full equation of motion for an AFSB ($\bar{\rho}$=1.80 and d_p = 400 μm). *Left:* ratio slip velocity over particle acceleration. *Right:* Forces. 40

4.1 Example of an image with a low image density: $N_I \ll 1$ (left) and with a high image density: $N_I \gg 1$ (right). (Reproduced from Raffel et al. (2007)). 42

4.2 PTV track with a third-order polynomial fit through 15 datapoints (synthetic data of a one-dimensional deceleration). *Left*: Position (third-order polynomial). *Middle*: Velocity (first-order derivative). *Right*: Acceleration (second-order derivative). 43

4.3 Velocity vector extraction using cross-correlation from PIV images (reproduced from Scarano (2013b)). 44

4.4 *Left*: Schematic overview of glare points distance for a HFSB in a planar PIV set-up. *Right*: Glare points as measured with planar PIV, red crosses indicate intensity maxima (Gaussian fit). 47

4.5 Normal distribution $\mathcal{N}(0,1)$. *Left:* Probability density function $f(x|0,1)$. *Right:* Cumulative distribution function $F(x|0,1)$. 50

5.1 *Left*: Schematic overview of the cylinder model. *Right*: Schematic overview of flat plate model. 54

5.2 Set-up of the cylinder experiment. *Left*: Photograph. *Right*: Schematic overview. 55

5.3 Bubble generator v2 from LaVision GmbH. *Left*: Nozzle. *Right*: Operating nozzle in aerodynamic rake installed in the settling chamber of the wind tunnel. 56

5.4 Set-up of the flat plate experiment. *Left*: Photograph. *Right*: Schematic overview. 58

6.1 High speed visualization of HFSBs production in bubbling (left) and jetting regime (right). 64

6.2 Image recordings at freestream velocity of 10 m/s. *Top:* single snapshot. *Bottom:* superposition of 500 time-resolved images. 65

6.3 Mean velocity profile along the stagnation streamline ahead of a cylinder by sum-of-correlation of all the images. 66

6.4 Superimposition of all tracks for neutrally buoyant bubbles (HFSB 1). 67

6.5 Mean velocity (left) and acceleration (right) profiles on the stagnation streamline ahead the cylinder. 68

6.6 Slip velocity (left), acceleration (right) and relaxation time (bottom) of individual bubbles on the stagnation line of the cylinder for heavier-than-air air-filled soap bubbles (AFSB 6). Black dashed lines indicate the uncertainty due to the freestream turbulence intensity. 69

6.7 Slip velocity (left), acceleration (right) and relaxation time (top) of individual bubbles on the stagnation line of the cylinder for neutrally buoyant helium-filled soap bubbles (HFSB 1). Black dashed lines indicate the uncertainty due to the freestream turbulence intensity. 70

6.8 Relaxation time of individual bubbles on the stagnation line of the cylinder for neutrally buoyant helium-filled soap bubbles. Black dashed lines indicate the uncertainty due to the freestream turbulence intensity. *Left:* HFSB 2. *Right:* HFSB 3. 71

6.9 HFSB diameter statistics. Left: diameter distribution. Right: diameter uncertainty. 72

6.10 The influence of the Q_{bfs} on the bubble diameter statistics (left) and an example of the unstable bubble production for HFSB 4 (right). 72

6.11 Bubble density of individual bubbles on the stagnation line of the cylinder. *Left:* Neutrally buoyant helium-filled soap bubbles (HFSB 1). *Right:* Air-filled soap bubbles (AFSB 6). 73

6.12 The influence of the ratio Q_{He}/Q_{bfs} on the bubble density statistics. 74

6.13 Bubble soap film thickness of individual bubbles on the stagnation line of the cylinder for neutrally buoyant helium-filled soap bubbles (HFSB 1). 75

7.1 Boundary layer 300 mm downstream the leading edge, measured by PIV with fog droplets. *Top*: Velocity $u_{x'}$. *Bottom*: Shear $\frac{du_{x'}}{dy'}$. 78

7.2 Velocity profiles along a line perpendicular to the flat plate, approximately 305 mm downstream the leading edge, measured by PIV with fog droplets. *Left*: full, dimensional velocity profile $u_{x'}$. *Right*: non-dimensional boundary layer velocity profile $u_{x'}/U_0$. 79

7.3 Boundary layer on the leading edge, measured by PIV with fog droplets: velocity $u_{x'}$. 79

7.4 Boundary layer 300 mm downstream the leading edge. Contour levels are velocity $u_{x'}$ measured by PIV with fog droplets. *Top*: small bubbles (d_p=200 μm). *Middle*: medium bubbles (d_p=300 μm). *Bottom*: large bubbles (d_p=600 μm). 80

7.5 Particle concentration inside the boundary layer for different bubble diameters d_p. 81

7.6 Expansion of a stream tube far upstream and inside a boundary layer of a flat plate, based on the conservation of mass. 81

7.7 HFSBs in a laminar boundary layer at the leading edge. Contour levels are velocity $u_{x'}$ measured by PIV with fog droplets. *Top*: small bubbles (d_p=200 μm). *Middle*: medium bubbles (d_p=300 μm). *Bottom*: large bubbles (d_p=600 μm). 83

List of Tables

2.1 Experimental parameters of relevant tomo-PIV experiments of the last decade. Numbering in accordance with Figure 2.3. (Reproduced and updated from Scarano (2013a)). 8

2.2 Tracer particles for PIV experiments in air. 18

5.1 Experimental parameters of experiment with cylinder. 56

5.2 HFSB test matrix of cylinder experiment. 57

5.3 Experimental parameters of boundary layer experiment with flat plate. 59

5.4 HFSB test matrix of flat plate experiment. 59

5.5 PTV settings for both the experiments. 60

6.1 Supply flow rates and terminology for different helium-filled soap bubbles (HFSBs) and air-filled soap bubbles (AFSBs). 66

6.2 Diameter, relaxation time and density statistics for different helium-filled soap bubbles. 76

Nomenclature

Abbreviations

AFSB	Air-filled soap bubble
BFS	Bubble fluid solution
CFD	Computational Fluid Dynamics
DNS	Direct Numerical Simulation
FOV	Field of view
FSU	Fluid supply unit
HFSB	Helium-filled soap bubble
HSL	High speed laboratory
LDA	Laser Doppler Anemometry
LES	Large Eddy Simulation
N-S	Navier-Stokes
PIV	Particle Image Velocimetry
ppp	Particles per pixel
PTV	Particle Tracking Velocimetry
RANS	Reynolds-Averaged Navier-Stokes
SA	Secondary airflow
Tomo-PIV	Tomographic Particle Image Velocimetry

Greek Symbols

Δt	Laser pulse separation	[s]
Δt	Time step	[s]
ΔX_0	Light sheet width	[m]
δz	Depth of field	[m]
ΔZ_0	Light sheet thickness	[m]
Δ	Difference	
$\bar{\mathcal{E}}_p$	Energy per unit area	[J/m^2]
ϵ_Z	Particle distance from plane of focus	[m]
λ	Light wavelength	[m]

μ	Dynamic viscosity	[N s/m^2]
μ	Mean value	
ν	Kinematic viscosity	[m^2/s]
δ^*	Displacement thickness	[m]
δ_{99}	Boundary layer thickness	[m]
Ω	Rotation	[s^{-1}]
Φ	Drag correction factor	[-]
$\bar{\rho}$	Specific density	[-]
ρ	Density	[kg/m^3]
σ	Standard deviation	
τ	Relaxation time	[s]
θ	Momentum thickness	[m]
ζ	Amplification factor	[-]

Latin Symbols

a	Particle radius	[m]
A_I	Interrogation area in the image plane	[m^2]
C	Mean number of particles per unit volume	[particles/m^3]
D	Diameter of cylinder model	[m]
d_G	Glare point distance	[m]
d_p	Particle diameter	[m]
d_τ	Particle image diameter	[m]
D_a	Objective aperture diameter	[m]
$\mathbf{F}$	Force	[N]
f	Focal length	[m]
$f_\#$	f-number	[-]
H	Shape factor	[-]
J_0	Light pulse energy	[J]
K	History kernel function	[-]
L	Length scale of fluid	[m]
$\dot{m}$	Mass flow rate	[kg/s]
M	Molar mass	[g/mol]
M_0	Magnification factor	[-]
m_p	Particle mass	[kg]
N	Sample size	[-]
N_I	Image density	[particles]
p	Pressure	[Pa]
Q	Volume flow rate	[ml/s]
R	Universal gas constant	[J/(mol·K)]
Re	Reynolds number	[-]
T	Temperature	[K]

t	Soap film thickness	[m]
t_0	Time	[s]
$\mathbf{u}$	Fluid velocity	[m/s]
$\mathbf{u}_s$	Slip velocity	[m/s]
U_0	Freestream velocity	[m/s]
$\mathbf{v}_p$	Particle velocity	[m/s]
$\mathbf{x}$	Position	[m]
Z_0	Object distance	[m]

Subscripts

∞	Free stream
bfs	Bubble fluid solution
f	Surrounding fluid
He	Helium
p	Particle
sa	Secondary airflow

Chapter 1

Introduction

A century and a decade after the first human flight, the aerospace industry has made huge progress. Nowadays, more than 3 billion passengers are flying on yearly basis and aviation is the safest way of transportation world wide. Part of this progress is due to the extensive research in aerodynamics. It led not only to basic aircraft and wing designs, but also to energy efficient and safe contributions outside the aerospace world, among others the wind energy industry, ground transportation concepts, sport aerodynamics, aeroacoustics, heat convection studies and propulsion and combustion applications (Figure 1.1).

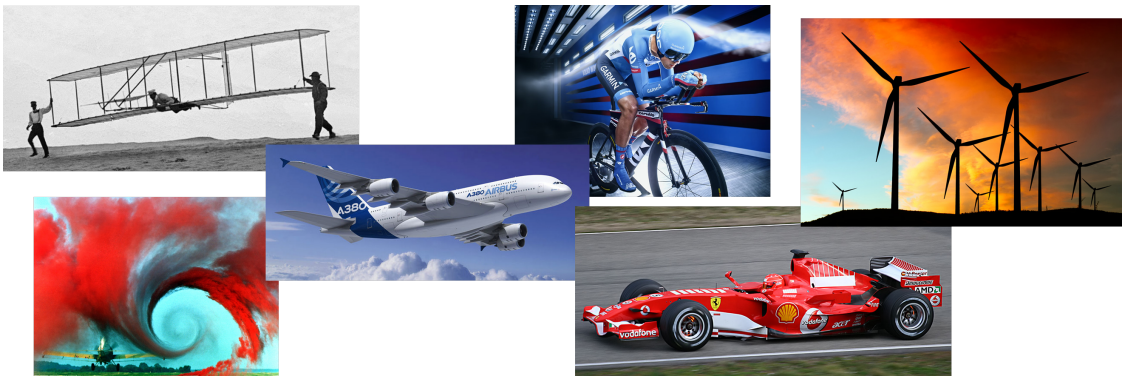

Figure 1.1: Applications of aerodynamics in daily life. From left to right: Wright flyer of the first human flight (1903), wing tip vortex visualisation, largest passenger airplane A380, cycling time trial optimization, Formula 1 race car and wind turbines.

Aerodynamics research can be categorized in three subdomains: theoretical, computational and experimental work. The theoretical side is focussed on finding solutions to the flow governing Navier-Stokes equations. A mathematical problem that is still unsolved due to the complex non-linearity of the equations and is classified as one of the millennium prize problems. However, simplified forms of the N-S equations led to only a few theoretical solutions such as laminar flows on flat plates and in ducts, the potential flow theory and insights in the boundary layer physics (boundary layer theory). Computational Fluid Dynamics (CFD)

are numerical solutions of the (simplified) N-S equations, where the spatial and temporal scales are discretized in finite steps. The most sophisticated simulations at present are Direct Numerical Simulations (DNS), where all the spatial and temporal scales of turbulence are resolved without using a turbulence model. Since this approach is way too computational expensive for the current computational capabilities at large-scale or in highly turbulent flows, Reynolds-Averaged Navier-Stokes (RANS) solutions are popular nowadays. RANS solutions compute a time-averaged flow field and account for the fluctuating quantities by mathematical models. When dealing with turbulence research, Large Eddy Simulations (LES) offer a good alternative to DNS by modelling the smallest length scales by mathematical models, reducing the computation load. CFD renders some uncertainty due to the choice of grid selection, numerical scheme and turbulence model and therefore requires (experimental) validation.

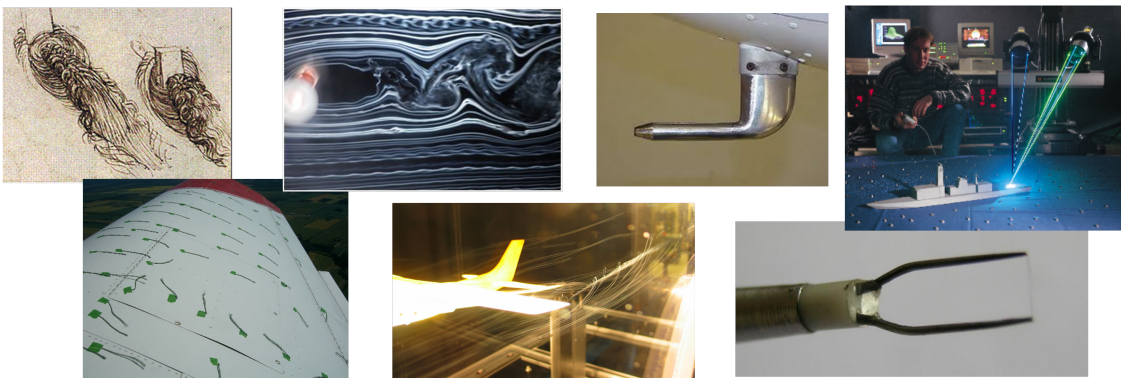

Figure 1.2: Experimental techniques for aerodynamics research. From left to right: Leonardo da Vinci drawings, turfs, smoke streamlines around sphere, wing tip vortex by bubbles streamlines, Pitot tube, hot-wire anemometer and Laser Doppler Anemometry.

In experimental aerodynamics two types of experiments are distinguished: qualitative and quantitative experiments. The former dates back from the flow visualization experiments by Leonardo da Vinci (1452-1519) to gain insight in the flow structures, with a specific interest in vortices. More modern flow visualization techniques include oil flow visualisation, adding dye or smoke in the flow or are based on the changes in optical refractive index due to the flow structure (shadowgraphy or Schlieren photography). There is, however, a huge demand for quantitative experimental data. Firstly, it is the preferred option to analyse the flow field around complex geometries or at large-scale. Secondly, it serves as benchmark to validate numerical simulations and lastly because of certification requirements. This need stimulated the development of velocity measurement techniques. Among others, Pitot tubes and hot wire anemometry are popular and accurate techniques. However, they are both intrusive and thus bring distortions along and only measure the velocity magnitude in a single point. Advancements in laser and camera technology lead to other measurement techniques such as Laser Doppler Anemometry (LDA). LDA is a very accurate optical velocimetry method, but relies still on a single-point velocity evaluation. An overview of some relevant techniques is given in Figure 1.2. Non-intrustive, multi-point, time-resolved measurements became feasible by Particle Image Velocimetry (PIV). PIV relies on the velocity extraction of in the flow submerged tracer particles by illuminating them with consecutive, short light pulses and recording their position with cameras.

Since the introduction of Tomographic Particle Image Velocimetry (Tomo-PIV; three componential velocity evaluation in a three dimensional volume), the measurement volume has been recognized as a major bottleneck due to the limitation of laser pulse energy and the constraints on imaging depth of focus (Scarano, 2013a). The use of lasers with pulse energy up to 1 J has marginally increased the volume with respect to the first experiment conducted by Elsinga et al. (2006), where the velocity was measured in a domain of $3.5\times3.5\times0.7$ cm^3. PIV experiments in air usually use fog droplets as tracers particles. Instead, experiments in water flows could be conducted at a significant larger size by using large neutrally buoyant tracers. The little energy scattered by micron-sized tracers can be considered as the main limitation preventing the upscale of Tomo-PIV and its deployment for industrial aerodynamics. The use of sub-millimeter helium-filled soap bubbles (HFSBs) as tracer particles has shown to overcome this limitation. With a diameter (300-500 μm) two orders of magnitude larger than the conventional seeding particles, the amount of scattered light enables the measurement over a measurement volume several orders of magnitude larger (Caridi et al., 2015).

The tracing fidelity of these bubbles has been studied recently by Scarano et al. (2015). They found out that HFSBs can be produced approaching neutral buoyancy and exhibiting a mean relaxation time of about 10 μs. Furthermore, the authors demonstrated the potential to employ these tracers for large-scale time-resolved tomographic PIV with a measurement in a volume of $20\times20\times12$ cm^3. However, some questions remain open concerning the aerodynamic behaviour of HFSBs. First, Scarano et al. (2015) report only the ensemble average relaxation time of the HFSBs. It is not known to what extent the relaxation time and density individual bubbles depart from the mean. This aspect is of primary importance to validate the use of HFSBs for instantaneous velocity fluctuations and turbulent statistics. Furthermore, the results reported on the tracing behaviour of the bubbles rely on the hypothesis of Stokes flow theory, which is only valid at Reynolds number well below unity. The latter is defined as:

$$Re_p = \frac{\rho_f \left|\mathbf{u} - \mathbf{v}_p\right| d_p}{\mu_f} \tag{1.1}$$

where $\mathbf{v}_p$ and d_p and are the particle velocity and diameter, respectively. The symbol $\mathbf{u}$ refers to the flow velocity. The difference between particle velocity and fluid velocity is referred to as slip velocity. Density and dynamic viscosity of the fluid are expressed by ρ_f and $\mathbf{u}$, respectively. When the specific density of a bubble $\bar{\rho}$ (ratio of bubble density over fluid density ρ_p/ρ_f) deviates from unity and the diameter increases, a finite slip velocity arises and the assumption $\mathrm{Re}_p \ll 1$ may no longer be valid. Scarano et al. (2015) are reporting maximum particle Reynolds numbers up to 10, a clear violation of the above assumption.

Furthermore, in presence of flow shear, an additional transverse lift force acts on the particles due to the difference of velocity between top and bottom of the HFSBs. This lift force depends on the slip velocity, shear rate and particle radius. Several researchers derived theoretical expressions of the lift under assumptions of particles behaviour and the amount of shear (among others: Saffman, 1965; McLaughlin, 1991; Mei, 1992). However, experimental results are scarce and often disagree with the theoretical expressions reported in literature. Therefore, it is unknown whether the trajectory HFSBs is influenced by this additional force, when moving through a strong shear region.

1.1 Aim of the thesis

The present work aims at characterizing statistically the tracing fidelity of HFSBs in PIV experiments. The tracing capability of the bubbles is studied considering the statistical distribution of the bubbles diameter, slip velocity, relaxation time and density. The analysis will account not only for the viscous Stokes drag, but also for quasi-steady drag at finite particle Reynolds numbers. The contribution of the latter will be evaluated in the slip velocity and particle response time. Experiments are performed at a spatial resolution such to determine simultaneously the bubbles trajectory and their diameter. Based on the relaxation time, the study will determine the tracing fidelity expected from individual bubbles and its dependence upon the bubble generation regime. Furthermore, the lift force on HFSBs in shear flows will be investigated by assessing the behaviour of the bubbles in a laminar boundary layer.

1.2 Thesis outline

In Chapter 2 a literature survey is conducted that explains the basics of PIV and clearly demonstrates its limitations in terms of measurement volume. Furthermore, it deals with the theoretical particle dynamics and subsequently their tracing fidelity. The chapter also studies the earlier use of helium-filled soap bubbles as flow tracers and discusses their characteristics. Chapter 3 starts off with the introduction of a theoretical model that connects the bubble characteristics (density, diameter, film thickness and production rate) to the supply flow rates of the bubble generator. It discusses as well the influence of the different force terms on the tracing fidelity of the particles at finite Reynolds numbers by means of numerical simulations of the equation of motion. The experimental methodology of the PIV experiments is explained in Chapter 4; the experimental apparatus and set-up is discussed in Chapter 5. The experimental results of the experiments that deals with the tracing fidelity of helium-filled soap bubbles is discussed in Chapter 6. The results are compared with the theoretical model built in Chapter 3 and are discussed accordingly. The experimental results of using HFSBs as tracer particles in a PIV experiment in a laminar boundary layer is treated in Chapter 7. Finally, the conclusion of this work together with some recommendations for further research are given in the last chapter of this thesis, Chapter 8.

Chapter 2

Particle image velocimetry and helium-filled soap bubbles

2.1 Particle image velocimetry

Particle image velocimetry (PIV) is an optical, non-intrusive measurement technique in fluid mechanics. It is capable of measuring an instantaneous three-dimensional velocity field with a reasonably high temporal and spatial resolution.

The working principle is as follows: the flow field of interest is seeded with tracer particles and is illuminated by a light source. The reflected light of tracer particles enables cameras to record their position. Velocity vectors can be calculated by measuring and dividing the displacement of the tracer particles in two or more successive recordings by the time interval between the measurements. This principle is illustrated in Figure 2.1-left. Depending on the methodology used to obtain the velocity vectors, two different techniques can be distinguished.

1. *Particle Tracking Velocimetry* (PTV): relies on the identification and tracking of individual particles. The outcome is one velocity vector per particle at the particle position.

2. *Particle Image Velocimetry* (PIV): relies on the calculation of the mean displacement of a group of particles in an interrogation window by means of a statistical correlation between two images. The outcome is one mean velocity vector per interrogation window in the center of this interrogation window.

A more detailed review of both the techniques is given by Adrian and Westerweel (2010). In essence, PTV is preferred over PIV when the seeding concentration is low, since only then particles pairs in two consecutive images can be identified.

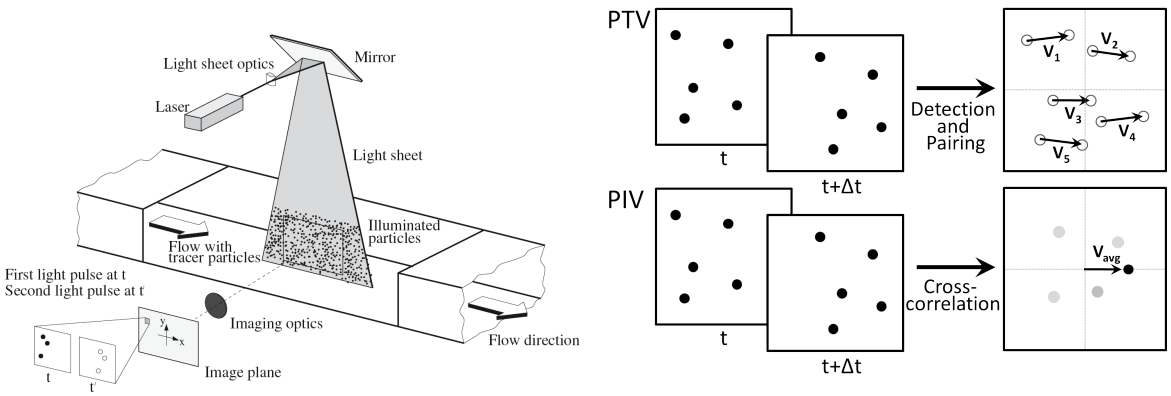

Figure 2.1: *Left*: Schematic overview of the working principle and set-up of a PIV experiment (Raffel et al., 2007). *Right*: Schematic PTV and PIV analysis (reproduced from Lynch (2015)).

Following the formulation of Westerweel (1997), the working principle can be formulated mathematically as follows. Consider a particle at time t_0 and position $\mathbf{x}(t_0)$. After a time interval Δt (the laser pulse separation), the new position can be expressed as $\mathbf{x}(t_0 + \Delta t)$. The displacement of the particle can be related to its velocity as:

$$\Delta\mathbf{x}(\mathbf{x}(t), t_0, \Delta t) = \int_{t_0}^{t_0+\Delta t} \mathbf{v}_p(\mathbf{x}(t), t)\, \mathrm{d}t. \tag{2.1}$$

Assuming that the acceleration of flow during the laser pulse separation Δt is sufficiently small, the particle velocity can be approximated with the difference quotient and can be expressed as:

$$\mathbf{v}_p(\mathbf{x}(t), t) = \lim_{\Delta t \to 0} \frac{\Delta\mathbf{x}(\mathbf{x}(t), t_0, \Delta t)}{\Delta t} \approx \frac{\mathbf{x}(t_0 + \Delta t) - \mathbf{x}(t_0)}{\Delta t} + \mathcal{O}(\Delta t) \tag{2.2}$$

The tracer particle velocity $\mathbf{v}_p(\mathbf{x}(t), t_0)$ is identical to the local fluid velocity $\mathbf{u}(\mathbf{x}(t), t_0)$ for ideal tracer particles, however, ideal tracers do not exist in practice. Therefore, tracer particles should be chosen carefully.

2.2 Tomographic particle image velocimetry

Particle image velocimetry (PIV) gained a lot of popularity in the last decade. Especially since the disclosure of tomographic particle image velocimetry (tomo-PIV) by Elsinga et al. (2006), the amount of applications and published papers increased significantly (Scarano, 2013a). Tomo-PIV relies on the reconstruction of the three-dimensional measurement volume, measured by at least three cameras under different angles. The resulting volume is built out of voxels (three-dimensional pixels), where the particles are represented as three-dimensional intensity maximums. The reconstructed volume is split up in interrogation volumes and for each interrogation volume a single three-component velocity vector is determined by means

of a statistical cross-correlation. A schematic overview of the working principle of tomo-PIV is given in Figure 2.2. It extended particle image velocimetry from two-component and three-component measurements in a plane (planar and stereoscopic PIV respectively) towards three-component measurements in a volume (tomographic PIV). In order to light up a three-dimensional volume, the laser beam needs to be expanded over the full measurement volume, reducing the local illumination intensity. The problem gets even worse by the small optical aperture (high $f_{\#}$), that is needed to ensure that all particles are in focus across the whole depth of the measurement domain. If the intensity of the light reflected by the particles becomes too low, the cameras cannot record their position. This is the main constraint of the measurement volume of tomo-PIV experiments.

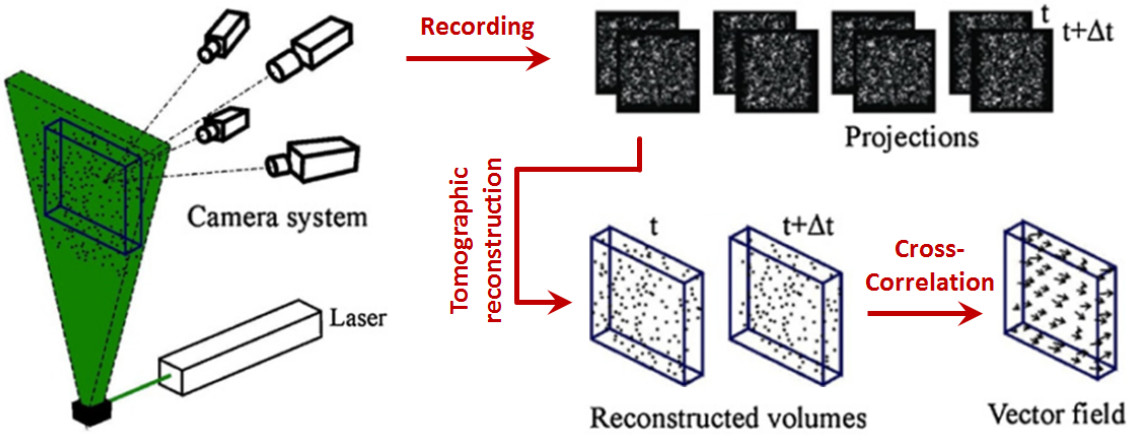

Figure 2.2: Principal of tomo-PIV (reproduced after Elsinga et al. (2006)).

The initial measurements by Elsinga et al. (2006) were conducted in a measurement volume of 3.5 × 3.5 × 0.7 cm^3 with 1 μm fog droplets as tracing particles. Further tomo-PIV experiments at a low acquisition frequency by Humble et al. (2007), Staack et al. (2010), Atkinson et al. (2011) and Schröder et al. (2011) do not go beyond measurement volumes of approximately 50 cm^3. Time-resolved measurements with an acquisition frequency in the kHz range by Schröder et al. (2009), Violato et al. (2011), Ghaemi and Scarano (2011), Michaelis et al. (2012) and Pröbsting et al. (2013) nearly exceed measurement volumes of 20 cm^3. This can be explained by the laser technology. High-speed Nd:YLF lasers are having a pulse energy of approximately 1-10 mJ/pulse in the kHz range, while standard dual-cavity Nd:YAG lasers have a pulse energy in the order of 100 mJ/pulse for non-time-resolved measurements. The largest measurement to date with micron-sized seeding was achieved by Fukuchi (2012) in a volume of 16 × 22 × 8 cm^3, with a reasonable signal-to-noise ratio in only 1,760 cm^3. An overview of relevant tomographic PIV experiments in the last decade is visualised in a synthetic diagram in Figure 2.3 and the corresponding experimental parameters are given in Table 2.1.

Recent tomo-PIV experiments by Kühn et al. (2011), Scarano et al. (2015), Caridi et al. (2015) and Schneiders et al. (2016) show the promising potential by using helium-filled soap bubbles as tracer particles, pushing measurement volume boundaries up to three orders of magnitude higher than tomo-PIV experiments with micron-sized tracer particles.

Table 2.1: Experimental parameters of relevant tomo-PIV experiments of the last decade. Numbering in accordance with Figure 2.3. (Reproduced and updated from Scarano (2013a)).

#	Experiment, (Reference)	Velocity, (Re)	Domain size (mm), (volume)	Tracers, concentration (total number)	Image size, resolution	Repetition rate, pulse energy	IV size, overlap factor	Vector grid, (total number)
1	Cylinder wake (Elsinga et al., 2006)	10 m/s (5,000)	$37 \times 36 \times 8$ (13 cm^3)	1 μm fog droplets 2 part/mm (23,000)	$4 \times 1376 \times 1040$ 18 voxels/mm	1 Hz 400 mJ	2.0 mm 75%	$77 \times 79 \times 15$ (91,000)
2	Shock wave boundary layer (Humble et al., 2007)	500 m/s (-)	$70 \times 35 \times 6.5$ (16 cm^3)	0.3 μm TiO_2 3 part/cm^3 (48,000)	$4 \times 2048 \times 1200$ 20 voxels/mm	10 Hz 400 mJ	2.0 mm 75 %	$142 \times 77 \times 14$ (153,000)
3	Turbulent boundary layer (Atkinson et al., 2011)	3 m/s (Re_θ=7,800)	$60 \times 60 \times 9$ (32 cm^3)	1 μm fog droplets 0.7 part/mm^3 (23,000)	$4 \times 2048 \times 2048$ 20 voxels/mm	1 Hz 250 mJ (double-pass)	3.2 mm 75 %	$72 \times 72 \times 8$ (41,000)
4	Backward-facing step (Schröder et al., 2011)	7 m/s (2,700)	$70 \times 93 \times 8$ (52 cm^3)	1 μm DEHS droplets N/A	$4 \times 4904 \times 3280$ 36 voxels/mm	1 Hz 400 mJ (double-pass)	1.0 mm 75 %	$286 \times 444 \times 29$ (3,700,000)
5	High-Re jet (Staack et al., 2010)	65 m/s (65,000)	$50 \times 50 \times 20$ (50 cm^3)	DEHS droplets 4 part/mm^3 (72,000)	$4 \times 2048 \times 2048$ 40 voxels/mm	4 Hz 200 mJ (double-pass)	2.0 mm 75 %	$75 \times 75 \times 29$ (160,000)
6	Cylinder wake (Fukuchi, 2012)	3.6 m/s (4,800)	$160 \times 220 \times 80$ (2,800 cm^3)	1 μm DEHS droplets 0.3 part./cm^3 (914,144)	$6 \times 4008 \times 2672$ 7.5 voxels/mm	1,000 Hz 900 mJ (multi-pass)	1.6 mm 75 %	$104 \times 136 \times 56$ (792,000)
7	Closed convective cell (Kühn et al., 2011)	< 1 m/s (-)	$750 \times 50 \times 165$ (55,500 cm^3)	200-300 μm HFSBs 0.75 part./cm^3 (42,700)	$4 \times 1392 \times 1024$ 1.3 voxels/mm	0.66 Hz 112 lm (double-pass)	48/24 mm 75 %	$62 \times 37 \times 27$ (62,000)
8	TR boundary layer wall pressure (Pröbsting et al., 2013)	10 m/s (Re_δ=6,240)	$19.7 \times 4.2 \times 41.3$ (3.4 cm^3)	1 μm fog droplets 10 part/mm^3 (36,700)	$4 \times 512 \times 1024$ 24 voxels/mm	10,000 Hz 25 mJ (multi-pass)	1.33/0.66 mm 75 %	$62 \times 26 \times 129$ (208,000)
9	TR Rod-airfoil interaction (Violato et al., 2011)	5 m/s (3,500)	$50 \times 50 \times 3$ (7.5 cm^3)	1 μm fog droplets 5 part/mm^3 (15,000)	$4 \times 800 \times 768$ 22 voxels/mm	5,000 Hz 12 mJ	2.5 mm 75 %	$66 \times 66 \times 6$ (26,000)
10	TR trailing edge (Ghaemi and Scarano, 2011)	14 m/s (370,000)	$47 \times 47 \times 8$ (18 cm^3)	1 μm fog droplets 4 part/mm^3 (72,000)	$4 \times 1024 \times 1024$ 22 voxels/mm	2,700 Hz 10 mJ (multi-pass)	1.5 mm 75 %	$128 \times 128 \times 22$ (360,000)
11	TR turbulent boundary layer (Schröder et al., 2009)	7 m/s (-)	$34 \times 30 \times 19$ (19 cm^3)	1.5 μm olive oil 3.5 part/mm^3 (42,000)	$4 \times 800 \times 768$ 24 voxels/mm	5,000 Hz 21 mJ (multi-pass)	2 mm 75 %	$46 \times 41 \times 24$ (45,000)
12	TR Insect wake (Michaelis et al., 2012)	3.3 m/s (-)	$70 \times 85 \times 6.2$ (37 cm^3)	N/A 1 part/mm^3 (36,700)	$4 \times 1024 \times 1024$ 12.5 voxels/mm	2,000 Hz 10 mJ	0.64 mm 75 %	$96 \times 129 \times 7$ (86,500)
13	TR Cylinder wake (Scarano et al., 2015)	5 m/s (17,000)	$200 \times 200 \times 120$ (4,800 cm^3)	300 μm HFSBs 1 part/cm^3 (4,800)	$4 \times 608 \times 448$ 4.6 voxels/mm	2,000 Hz 25 mJ	5.0 mm 75 %	$50 \times 50 \times 24$ (60,000)
14	TR Cylinder wake (Schneiders et al., 2016)	5 m/s (36,000)	$200 \times 170 \times 180$ (6,120 cm^3)	300 μm HFSBs 0,7 part/cm^3 (4,300)	$4 \times 1024 \times 1024$ 5 voxels/mm	2,000 Hz 25 mJ	N/A N/A	$70 \times 60 \times 60$ (252,000)
15	TR Vertical axis wind turbine (Caridi et al., 2015)	8.5 m/s (Re_c=170,000)	$380 \times 340 \times 190$ (24,500 cm^3)	300 μm HFSBs 1 part/cm^3 (4,800)	$3 \times 1024 \times 1024$ 3.3 voxels/mm	1,000 Hz 25 mJ	8.0 mm 75 %	$47 \times 35 \times 24$ (40,000)

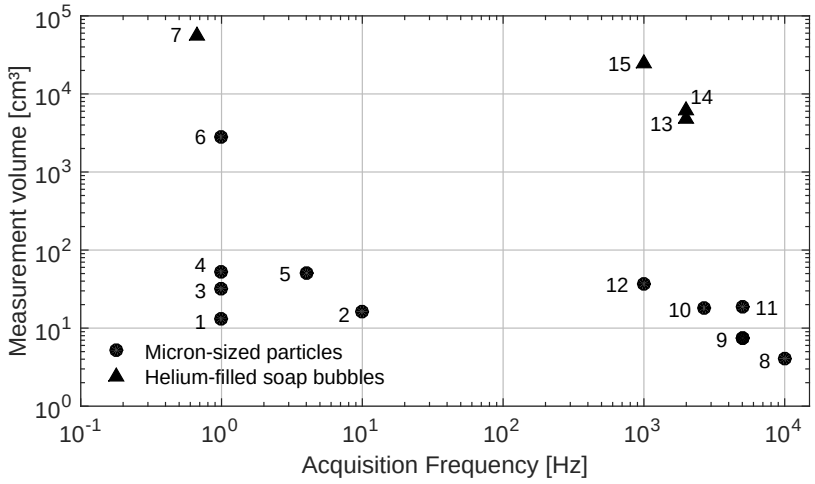

Figure 2.3: Relevant tomo-PIV experiments in air of the last decade (reproduced and updated from Scarano et al. (2015)). 1 Elsinga et al. (2006), 2 Humble et al. (2007), 3 Atkinson et al. (2011), 4 Schröder et al. (2011), 5 Staack et al. (2010), 6 Fukuchi (2012), 7 Kühn et al. (2011), 8 Pröbsting et al. (2013), 9 Violato et al. (2011), 10 Ghaemi and Scarano (2011), 11 Schröder et al. (2009), 12 Michaelis et al. (2012), 13 Scarano et al. (2015), 14 Schneiders et al. (2016), 15 Caridi et al. (2015).

2.3 Particle-image intensity

Adrian (1991) modeled the energy per unit area on a camera's light sensor by the scattered light of a particle. He approximated the scattering behavior of the particles with power laws with an exponent $2 \leq q \leq 4$, depending on the particle diameter. The energy increases with power exponent $q = 4$ in the Rayleigh scattering range ($d_p \ll \lambda$), with power exponent $q = 3$ in the Mie scattering range ($d_p \approx \lambda$) and with power exponent $q = 2$ in the geometric scattering range ($d_p \gg \lambda$), as depicted in Figure 2.4 after Adrian and Yao (1985). The energy per unit area $\bar{\mathcal{E}}_p$ can be approximated by:

$$\bar{\mathcal{E}}_p \approx \frac{\lambda^2 J_0 \; D_a^2 \; d_p^q}{\lambda^q Z_0^2 \; d_\tau^2 \; \Delta X_0 \; \Delta Z_0} \; \zeta \tag{2.3}$$

The latter contains the light wavelength λ, the light pulse energy J_0, the objective aperture D_a, the particle diameter d_p and the amplification factor ζ. The amplification factor ζ is a factor expressing the gain in light intensity by mechanical aid devices, such as a mirror. The energy per unit area $\bar{\mathcal{E}}_p$ is inversely proportional to the object distance Z_0, the particle image diameter d_τ, the light sheet width ΔX_0 and light sheet thickness ΔZ_0. A schematic overview of a PIV set-up with these parameters is given in Figure 2.4. The particle image diameter d_τ is given by:

$$d_\tau = \sqrt{(M_0 d_p)^2 + (2.44\,(1 + M_0)\, f_\# \lambda)^2 + \left(\frac{\epsilon_Z M_0^2}{f_\#}\right)^2} \tag{2.4}$$

where the first term on the right-hand side is due to geometrical imaging, the second due to diffraction imaging and the third being the out-of-focus blur. The magnification M_0 represents

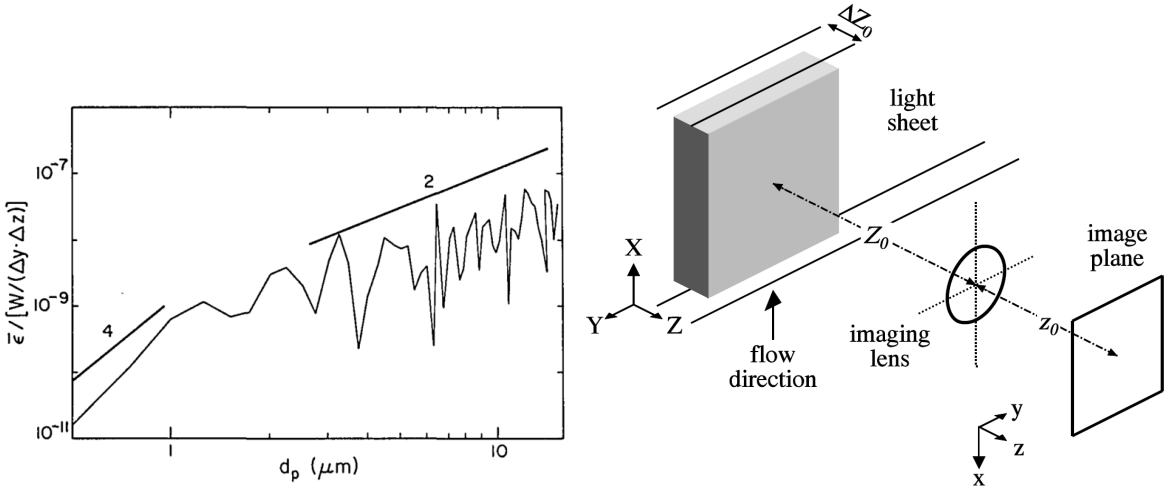

Figure 2.4: *Left*: Scattering behavior of particles approximated with power laws (after Adrian and Yao (1985)). *Right*: Schematic representation of PIV set-up (reproduced from Westerweel (1997)).

the ratio z_0/Z_0 (with z_0 being the distance between the lens and the imaging plane) and ϵ_Z is the distance of the particle from the plane of focus. The f-number $f_\#$ is the ratio of the focal length f of the lens over the aperture diameter D_a:

$$f_\# = \frac{f}{D_a} \tag{2.5}$$

Following Adrian (1991), if the image diameter is dominated by diffraction and the experiment is scaled up with a factor n in the $X-$direction while keeping the particle size constant and while using the same camera, then this will require to scale the object distance Z_0 with a factor n as well. The energy per unit area $\bar{\mathcal{E}}_p$ drops with a factor n^3. Furthermore, the problem becomes even more complicated when scaling up the experiment in the $Z-$direction. In order to have all particles in the measurement volume in focus, the depth of field δz of the imaging system needs to be equal or bigger than the thickness of the light sheet ΔZ_0. The depth of field can be approximated by:

$$\delta z \approx 4.88\lambda f_\#^2 \left(\frac{M_0+1}{M_0}\right)^2 \tag{2.6}$$

Keeping a constant magnification factor M_0, a scale up of the measurement volume with factor n in the Z direction yields a decrease of the aperture diameter D_a with a factor $\sqrt{n}$ to have the full depth of the measurement volume in focus. This gives a decrease in energy per unit area $\bar{\mathcal{E}}_p$ with a factor n^3.

The shortage of light at large-scale volumes requires to optimize the available light energy. The double-pass amplification system consists of a mirror perpendicular to the illumination axis, that reflects the light back into the measurement volume for a second time (Scarano, 2013a). This technique has been used by Scarano and Poelma (2009) in water and by Schröder

et al. (2011) in air. It results in an amplification factor ζ of approximately 1.5. The multi-pass amplification system uses two high reflective mirrors to reflect a laser beam with a small angle several times (typically 20) throughout the volume before exiting the measurement region. The first use has been reported by Schröder et al. (2008) and a detailed description of the working and design principles is given by Ghaemi and Scarano (2010). They reported an achievable amplification factor ζ of 5 with respect to the double-pass system and 7 with respect of single-pass illumination. A schematic overview of double- and multi-pass light amplification systems is given in Figure 2.5. An overview of the use of these light amplification systems in some relevant tomo-PIV experiments of the last decade is given in Table 2.1.

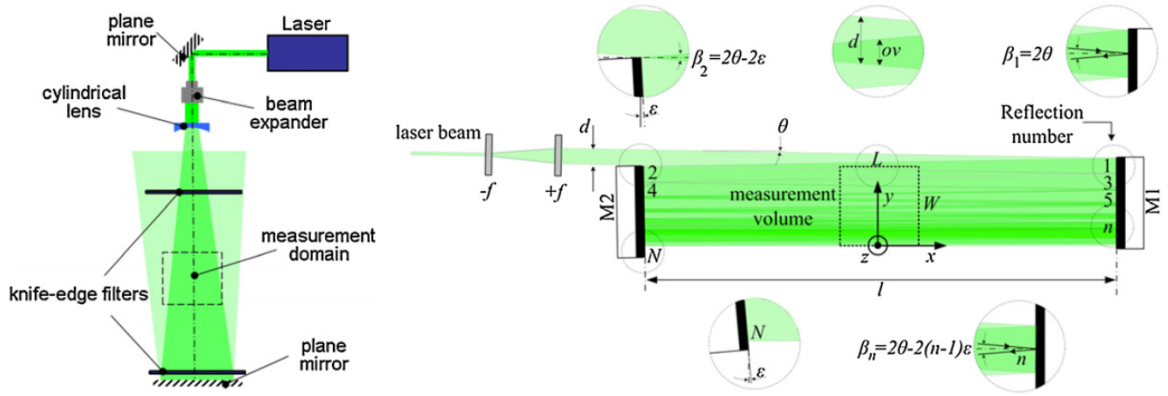

Figure 2.5: *Left*: Schematic description of a double-pass illumination system (reproduced from Scarano (2013a)). *Right*: Schematic description of a multi-pass illumination system (reproduced from Ghaemi and Scarano (2010)).

In large-scale applications, the measurement volume, i.e. the factor $\Delta X_0\ \Delta Z_0$, will increase with a factor $n = 10^3 - 10^4$. The loss in the particle image intensity in these experiments cannot be compensated by increasing and optimizing the laser power and requires the use of bigger particles.

2.4 Tracer particles

It hardly needs saying that the choice of tracer particles distinguishes quantitative techniques as PTV and PIV from ordinary flow visualization. An ideal particle should behave identical as an infinitesimal fluid flow element, such that the particle velocity equals the fluid velocity at any time. Furthermore, the particles need to scatter enough light to be visible by the imaging system. Finally, the concentration of the tracer particles should be sufficiently high in order to resolve the flow field with an acceptable spatial resolution, but not too high to not alter the flow field properties and to obstruct light.

2.4.1 Particle dynamics

The behavior of tracer particles can be modelled using Newton's second law

$$m_p \frac{d\mathbf{v}_p}{dt} = \mathbf{F}_{QS} + \mathbf{F}_{G-B} + \mathbf{F}_{FS} + \mathbf{F}_{AM} + \mathbf{F}_H + \mathbf{F}_L \tag{2.7}$$

where m_p is the mass of the particle, $d\mathbf{v}_p/dt$ is the particle acceleration and $\mathbf{F}_i$ are the forces acting on the particle. An extensive equation of motion for particles at finite Reynolds numbers ($Re_p > 1$) is given by Mei (1996), which is based on the work of Maxey and Riley (1983) for particles in Stokes regime ($Re_p < 1$). The definition of the particle Reynolds number Re_p is based on the difference between the particle velocity and the local fluid velocity, the particle slip velocity $|\mathbf{u} - \mathbf{v}_p|$, the fluid density ρ_f, the particle diameter d_p and the fluid dynamic viscosity μ_f:

$$Re_p = \frac{\rho_f \, |\mathbf{u} - \mathbf{v}_p| \, d_p}{\mu_f} \tag{2.8}$$

Both equations consider the quasi-steady drag force $\mathbf{F}_{QS}$, gravity-buoyancy force $\mathbf{F}_{G-B}$, pressure force $\mathbf{F}_{FS}$, added-mass force $\mathbf{F}_{AM}$ and history force $\mathbf{F}_H$. This survey adds a transverse lift force $\mathbf{F}_L$ due to the presence of a shear field or particle rotation to the equation of motion.

Quasi-steady drag force

The drag on a solid sphere moving through a stagnant fluid was first derived by Stokes (1851). The so-called Stokes drag (Equation 2.9) is based on the assumptions that the flow around the object is uniform, the particle Reynolds number Re_p is small compared to unity and the no-slip condition is satisfied on the sphere's boundary. The influence of non-uniform flow can be included with the Faxén term (last term in Equation 2.9), named after Faxén (1922). He studied a sphere in a non-uniform flow with a small value of d_p/L, where L is the length scale of the fluid. The Faxén term scales with $(a/L)^2$, with a $(= d_p/2)$ being the particle radius and can be neglected since one pre-assumes that d_p/L is small. Therefore, it will not be mentioned in the other force terms.

$$\mathbf{F}_{QS} = 6\pi\mu_f a \left(\mathbf{u} - \mathbf{v}_p + \frac{1}{6} a^2 \nabla^2 \mathbf{u} \right) \tag{2.9}$$

The Stokes drag breaks down at finite particle Reynolds numbers. A wake developes in the aft of the sphere and increases the drag. In the absence of theoretical models, the Stokes drag is corrected by a multiplication factor Φ, determined empirically. The most well known correlation is the one by Schiller and Naumann (1933) in Equation 2.10. This expression remains valid with an accuracy of 5% for particle Reynolds numbers smaller than 800.

$$\Phi = 1 + 0.15 Re_p^{0.687} \tag{2.10}$$

The influence of the Stokes drag correction is illustrated in Figure 2.6. The corrected drag is 170% of the Stokes drag at a particle Reynolds number of 10, indicating that the finite Reynolds number correction cannot be neglected in accurate sphere motion analysis. If the Faxén term is neglected, the drag expression can be written in the more convenient form of $\mathbf{F}_d = C_d \frac{1}{2} \rho_f \, (\mathbf{u} - \mathbf{v_p}) \, |\mathbf{u} - \mathbf{v_p}| \, \pi a^2$ to find a corrected Stokes drag coefficient of $\frac{24}{Re_p}\Phi$. Additionally, Figure 2.6 shows the behavior of the drag coefficient in function of the particle Reynolds number.

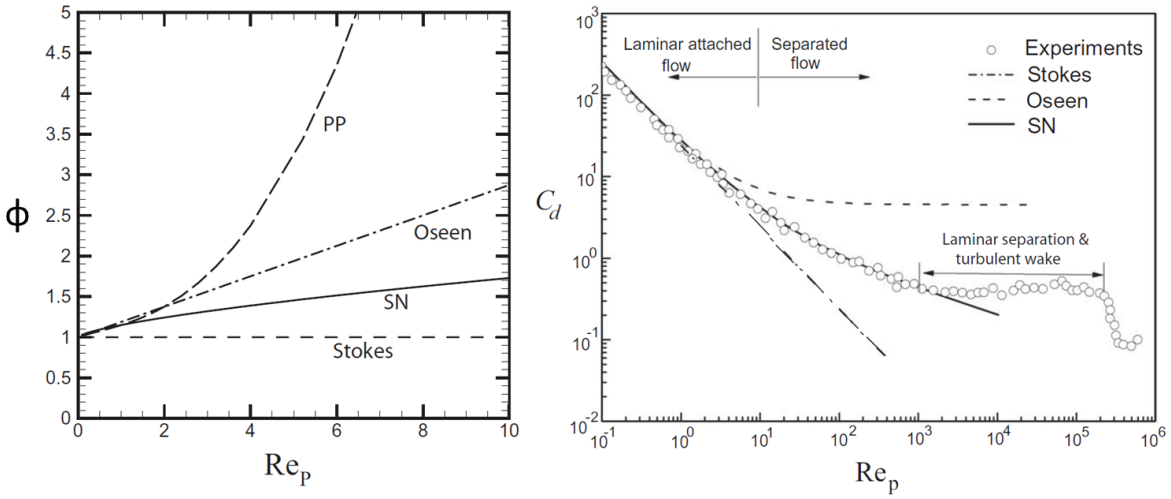

Figure 2.6: Sphere drag at finite particle Reynolds numbers with Stokes drag (Stokes), Oseen and Schiller and Naumann (SN). *Left*: Drag correction factor Φ. *Right*: Drag coefficient C_d. (Reproduced from Marshall and Li (2014).)

Gravity-Buoyancy Force

For particles with a density that differs from its surrounding fluid, the gravity will exert a force on the sphere. This force can be modelled by the mass difference of the sphere and air (based on an equivalent volume as the sphere) times the gravitational acceleration $\mathbf{g}$, as in Equation 2.11. For perfect neutral-buoyant particles, this force logically equals zero.

$$\mathbf{F}_{G-B} = \frac{4}{3}\pi a^3 \left(\rho_p - \rho_f\right) \mathbf{g} \tag{2.11}$$

Pressure Force

The pressure force or fluid-stress force is the force that a sphere experiences in a non-uniform pressure field due to the flow acceleration. If the viscous term is small compared with the inertial term, i.e. a high flow Reynolds number outside a boundary layer, the pressure gradient can be related to the fluid acceleration and the pressure force can be expressed as

$$\mathbf{F}_{FS} = \frac{4}{3}\pi a^3 \rho_f \frac{D\mathbf{u}}{Dt}. \tag{2.12}$$

Added-Mass Force

The added-mass force or the virtual mass force is one of the unsteady forces acting on the particle. If a sphere is accelerating, it needs to accelerate not only the sphere itself, but also a certain amount of fluid in front of the sphere. This is felt like the sphere is carrying an extra mass. The added-mass force is inertia related and is therefore independent of the particle Reynolds number. The first expression was given by Batchelor (1967). Nowadays,

the added-mass force that was given in the inviscid, rotational equation of motion of a sphere by Auton et al. (1988) is preferred. It reads as

$$\mathbf{F}_{AM} = C_{am}\frac{4}{3}\pi a^3 \rho_f \left(\frac{D\mathbf{u}}{Dt} - \frac{d\mathbf{v}_p}{dt}\right) \tag{2.13}$$

where the added-mass coefficient C_{am} equals 0.5. The material derivative D/Dt is defined following the fluid element path and the material derivative d/dt is calculated with respect to the particle path. The difference between the expressions of Batchelor (1967) and Auton et al. (1988) arises from the fact that Batchelor expressed the acceleration of the fluid element following the particle path. The added-mass force is purely inertial related and needs therefore no correction at finite Reynolds numbers.

History Force

The history force or the Basset force originates from the diffusion of the vorticity around the sphere. If a sphere accelerates, the flow field around the sphere will change as well. The history force accounts for the change in velocity gradient around the sphere. The history force is complex and is often neglected in analyses. No exact form of the force is available. An expression for the history term at low Reynolds numbers was obtained by Boussinesq (1885) and Basset (1888) as

$$F_H = 6\pi\mu_f a \int_{-\infty}^{t} K\left(t-\tau\right)\left(\frac{d\mathbf{u}}{d\tau} - \frac{d\mathbf{v}_p}{d\tau}\right) \mathrm{d}\tau, \tag{2.14}$$

where $K\left(t-\tau\right)$ is a Kernel function, that is given by

$$K\left(t-\tau\right) = \left[\frac{a^2}{\pi\nu_f\left(t-\tau\right)}\right]^{\frac{1}{2}}. \tag{2.15}$$

The Kernel function was modified by Mei (1993) to account for particles at finite Reynolds numbers. The modification is that the behavior of the short decay can indeed be modeled with $(t-\tau)^{-1/2}$, but the decay at large time is modeled by $(t-\tau)^{-2}$ instead of $(t-\tau)^{-1/2}$. This Kernel function is an approximation and is not exact. Mei (1996) reports that *"the equations are reliable, robust, accurate at small time, and qualitatively correct at large times over a large range of Reynolds numbers* [1] *"*. This Kernel function can be used up to a particle Reynolds number of 173. At higher Reynolds numbers, three-dimensional effects start to develop and the motion cannot be considered as two-dimensional anymore. The Kernel function approximation is given as

$$K\left(t-\tau\right) \approx \left\{\left[\frac{\pi\left(t-\tau\right)\nu_f}{a^2}\right]^{1/4} + \left[\frac{\pi}{2}\frac{\left|\mathbf{u}\left(\tau\right)-\mathbf{v}_p\left(\tau\right)\right|^3}{a\nu_f f_H^3\left(Re_p\right)}\left(t-\tau\right)^2\right]^{1/2}\right\}^{-2}, \tag{2.16}$$

where the function f_H is given by $f_H\left(Re_p\right) = 0.75 + 0.105Re_p$.

[1] Citation of Mei (1996), page 4.

Transverse Lift Force

Spherical particles in an unidirectional motion in a shear field or rotating in an uniform flow field, will experience a transverse lift force. The velocity difference on top and at the bottom of the sphere causes a pressure difference and a transverse motion towards the higher velocity region.

Due to shear
The outward displacement of spherical particles in shear was observed first by Segré and Silberberg (1962). They noticed that neutrally-buoyant particles in Pouseille flow migrated away from the wall to an equilibrium position.

One of the first, but still the most used theoretical model to quantify the transverse lift force of a spherical particle in linear shear is the one by Saffman (1965, 1968). In his zeroth-order asymptotic expansion, he assumed that the Reynolds numbers based on the particle slip velocity $Re_p = \rho_f |\mathbf{u} - \mathbf{v}_p| a/\mu_f$, on the particle rotation $Re_\Omega = \rho_f \Omega a^2/\mu_f$ and on the shear $Re_G = \rho_f G a^2/\mu_f$ are all small compared to unity and that the slip Reynolds number Re_p is small with respect to the square root of the shear Reynolds number $Re_G^{1/2}$. Then, the Saffman lift force is given by

$$\mathbf{F}_L = 6.46 \mu_f a^2 |\mathbf{u} - \mathbf{v}_p| \left| \frac{d\mathbf{u}}{dy} \right|^{\frac{1}{2}} \nu_f^{-\frac{1}{2}}, \tag{2.17}$$

with the force pointing from the lower velocity side towards the higher velocity side. The contribution of particle rotation is not included in the zeroth-order term and is thus, according to Saffman, small compared to the shear induced lift force. If the inner expansion is evaluated to the first order, the Saffman lift equation becomes

$$\mathbf{F}_L = 6.46 \mu_f a^2 |\mathbf{u} - \mathbf{v}_p| \left| \frac{d\mathbf{u}}{dy} \right|^{\frac{1}{2}} \nu_f^{-\frac{1}{2}} + \pi \rho_f a^3 |\mathbf{u} - \mathbf{v}_p| \left(\Omega - \frac{11}{8\pi} \left| \frac{d\mathbf{u}}{dy} \right| \right). \tag{2.18}$$

The second term of this last equation is usually small compared to the first term and therefore, Equation 2.17 is more commonly used and will be referred as the Saffman lift force. McLaughlin (1991) was able to remove the assumption in Saffman's expression that $Re_p < \sqrt{Re_G}$. He proved theoretically that the Saffman lift force becomes

$$\mathbf{F}_L = 6.46 \mu_f a^2 |\mathbf{u} - \mathbf{v}_p| \left| \frac{d\mathbf{u}}{dy} \right|^{\frac{1}{2}} \nu_f^{-\frac{1}{2}} 0.433 J(\epsilon), \tag{2.19}$$

where ϵ is defined as the ratio of $\sqrt{Re_G}/Re_p$. The values of $J(\epsilon)$ should be numerically evaluated and are given in tabular form in McLaughlin (1991). McLaughlin provided two asymptotic approximations for the function $J(\epsilon)$ in the lower and upper limit. This is, $J(\epsilon) = 2.255 - 0.6463/\epsilon^2$ for $\epsilon \gg 1$ and $J(\epsilon) = 32\pi^2 \epsilon^5 \ln\left(\epsilon^{-2}\right)$ for $\epsilon \ll 1$. Based on the numerical tabular values of McLaughlin (1991), Mei (1992) made a correlation of the function $J(\epsilon)$, valid for $0.1 \leq \epsilon \leq 20$:

$$J(\epsilon) = 0.6765 \{1 + \tanh[2.59 \log_{10} \epsilon]\} \{0.667 + \tanh[6(\epsilon - 0.32)]\}. \tag{2.20}$$

Dandy and Dwyer (1990) performed numerical simulations of a sphere in a linear shear field at finite particle Reynolds numbers ($0.1 \leq Re_p \leq 100$). Based on these results and on the analytical expression by Saffman (1965), Mei (1992) derived a correlation for the lift force of a sphere in linear shear:

$$\frac{\mathbf{F}_L}{\mathbf{F}_{L,Saff}} = \begin{cases} \left(1 - 0.3314\alpha^{\frac{1}{2}}\right) e^{-\frac{Re_p}{10}} + 0.3314\alpha^{\frac{1}{2}} \\ 0.0524\left(\alpha Re_p\right)^{\frac{1}{2}} \end{cases} \tag{2.21}$$

where $\alpha = Re_G/Re_p$. The results so far assumed a small particle rotation Reynolds number and therefore, the influence of the particle's rotation was always neglected. The particles under investigation are assumed to be freely-rotating. In a linear shear flow, the velocity difference on top and on the bottom of the particle will apply a torque and the particle will start rotating. The effect of the rotation on the transverse lift force will be investigated separately.

Due to rotation

The displacement due to rotation of a sphere with a relative velocity in a fluid was examined first by Magnus (1853). The so-called Magnus effect is quantified for particle Reynolds numbers small compared to unity by the expression of Rubinow and Keller (1961) with $C_s = 1$:

$$\mathbf{F}_L = C_s \pi \rho_f a^3 \left(\mathbf{u} - \mathbf{v}_p\right) \times \boldsymbol{\Omega}. \tag{2.22}$$

However, this equation tends to overpredict the lift force compared to experimental and numerical results. Different values for a lower coefficient C_s are available in literature; numerical simulations of rotating and non-rotating spheres in a linear shear flow were performed by Bagchi and Balachandar (2002) and accurate results were achieved for $C_s = 0.55$. The relative rotation $\boldsymbol{\Omega}$ of the particle is influenced by the rotation of the particle $\boldsymbol{\Omega}_s$ and the rotation of the velocity field. The relative rotation can be defined as $\boldsymbol{\Omega} = \boldsymbol{\Omega}_s - 0.5\nabla \times \mathbf{u}$. For a linear shear field, this simplified to $\boldsymbol{\Omega}_s - 0.5G$. However, the torque-free rotation rate of a freely-rotating sphere is different than the rotation rate $\Omega_f = G/2$. The extended version of the Saffman lift force (Equation 2.18) contains the term $\Omega_s - \frac{11}{8\pi}G$ or $\Omega_s - 0.4377G$. A correlation between the rotation rate Ω_f and the torque-free rotating rate Ω_{st} is given by Bagchi and Balachandar (2002):

$$\frac{\Omega_{st}}{\Omega_f} = \begin{cases} 1 - 0.03464 Re_p^{0.95} \\ 1 - 0.0755 Re_p^{0.455} \end{cases} \tag{2.23}$$

In the same work, Bagchi and Balachandar (2002) concluded that the combined lift force of a freely-rotating particle in shear can be approximated with the sum of a non-rotating particle in shear and a rotating particle in uniform flow. However, the influence of the rotation is small, such that its effect on the sphere's trajectory is negligible.

2.4.2 Tracing fidelity

An ideal particle should behave identical as an infinitesimal fluid flow element, such that the particle velocity equals the fluid velocity. However in practice, ideal particles do not exist

and all tracer particles have a finite slip velocity. Neglecting external forces (gravitational, transverse lift, centrifugal and electrostatic), Melling (1997) found out that the tracing capabilities of particles in creeping flow is a function of the particle shape, particle diameter d_p, particle density ρ_f, fluid density ρ_f and fluid viscosity μ_f. Extending this model to finite particle Reynolds numbers, the slip velocity $\mathbf{u}_s$ or the difference between the fluid and particle velocity can be modelled as:

$$\mathbf{u}_s = \mathbf{u} - \mathbf{v}_p = d_p^2 \frac{(\rho_p - \rho_f)}{18\mu_f \Phi} \frac{d\mathbf{v}_p}{dt} \tag{2.24}$$

This expression can be derived from the equation of motion (Equation 2.7) by assuming that the particle acceleration $d\mathbf{v}_p/dt$ equals the fluid flow acceleration $D\mathbf{u}/Dt$. It shows that a tracer particle will only have zero slip and thus perfectly follow the fluid flow if the particle acceleration is zero (totally irrelevant in aerodynamics) or when the particle is neutrally buoyant. In all other cases, the particle will react with a delay to a change in the fluid flow velocity. In Stokes regime (that is $\Phi \to 1$), Equation 2.24 reads as a first order differential equation and has a single exponential decay with characteristic time τ_p:

$$\tau_p = d_p^2 \frac{(\rho_p - \rho_f)}{18\mu_f \Phi} \tag{2.25}$$

The particle relaxation time τ_p can be interpreted as the time it takes for the particle to change its velocity, after a sudden change in fluid velocity, to $1 - e^{-1} = 63\%$ of the new fluid velocity. This is visualised in Figure 2.7.

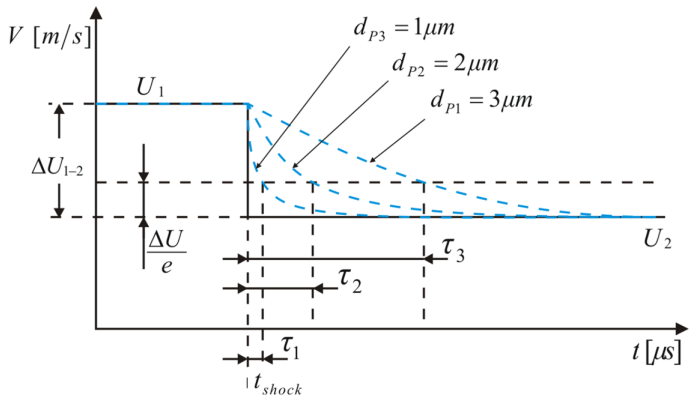

Figure 2.7: Exponential decay after velocity step change (reproduced after Scarano (2013b)).

However, at finite particle Reynolds numbers Equation 2.24 becomes non-linear and will no longer be a constant for a given particle. Although the exponential decay can only be defined for heaver-than-air particles, a negative characteristic time can still be used as a measure to quantify the behavior of lighter-than-air particles. The relaxation time should be small in order to have faithful tracing behaviour. The Stokes number St, defined as the ratio of the particle relaxation time τ_p over the flow characteristic time τ_f, should be smaller than 0.1 (Samimy and Lele, 1991) to guarantee faithful tracing behaviour.

$$St = \frac{\tau_p}{\tau_f} \tag{2.26}$$

2.4.3 Commonly used tracer particles

An overview of tracer particles commonly used in PIV experiments in air is given in Table 2.2. In most experiments, micron-sized liquid droplets with a density in the order of 1000 kg/m^3 are used as flow tracers. These types of particles have a typical relaxation time between 1 and 20 μs. Ceramic materials (TiO_2 and Al_2O_3) are used for flows at high temperature, due to their inertness and high melting point. TiO_2 particles are favored for high-speed applications due to their low relaxation time (Ragni et al., 2011). For large-scale measurements the use of helium-filled soap bubbles is showing promising results (see Figure 2.3). In experiments performed in water, it is much easier to match the neutral buoyancy condition and particle diameters in the order of 50 μm can be used to increase the amount of scattered light.

Table 2.2: Tracer particles for PIV experiments in air.

Material	d_p [μm]	ρ_p [kg/m^3]	τ_p [μs]	Reference
DEHS	1	912	2	Kähler et al. (2002)
Olive oil	3	970	22.5	Melling (1997)
Hollow glass	1.67	2600	22.6	Melling (1997)
Helium-filled soap bubbles	100-2000	≈1.225	11-42	Scarano et al. (2015)
TiO_2	0.01	4230	0.4-3.7	Ragni et al. (2011)
Al_2O_3	0.3	4000	20-28	Urban and Mungal (2001)

The discussion on tracer particles can be summarized as follows: particles should be small enough to faithfully follow the flow, but should be big enough to reflect a sufficiently amount of light. In order to enable large-scale PIV applications, bigger particles are needed. The increase in particle diameter can only be compensated by making the particles more buoyant. Helium-filled soap bubbles are the most suitable particles approaching the neutral-buoyancy condition for experiments in air, while being two orders of magnitude bigger than the present micron-sized tracer particles.

2.5 Helium-filled soap bubbles

2.5.1 Overview of earlier applications

The idea of using HFSBs as flow tracers dates back to 1928, when Lock mentioned the option of using HFSBs for qualitative flow visualization around an airscrew. Only in 1936, the first application of flow visualisation with HFSBs in a wind tunnel is reported by Redon and Vinsonneau (1936). Since then, many flow visualization experiments are conducted, among others: the flow around a parachute (Pounder, 1956; Klimas, 1973), around an airfoil (Hale et al., 1971a), wing-tip vortices (Hale et al., 1971b) and the rotor-ground interaction of a helicopter model (Empey and Ormiston, 1984). Due to the aerodynamic uncertainty of the bubbles, most of the applications were limited to qualitative flow visualization only.

More recently, Kerho and Bragg (1994) studied the accuracy of HFSBs as flow tracers in the stagnation region of a NACA00012 airfoil. Bubbles with diameter varying between 1 and 5 mm were generated. However, the trajectories of non-neutral buoyant bubbles showed a clear departure from the streamlines of the airflow (see Figure 2.8). The conclusion was that HFSBs did not qualify for quantitative measurements in aerodynamics.

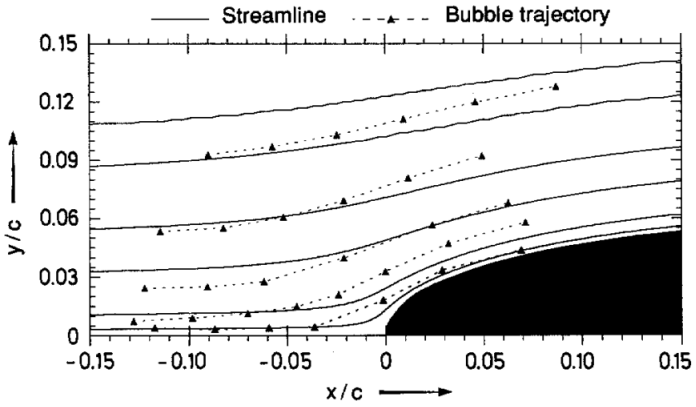

Figure 2.8: HFSBs trajectories of the experiment by Kerho and Bragg (1994).

Therefore, HFSBs have mainly been used in convective flow studies, typically with low velocities (< 1 m/s). Müller et al. (2000) investigated the flow inside an aircraft cabin using 2-mm-sized HFSBs with planar PIV with a field of view of $2 \times 2,5$ m^2. Müller et al. (2001) obtained 3C velocity vectors in a plane with particle streak tracking (PST) with HFSBs of 1-2 mm in diameter. Machacek (2003) applied particle streak velocimetry in a large wind tunnel using helium-filled soap bubbles, but the particle concentration of 5-10 bubbles particles/frame was rather low. The flow in an aircraft cabin was investigated by Sun et al. (2005) by means of particle streaking velocimetry in a measurement volume of $4.7 \times 2.1 \times 1.8$ m^3 with bubbles diameters ranging from 1.3 to 3 mm. Lobutova et al. (2009) achieved a 3D PTV measurement volume of 140 m^3 in Rayleigh-Bénard convection cell using HFSBs of 4 mm.

Bosbach et al. (2009) introduced a novel bubble generator developed by the German Aerospace Center (DLR), capable of producing bubbles of 0.2 to 0.6 mm at a high rate (50,000 bubbles/s). Planar PIV measurements on the mixed convective flow in a full scale airplane cabin mock-up (measurement domain of 7 m^2) demonstrated their effectiveness as flow tracers at large scale. A large-scale tomographic application is reported by Kühn et al. (2011) addressing the three-dimensional flow field in a rectangular convective cell over a volume of $75 \times 45 \times 16.5$ cm^3. Tomographic PIV measurements in a wind tunnel were conducted by Scarano et al. (2015), where the faithful tracing behavior of the bubbles in the stagnation region of a cylinder was studied. A demonstration experiment was also carried out where time-resolved tomographic PIV was employed to describe the large-scale velocity field in the wake of a cylinder in a volume of $20 \times 20 \times 12$ cm^3. Subsequently, Caridi et al. (2015) developed a dedicated seeding system to increase the concentration of tracers in large-scale experiments (measurement volume of 16,000 cm^3) involving a vertical axis wind turbine. Schneiders et al. (2016) have reconstructed the flow pressure in the wake of a cylinder by large-scale tomo-PIV measurements with HFSBs.

2.5.2 Bubble generator

Helium-filled soap bubbles are produced with an orifice type nozzle. This type of nozzle was invented by Okuno et al. (1993) in his search for a bubble generator with a higher production rate (up to 3,000 bubbles/s with a diameter of 1-2 mm) than the existing pitot tube nozzles (Figure 2.9). Improvements in the nozzle design by Müller et al. (2000) resulted in an increase of production rate by a factor 5. A comprehensive description of the latest nozzle design by the German Aerospace Center is given by Bosbach et al. (2009), reporting a stable production of sub-millimeter HFSBs at a rate of 50,000 bubbles/s. A schematic overview of this nozzle is given in Figure 2.10-left.

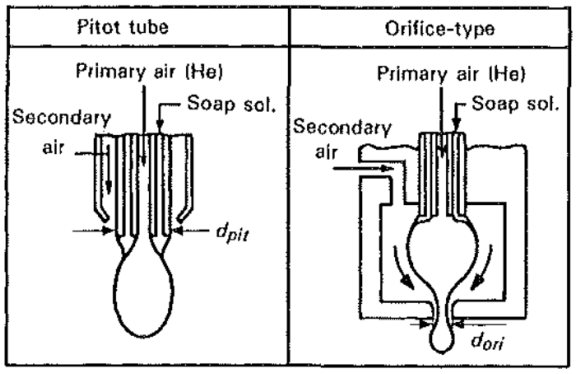

Figure 2.9: Initial nozzle design by Okuno et al. (1993).

The orifice type nozzle consists of two co-axial tubes with different diameter. Helium flows through the inner tube and a bubble fluid solution (BFS) through the outer tube. A secondary airflow (SA) forces the cylindrical column of soap with helium inside out of the cap and cuts the column into bubbles in the orifice. The diameter of the bubbles can be tuned by changing the orifice diameter and/or the mass flow rate of the secondary airflow. The mass flow rates of the bubble fluid solution and the helium needs to be adjusted properly to assure neutral buoyancy and stable production. The mass flow rates of the helium, BFS and air flow are controlled by a fluid supply unit (FSU). The operation principle of the FSU is depicted in Figure 2.10-right. Pressurized helium is filtered and flows through a fine pressure regulation valve straight to the nozzle. The pressurized air is split up into two different supply lines after passing a filter. The first line consists of a fine pressure regulation valve and feeds the secondary air flow channels in the nozzle. The second line with another fine pressure regulation valve, is used to pressurize the soap pressure tank and is connected with the BFS channels. A parallel air line around the pressure tank offers the ability to purge the soap channels in the nozzle with air. A return channel is used to drain redundant BFS when using multiple nozzles.

Multiple nozzles need to be operated in parallel to increase the bubble concentration in a wind tunnel. When numerous nozzles are connected to a single FSU, nozzle interaction and different supply tube lengths will cause different pressure drops for each nozzle. This results in different mass flow rates per nozzle. Therefore, each nozzle is connected to three very thin capillary tubes (one for each fluid), before being attached to the supply tubes and the FSU.

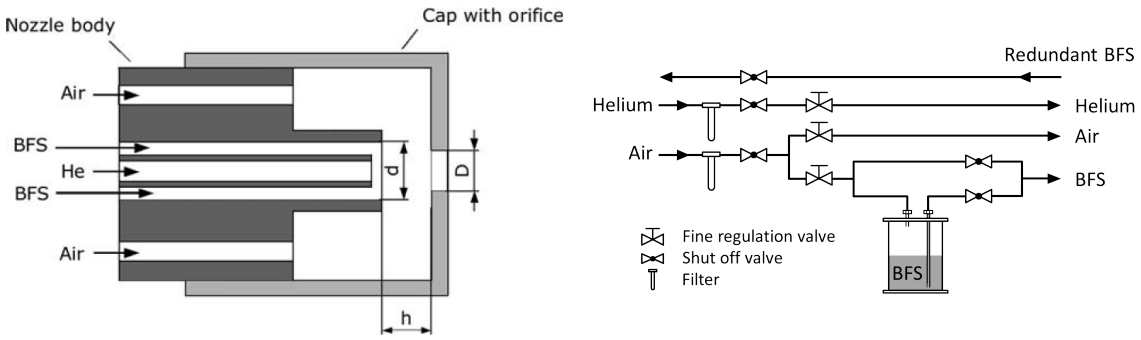

Figure 2.10: Bubble Generator System. *Left*: Pitot type nozzle (reproduced from Bosbach et al. (2009)). *Right*: Schematic overview of the fluid supply unit (FSU).

The pressure drop in the capillary tube is much bigger than any other pressure drop in the system, assuring the same mass flow rates of helium, BFS and air for each single nozzle. The nozzles are mounted in an aerodynamic rake to reduce the disturbance, introduced by the presence of the nozzles in the wind tunnel channel, to an absolute minimum. The influence of the presence of the rake and the secondary airflow of each single bubble generator (i.e. turbulence and added momentum) on the flow quality inside the wind tunnel is unclear at this moment and needs some further investigation.

2.5.3 Tracing fidelity

The survey in subsection 2.5.1 covers a lot of earlier applications on HFSBs. However, only two of them describe the aerodynamic behavior of HFSBs quantitatively. Kerho and Bragg (1994) analyzed the trajectories of 20 bubbles in the stagnation region of a NACA0012 airfoil at freestream velocity of 18 m/s. They determined the bubble density and diameter by comparing the experimental trajectories and the velocity profiles with potential-flow based numerical trajectory simulations. However, this approach could not provide a unique solution, since both the bubble diameter and density were unknown. They report widely scattered bubbles with specific densities (ρ_p/ρ_f) ranging from 0.3 to 1 and with diameters varying between 1 and 5 mm. Heavier-than-air bubbles were filtered by means of a vortex-filter.

Scarano et al. (2015) studied the tracing fidelity of the HFSBs in the stagnation region of a cylinder at freestream velocity of 30 m/s. They varied the mass flow rate of the helium and BFS supply until the bubble trajectories and velocity profiles coincidence with the reference solution that was measured by means of planar PIV with micron-sized fog droplets. The experimental results in Figure 2.11 show that the neutral buoyancy condition was achieved for volume flow rates of helium and BFS of respectively $Q_{He} = 5$ l/h and $Q_{BFS} = 5$ ml/h. However, their study focused only on the statistical mean relaxation time of a large amount of bubbles and did not investigate any variance in bubble diameter. Therefore, questions remain open on the individual, aerodynamic bubble behaviour, on the dispersion in terms of diameter and density and on the influence of the second airflow (SA) in the nozzle.

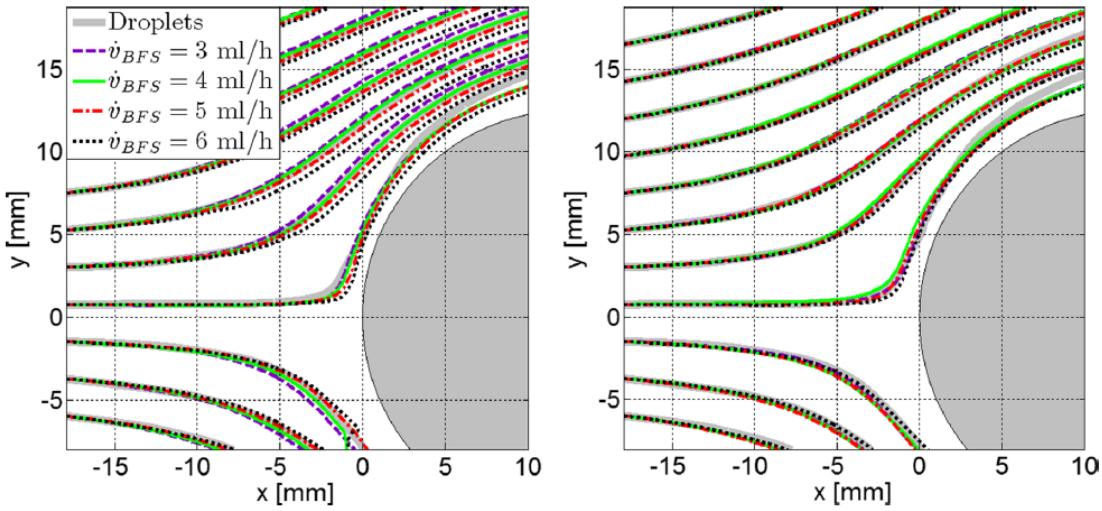

Figure 2.11: Time averaged streamlines at $U_\infty = 30$ m/s obtained with micron-sized droplets and HFSBs with four different volume rates of BFS and two volume rates of helium: $Q_{He} = 4$ l/h (left) and $Q_{He} = 5$ l/h (right). Streamlines are determined by cross-correlation analysis (reproduced from Scarano et al. (2015)).

2.5.4 Optical properties

Helium-filled soap bubbles have special optical properties compared to other tracer particles. The scattering properties of micron-sized particles are typically characterized by the Mie scattering theory (since $d_p \approx \lambda$), whereas the optical properties of helium-filled soap bubbles with a nominal diameter of 300 μm are analyzed by means of geometrical optics ($d_p \gg \lambda$). Geometrical optics describes the light propagation in terms of light rays.

A light ray has to pass through a thin bubble fluid solution (BFS) film with a refractive index approximately the same as water $n = 1.333$ and through the inner part of the bubble filled with helium with a refractive index of $n = 1.000036$, which is close the refractive index of the surrounding fluid (air, $n = 1.0001$). It is assumed that the soap film is so thin that the light ray deflection due to passing through it is negligible and that the difference in refractive indices of helium and air can be neglected. Therefore, a helium-filled soap bubble can -from an optical point of view- be approximated with a homogeneous air sphere with an infinitesimal, transparent coating.

Each light ray will reflect and refract upon passing through the soap film. These reflections and refractions will create intensity maxima when viewed from a certain direction and are called glare points. These glare points are the reflected ray and first-order refraction as seen from a certain angle (Figure 2.12). The glare points were investigated by van de Hulst and Wang (1991) by means of a light ray study. They found out that the distance between the glare points depends on the angle of the imaging system with respect to the illumination direction, the refractive indices in and outside the bubble and on the bubble diameter.

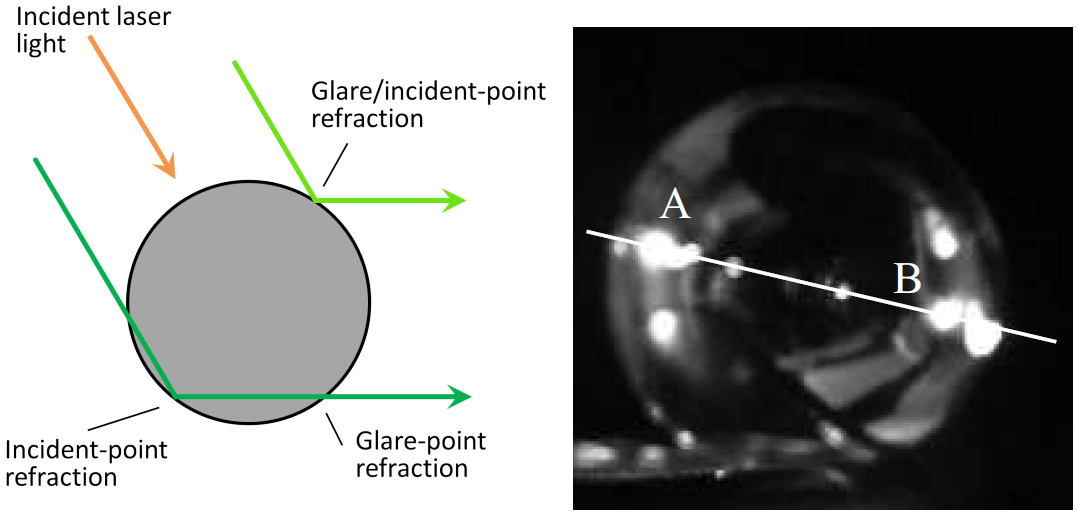

Figure 2.12: Glare points explained by light rays in a HFSB. *Left*: Schematic view of glare points (reproduced after Tropea (2011)). *Right*: Glare points as seen by eye (Machacek, 2003).

Chapter 3

Theoretical analysis

In this chapter a theoretical approach will be used to address the tracing fidelity of helium-filled soap bubbles (HFSBs). Section 3.1 starts off with a physical model of HFSBs and links the physical properties of the bubbles to the production process. In section 3.2 the equation of motion of a spherical particle is analysed and simulated to investigate which forces need to be taken into account to characterize the aerodynamic behaviour of the HFSBs.

3.1 Bubble physics, production and behaviour

It is convenient to define the *specific density* $\bar{\rho}$ of a tracer particle. The specific density is the ratio of the particle density over fluid density. A specific density of 1 means the particle is neutrally buoyant, larger than 1 means the particle is heavier than its surrounding fluid, a value smaller than 1 means lighter than the fluid. This is defined as:

$$\bar{\rho} = \frac{\rho_\mathrm{p}}{\rho_\mathrm{f}} \tag{3.1}$$

where the subscript f is the abbreviation for the surrounding fluid. From a physical point of view, a helium-filled soap bubble can be modelled by a thin-walled sphere with radius a and wall thickness t. The total mass of a helium-filled soap bubble can then be split up in the mass of the bubble fluid solution (i.e. the thin soap film) and the helium inside the bubble and reads as

$$\underbrace{\frac{4}{3}\pi a^3 \rho_p}_{m_\mathrm{p}} = \underbrace{\frac{4}{3}\pi \left(a^3 - (a-t)^3\right) \rho_\mathrm{bfs}}_{m_\mathrm{bfs}} + \underbrace{\frac{4}{3}\pi (a-t)^3 \rho_\mathrm{helium}}_{m_\mathrm{helium}} \tag{3.2}$$

where the subscripts *bfs* and p stand for bubble fluid solution and particle respectively. With some mathematical manipulation, Equation 3.2 can be rewritten to find the specific density

of the particle when the bubble radius and film thickness are known:

$$\bar{\rho} = \frac{\rho_{\text{bfs}}}{\rho_{\text{f}}} + \left(1 - \frac{t}{a}\right)^3 \left(\frac{\rho_{\text{helium}}}{\rho_{\text{f}}} - \frac{\rho_{\text{bfs}}}{\rho_{\text{f}}}\right) \tag{3.3}$$

The soap film thickness can be retrieved from the same equation, if the bubble mass and radius are known. Then the soap film thickness is given by Equation 3.4. It scales linearly with the radius and with the cube root of the particle density.

$$t = a\left(1 - \sqrt[3]{\frac{\rho_{\text{p}} - \rho_{\text{bfs}}}{\rho_{\text{helium}} - \rho_{\text{bfs}}}}\right) \tag{3.4}$$

The density of helium ρ_{helium} inside the bubble can be determined from the ideal gas law and the Young-Laplace equation. The latter assumes a static equilibrium between the surface tension γ_{bfs} in the soap film and the pressure load exerted by the gas inside the bubble on the soap film. Then the density of helium inside the bubble is obtained by:

$$\rho_{\text{helium}} = \frac{M_{\text{helium}}}{RT}\left(p_\infty + \frac{4\gamma_{\text{bfs}}}{a}\right) \tag{3.5}$$

where M_{helium} is the molar mass of helium and R is the universal gas constant. It is expected that the influence of the surface tension to the density of helium is negligible, since that the freestream pressure p_∞ is few orders of magnitude larger than the ratio surface tension over particle radius γ_{bfs}/a. The density of the surrounding fluid, in case of wind tunnel experiments this will be air, can be calculated from the ideal gas law:

$$\rho_{\text{f}} = \frac{M_{\text{air}} p_\infty}{RT} \tag{3.6}$$

The density of the BFS mixture ρ_{bfs} is measured to be 1,130 kg/m^3 and is assumed to be insensitive for changes in temperature and/or pressure. The exact surface tension of soap is unknown, but can be assumed to be 30 mN/m (the surface tension of soapy water according to Soapbubble.dk (2016)). The molar mass M of air and helium is respectively 28.97 and 4.03 g/mol. The universal gas constant R equals 8.31446 J/(mol·K).

3.1.1 Bubble physics: helium-filled soap bubbles

With the help of Equation 3.3, some insight can be gained in which combinations of helium-filled soap bubble diameters and film thicknesses form particles with certain specific densities (Figure 3.1-left). The calculation is done at standard atmospheric conditions. For a neutrally buoyant bubble with a diameter between 300 and 400 μm, the soap film thickness varies roughly between 45 and 65 nm. The same soap thicknesses for a given diameter of 350 μm can give variations in the specific density $\bar{\rho}$ between 0.85 and 1.15. Figure 3.1-right illustrates the mass of the helium in the inner part of the bubble (dotted line) and the mass of the BFS mixture for different specific densities (solid lines) in function of the bubble diameter. It shows that the mass variations of an individual bubble with a given diameter is solely determined by variations in the amount of BFS mass. Furthermore, for neutrally buoyant HFSBs the soap mass is roughly one order of magnitude larger than the helium mass.

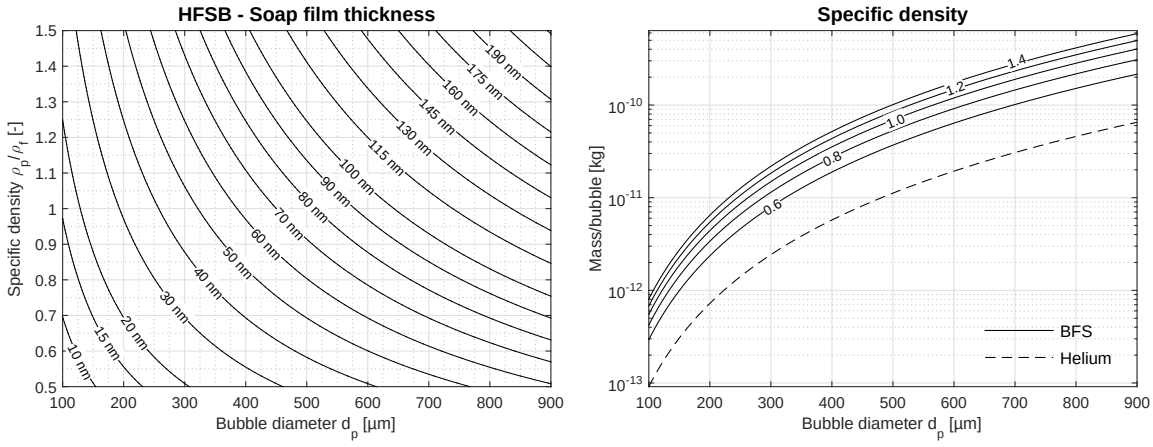

Figure 3.1: HFSB physics. *Left*: Soap film thickness (contour lines) in function of the bubble diameter d_p and specific density $\bar{\rho}$. *Right*: Mass of the soap film and helium inside a bubble in function of the bubble diameter d_p and the specific density $\bar{\rho}$ (contour lines).

3.1.2 Bubble physics: air-filled soap bubbles

The same analysis can be performed for air-filled soap bubbles (AFSBs), where the inside of the bubble is filled with air instead of helium. Logically, every air-filled soap bubble will be heavier than air. The analysis is again performed at standard atmospheric conditions. For a bubble with a diameter between 300 and 400 μm and a soap film thickness between 45 and 65 nm respectively (i.e. the neutrally buoyant condition for HFSBs), the specific density of an AFSB varies between 1.8 and 1.9 (Figure 3.2-left). The BFS and air mass of an individual AFSB is plotted in Figure 3.2-right. The dotted line that indicates the air mass lies on top of the solid line with specific density 2. This makes sense since the specific of air inside an AFSB equals 1 and in order to have a bubble with specific density 2, the mass of BFS and air should be equal. Air-filled soap bubbles are used to extend the range of feasible specific densities of the bubbles when studying the tracing fidelity of HFSBs. The remainder of this section will only focus on helium-filled soap bubbles.

3.1.3 Bubble production

The information of subsection 3.1.1 tells us more on which masses of BFS and helium are needed to create a bubble with a desired specific density. Ultimately, this information needs to be coupled to the fluid supply unit (FSU) settings. For a helium-filled soap bubble with a diameter of 400 μm and a specific density of 1, the mass ratio of helium over BFS equals 0.162. Logically, this ratio equals the mass flow ratio of helium over BFS as well and can thus be linked to the ratio of volume flow rates by:

$$\frac{Q_{\text{helium}}}{Q_{\text{bfs}}} = \frac{\dot{m}_{\text{helium}}}{\dot{m}_{\text{bfs}}} \frac{\rho_{\text{bfs}}}{\rho_{\text{helium}}} \tag{3.7}$$

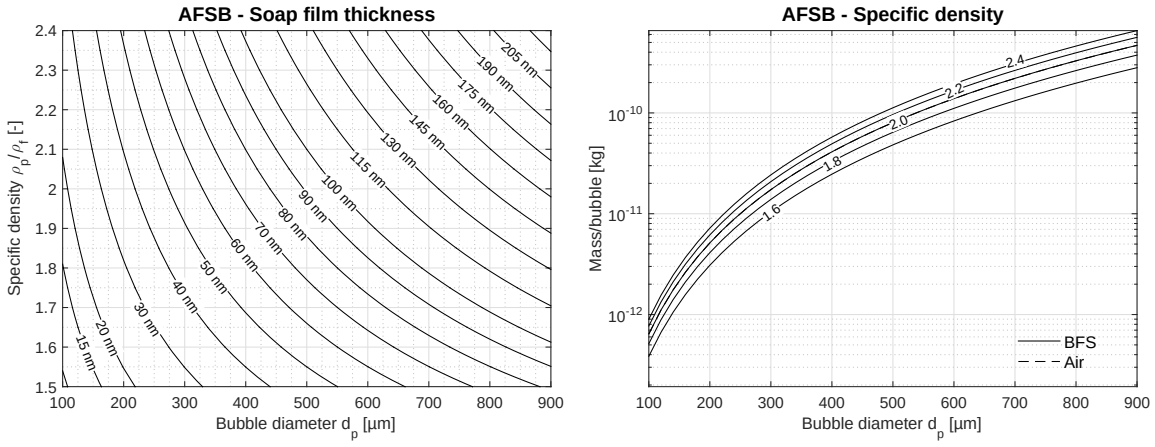

Figure 3.2: AFSB physics. *Left*: Soap film thickness (contour lines) in function of the bubble diameter d_p and specific density $\bar{\rho}$. *Right*: Mass of the soap film and helium inside a bubble in function of the bubble diameter d_p and the specific density $\bar{\rho}$ (contour lines).

giving a volume flow rate ratio of 1070.7. If this calculation is repeated for a range of bubble diameters and specific densities, it is possible to determine the theoretical mass and volume flow rates of a HFSB with any diameter and specific density. The results are shown in Figure 3.3. This calculation does not take into account whether the bubble generator is operating in a stable regime and consequently the reported flow rates might not be feasible in practice. Furthermore, it assumes that all the produced bubbles are perfectly homogeneous in diameter and density.

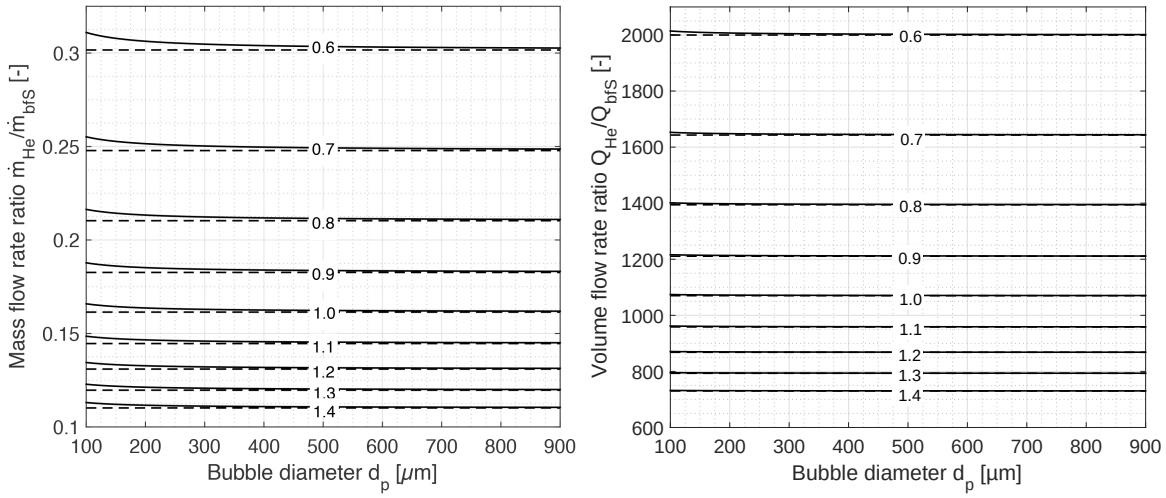

Figure 3.3: FSU flow rate ratios with solid lines as exact solution and dotted lines with surface tension influence neglected. *Left*: Specific density (contour lines) in function of the bubble diameter d_p and mass flow rate ratio $\dot{m}_{He}/\dot{m}_{bfs}$. *Right*: Specific density (contour lines) in function of the bubble diameter d_p and volume flow rate ratio Q_{He}/Q_{bfs}.

The solid lines in Figure 3.3 indicate the exact solution as given by Equations 3.3 through 3.6. It can be seen that the flow rate ratios are not constant for a given specific density for all bubble diameters. This is due to the pressure increase (and thus density increase) of the helium inside the bubble by the surface tension. The effect of neglecting this influence on the overall specific density of a bubble is small: less than 0.35 % for $d_p = 200$ μm, less than 0.15 % for $d_p = 400$ μm and less than 0.10 % for $d_p = 600$ μm. Therefore, Equation 3.5 can be simplified to the ideal gas law only. Those results are plotted in Figure 3.3 with dotted lines. The relation between the volume flow rate ratio Q_{He}/Q_{bfs} and the specific density of the HFSBs produced is therefore independent of the bubble diameter and is given by Figure 3.4.

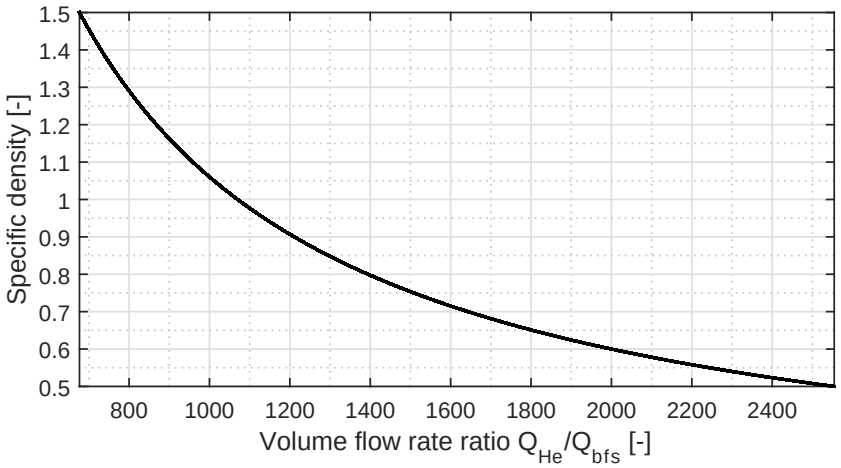

Figure 3.4: The specific density $\bar{\rho}$ of the HFSBs in function of the FSU volume flow rate ratio Q_{He}/Q_{bfs}.

3.1.4 Production rate

From the work of Scarano et al. (2015), it is known that the neutrally buoyant condition is achieved for volume flow rates of $Q_{He} = 5$ l/h and $Q_{bfs} = 5$ ml/h. This gives a volume flow rate ratio of 1000, according to Figure 3.4 this renders a specific density of approximately 1.05, so slightly heavier than air. In order to have perfect neutrally buoyant HFSBs, the flow rate of BFS should have been lowered to 4.67 ml/h. Since it is known how much helium and BFS a single bubble contains for a given diameter and specific density, it is possible to estimate the production rate of the bubble generator from the supply volume rates. For $Q_{He} = 5$ l/h and $Q_{bfs} = 4.67$ ml/h, the production rate is plotted in Figure 3.5.

For constant volume fow rates the production rate logically depends on the bubble diameter. The diameter of the HFSBs is mainly a function of the orifice diameter of the nozzle and the flow rate of the secondary airflow inside the nozzle. Also the flow rate of the helium has a small effect on the HFSB diameter. At the moment of writing, the exact relation between the flow rates of the secondary airflow and helium and the HFSB diameter is still

unknown. The bubbling process in co-flow is a popular research topic with two fluids, but only little information exists on the process in a three-fluid flow configuration. LaVision GmbH is experimentally investigating the effect of the supply flow rates on the bubble diameter.

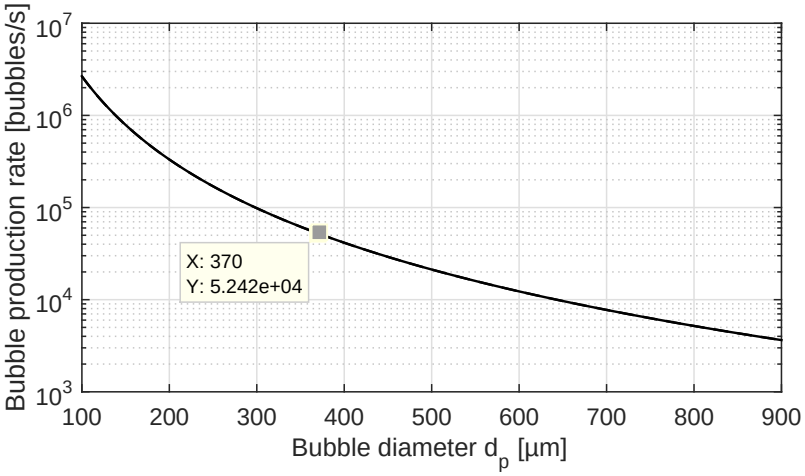

Figure 3.5: Theoretical relation between the FSU supply volume flow rates of helium over BFS and the specific density $\bar{\rho}$ of the HFSBs.

3.1.5 Settling velocity

In absence of external forces expect gravity, if a particle is released with zero initial velocity in a stagnant fluid, it will rise, float or sink depending on the density difference between fluid and particle. If the densities of the particle and fluid are not identical, the particle's velocity will increase until it has developed a constant settling velocity with respect to the fluid. This can be modelled by neglecting all forces of the equation of motion (Equation 2.7) except for the drag force and the gravity-buoyancy force. When the particle will have a constant slip velocity, those two forces are in equilibrium. The particle slip velocity reads then as:

$$\mathbf{u}_\mathrm{s} = \mathbf{u} - \mathbf{v}_\mathrm{p} = \underbrace{\frac{d_p^2}{18}\frac{(\rho_\mathrm{p} - \rho_\mathrm{f})}{\mu_\mathrm{f}}\frac{1}{\Phi\left(Re_p\right)}}_{\tau_p}\mathbf{g} = \underbrace{\frac{\bar{\rho}-1}{\bar{\rho}}\frac{\tau_0}{\Phi\left(Re_p\right)}}_{\tau_p}\mathbf{g} \tag{3.8}$$

where $\mathbf{g}$ is the gravitational acceleration. The relation to the relaxation time τ_0 is further highlighted in section 3.2. As such, the relaxation time τ_p equals the ratio of the settling velocity over the gravitational acceleration. This relaxation time τ_p is a function of the drag correction term $\Phi\left(Re_p\right)$ and thus of the slip velocity $\mathbf{u}_\mathrm{s}$ itself. Therefore, the relaxation time is no longer a constant as assumed in the Stokes regime, where the correction factor equals 1. It means that the relaxation time for two identical particles subjected to different external accelerations will be different. This is illustrated in Figure 3.6. In this figure, the relaxation time is plotted for spheres with a diameter in the range between 100 μm and 900 μm and with a specific density between 0.75 and 1.25. The external accelerations are 9.81, 1,000, 10,000 and 100,000 respectively.

Figure 3.6 shows how the relaxation time goes down for a bubble with a given diameter d_p and specific density $\bar{\rho}$ for increasing external accelerations. This can be explained by the fact that a higher acceleration induces a higher slip velocity. The viscous drag term is a function of the slip velocity with a power higher than linearly. The higher drag will imply that the slip velocity will scale less than linearly for a linear increase in external acceleration, giving lower relaxation times at higher accelerations. In short: the higher drag at finite Reynolds number (the drag correction factor) has a favourable effect on the relaxation time. This does not necessarily mean that HFSBs are better tracers at higher accelerations, since flows with higher acceleration in general have a lower characteristic flow time τ_p. Therefore, the Stokes number St should be used to decide on the tracing capability for particles' settling velocity under different accelerations.

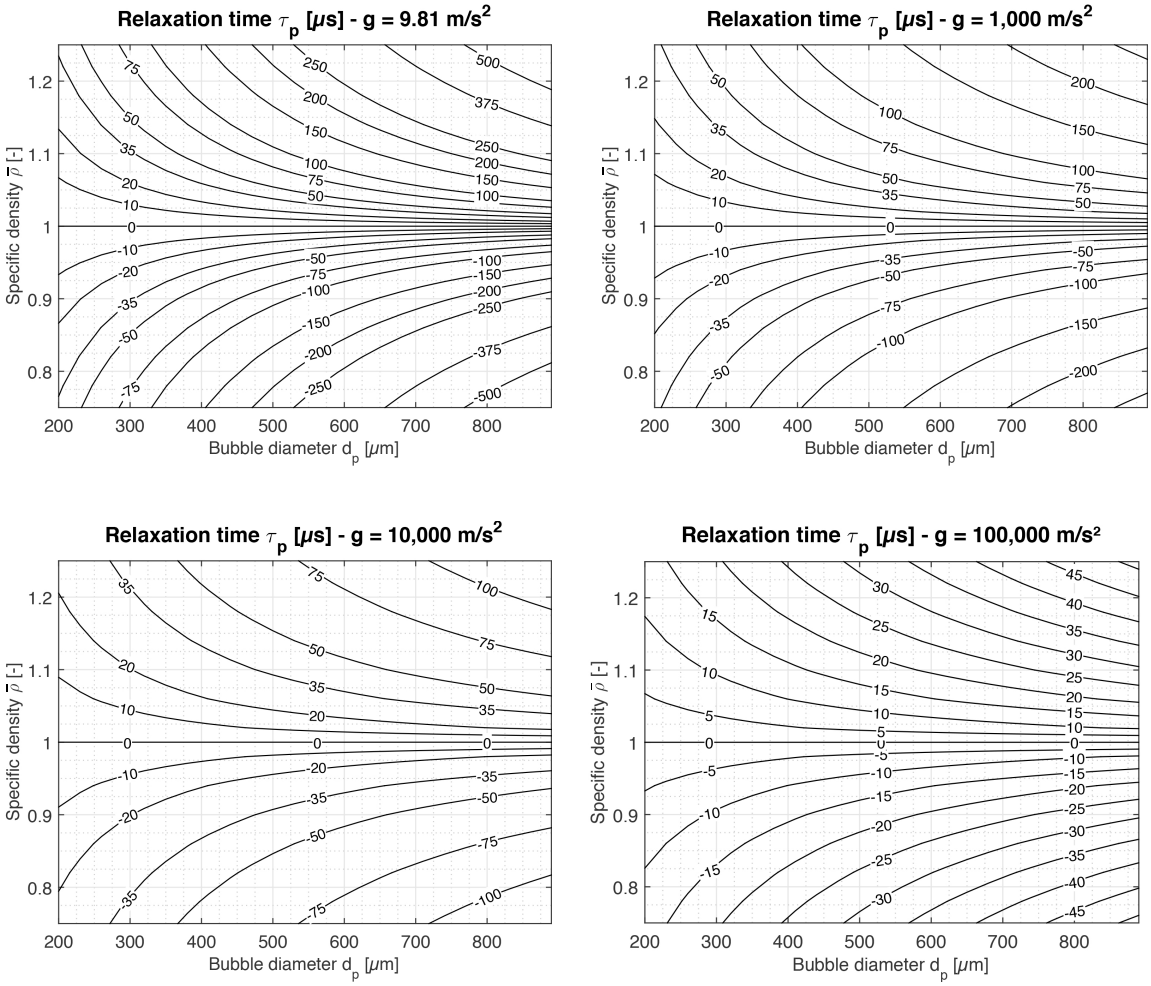

Figure 3.6: Relaxation time τ_p (contour lines) based on the settling velocity of spherical particles in stagnant air under different accelerations.

3.2 Tracing fidelity

The equation of motion will be analysed and simplified to study the present definition of the relaxation time. Furthermore, the trajectory of the bubbles will be simulated by means of a numerical simulation on the stagnation streamline in front of a cylinder to get to known which forces have to be accounted for to accurately predict the tracing fidelity of HFSBs.

3.2.1 Relaxation time

In order to derive an expression for the particle relaxation time τ_p the equation of motion of Mei (1996) that was introduced in section 2.4 is revisited. If the gravity force, the history force and the transverse lift force are neglected, the equation of motion of a particle at finite particle Reynolds number reduces to:

$$\frac{4}{3}\pi a^3 \rho_p \frac{d\mathbf{v}_p}{dt} = 6\pi a \mu_f \left(\mathbf{u} - \mathbf{v}_p\right) \Phi(Re_p) + \frac{2}{3}\pi a^3 \rho_f \left(\frac{D\mathbf{u}}{Dt} - \frac{d\mathbf{v}_p}{dt}\right) + \frac{4}{3}\pi a^3 \rho_f \frac{D\mathbf{u}}{Dt} \tag{3.9}$$

Neglecting the transverse lift force seems legitimate outside strong shear regions; inside a shear layer, this assumption is investigated with a dedicated experiment in chapter 6. Furthermore, the assumption is added that the difference in particle and fluid acceleration is small and can be neglected, as commonly done in the tracing fidelity theory. This is justified for faithful, micron-sized tracer particles: faithful tracers might exhibit a small velocity variation with respect to the fluid flow, but consequently the difference is acceleration will be even smaller and thus negligible. Then the particle acceleration can be substituted for the fluid acceleration or vice versa and Equation 3.9 simplifies to:

$$\frac{4}{3}\pi a^3 \rho_p \frac{d\mathbf{v}_p}{dt} = 6\pi a \mu_f \left(\mathbf{u} - \mathbf{v}_p\right) \Phi(Re_p) + \frac{4}{3}\pi a^3 \rho_f \frac{d\mathbf{v}_p}{dt} \tag{3.10}$$

Rearranging the terms gives on the left-hand side of Equation 3.11 the expression for the particle relaxation time and on the right-hand side the ratio of the slip velocity over the particle acceleration. Since both the slip velocity and particle acceleration can be extracted from the simulations and experiments, the relaxation time for each particle at each time instant can -under the given assumptions- be determined as:

$$\tau_p = \frac{d_p^2}{18}\frac{\rho_p - \rho_f}{\mu_f}\frac{1}{\Phi\left(Re_p\right)} = \frac{\mathbf{u} - \mathbf{v}_p}{\frac{d\mathbf{v}_p}{dt}} \tag{3.11}$$

According to this definition, the particle relaxation time τ_p can be negative. However, this would be a violation of its physical meaning. The relaxation time is defined as the time a particle needs to adjust its own velocity to the velocity of the surrounding fluid after a sudden change of the fluid velocity. The latter cannot be negative. This quantity can, however, still be useful to provide information on the aerodynamic behaviour of the particles. A negative value indicates the particle is lighter than its surrounding fluid and its magnitude is an indication of how much it deviates from neutral buoyancy. A positive value indicates a particle that is heavier than its surrounding fluid and is a measure of how much time it need to adapt

its velocity to the fluid velocity. Therefore, this work will stick to the definition as given in Equation 3.11. For particles in Stokes regime the drag correction factor Φ equals 1 and thus drops out of the relaxation time expression. For particles that are heavily heavier than its surrounding fluid, that is when $\rho_p >> \rho_f$, the term ρ_f can be neglected as well. This comes down to the fact that the fluid-stress force $\mathbf{F}_{\mathrm{FS}}$ is neglected in the equation of motion, giving a relaxation time τ_0:

$$\tau_0 = \frac{d_p^2}{18}\frac{\rho_p}{\mu_f} \tag{3.12}$$

The above theory is proved to be valid and useful to predict the tracing fidelity of micron-sized particles in PIV experiments in air. The main question that remains is whether the mentioned assumptions are still valid for helium-filled soap bubbles: particles that are nearly neutrally buoyant and that are two orders of magnitude larger. This will be investigated with numerical simulations of the equation of motion of the tracer particles.

3.2.2 Bubble trajectory simulator

In order to get to known which forces have to be accounted for to accurately predict the tracing fidelity of HFSBs, the trajectory of the bubbles will be simulated by means of a two-dimensional numerical simulation in a potential flow around a cylinder. The numerical simulation is performed in Matlab R2014b. The code is attached in Appendix A and is based on the discrete phase solver of the commercial CFD software ANSYS Fluent Inc. (2013).

The working principle is as follows. A helium-filled soap bubble with radius a and specific density $\bar{\rho}$ is introduced at a position $\mathbf{x_0}$ ahead of the cylinder. The particle is forced to have the same velocity as the velocity field on that position for two consecutive time instants. For the time instant after the first two, the bubble displacement and velocity is calculated based on the particle acceleration computed from the equation of motion. The equation of motion that is used the one of Mei (1996), that was discussed in section 2.4 and reads as:

$$m_p\frac{d\mathbf{v}_p}{dt} = \mathbf{F}_{QS} + \mathbf{F}_{G-B} + \mathbf{F}_{FS} + \mathbf{F}_{AM} + \mathbf{F}_H + \mathbf{F}_L \tag{3.13}$$

When the lift force and history force are neglected and both sides of Equation 3.13 are divided by the particle mass m_p, then the equation of motion becomes:

$$\frac{d\mathbf{v}_p}{dt} = \frac{18\mu_f}{\rho_p d_p^2}\Phi\left(Re_p\right)\left(\mathbf{u}-\mathbf{v}_p\right) + \frac{\left(\rho_p-\rho_f\right)}{\rho_p}\mathbf{g} + \frac{\rho_f}{\rho_p}\frac{D\mathbf{u}}{Dt} + \frac{\rho_f}{2\rho_p}\left(\frac{D\mathbf{u}}{Dt} - \frac{d\mathbf{v}_p}{dt}\right) \tag{3.14}$$

which can be simplified to a general form of a set of coupled ordinary differential equations:

$$\frac{d\mathbf{v}_p}{dt} = \frac{\Phi}{\tau_0}\left(\mathbf{u}-\mathbf{v}_p\right) + \mathbf{a} \tag{3.15}$$

The latter is a function of relaxation time τ_0 (Equation 3.12), which is not the same as the particle relaxation time τ_p, and the drag correction coefficient Φ. This work uses the correction factor by Schiller and Naumann (1933) and was discussed in subsection 2.4.1. The term $\mathbf{a}$

is the acceleration by all the force terms, except the drag force. Equation 3.15 needs to be integrated in time to find the new velocity and position of particle at the next time instant. The time integration of the equation of motion is performed according to the analytical scheme proposed in the theory guide of (ANSYS Fluent Inc., 2013), that was modified to incorporate the drag correction term Φ. It is a stepwise integration over discrete time steps. Assuming a constant $\mathbf{u}$, $\mathbf{a}$ and τ_0, an analytical integration yields that the velocity at time instant $n+1$ is given by

$$\mathbf{v}_{\mathrm{p}}^{n+1} = \mathbf{u}^n + e^{-\frac{\Delta t}{\tau_0}\Phi^n}\left(\mathbf{v}_{\mathrm{p}}^n - \mathbf{u}^n\right) - \mathbf{a}^n \frac{\tau_0}{\Phi^n}\left(e^{-\frac{\Delta t}{\tau_0}\Phi^n} - 1\right) \tag{3.16}$$

where the vector $\mathbf{a}^n$ due to the steady velocity field can be discretized as:

$$\mathbf{a}^n = \frac{(\rho_p - \rho_f)}{\rho_p}\mathbf{g} + \frac{\rho_f}{\rho_p}\mathbf{u}^n\nabla\mathbf{u}^n + \frac{\rho_f}{2\rho_p}\left(\mathbf{u}^n\nabla\mathbf{u}^n - \mathbf{v}_{\mathrm{p}}^n\nabla\mathbf{v}_p^n\right) \tag{3.17}$$

and the Nabla operator $\nabla\mathbf{u}^n$ is discretized by a first-order backward scheme. Consequently, the new position of the particle is given by:

$$\mathbf{x}_{\mathrm{p}}^{n+1} = \mathbf{x}_{\mathrm{p}}^n + \Delta t\left(\mathbf{u}^n + \mathbf{a}^n\frac{\tau_0}{\Phi^n}\right) + \frac{\tau_0}{\Phi^n}\left(1 - e^{-\frac{\Delta t}{\tau_p}\Phi^n}\right)\left(\mathbf{v}_p^n - \mathbf{u}^n - \mathbf{a}^n\frac{\tau_0}{\Phi^n}\right) \tag{3.18}$$

The velocity field $\mathbf{u}$ through which the bubble will move, is the potential flow solution around a cylinder. Since this velocity field is steady, it is at any instant in time given by $\mathbf{u} = [u_x, u_y]$ as a function of the particle position $\mathbf{x}_p = [x, y]$ and reads as:

$$u_x = U_0\left(R^2\frac{\left(y^2 - x^2\right)}{\left(x^2 + y^2\right)^2} + 1\right) \tag{3.19}$$

$$u_y = -U_0R^2\frac{2xy}{\left(x^2 + y^2\right)^2} \tag{3.20}$$

where U_0 is the freestream velocity and R is the radius of the cylinder. The radius R is chosen to be 20 mm, that is identical to the experimental campaign that will be discussed in chapter 6.

3.2.3 Simulation results

Simplified equation of motion: validation

The first simulations of the particle motion are performed with a simplified equation of motion, only accounting for the Stokes drag term and for the fluid-stress force. Furthermore, it is assumed that the fluid acceleration $D\mathbf{u}/Dt$ is replaced by the particle acceleration $d\mathbf{v}_p/dt$. Then the equation of motion reads as:

$$\frac{4}{3}\pi a^3\rho_p\frac{d\mathbf{v}_p}{dt} = 6\pi a\mu_f\left(\mathbf{u} - \mathbf{v}_p\right) + \frac{4}{3}\pi a^3\rho_f\frac{d\mathbf{v}_p}{dt} \tag{3.21}$$

The latter equation is the same as the one derived in subsection 3.2.1 and therefore it is known that the relaxation time expression of Equation 3.11 is valid. This allows to assess the

accuracy of the numerical simulations. The relative error ϵ between the theoretical solution of the relaxation time τ_p (Equation 3.11-left with Φ=1) and the ratio of the slip velocity over the particle acceleration, calculated by the numerical simulation, is then given by:

$$\epsilon = \max \left| \frac{\tau_p - \left(\frac{\mathbf{u}-\mathbf{v}_p}{\mathbf{v}_p} \right)_{\text{sim}}}{\tau_p} \right| \tag{3.22}$$

where the subscript *sim* stands for the simulation results. A particle is introduced 10 cylinder diameters upstream of the stagnation point of the cylinder. The particle motion along the stagnation line ahead the cylinder is simulated; any motion in the Y-direction is disabled. Consider a particle with a diameter d_p=400 μm and a specific density $\bar{\rho}$=1.02 at a freestream velocity of U_0=30 m/s. The Stokes relaxation time τ_p then equals 12.1 μs. Figure 3.7-left shows the ratio of the slip velocity over the particle acceleration of the simulation. It confirms that this ratio equals the theoretical expression of the relaxation time τ_p, as they lie exactly on top of each other. As such it validates the implementation and correct working of the numerical trajectory simulator. Under the mentioned assumptions, the relaxation time is constant along the stagnation line. From Figure 3.7-right, it becomes clear that the relative error and thus the accuracy of the simulation can be improved by decreasing the time step Δt of the simulation. The remaining simulation will all be performed with a time step Δt = 1e-08, to have accurate results, while the simulations do not become too computational expensive.

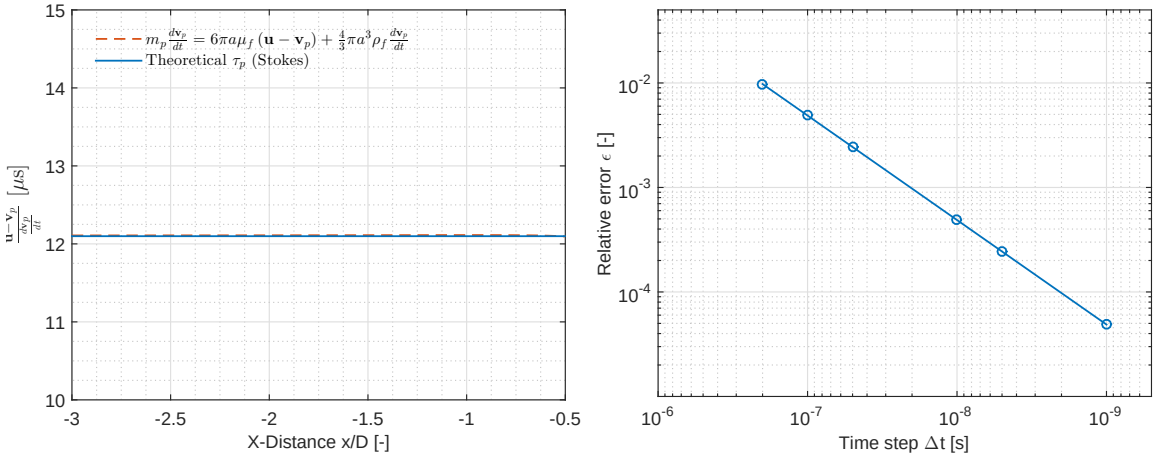

Figure 3.7: Simplified equation of motion of a HFSB (d_p=400 μm and $\bar{\rho}$=1.02). Left: Ratio slip velocity over particle acceleration on the stagnation streamline ahead of the cylinder. Right: Influence of the time step Δt on the accuracy.

Simplified equation of motion: influence of assumption $\frac{\mathbf{D\bar{u}}}{\mathbf{Dt}} = \frac{\mathbf{d\bar{v}_p}}{\mathbf{dt}}$

This section will investigate whether the assumption that both the fluid and particle acceleration are equal and can be interchanged, is valid. Therefore, the simplified equation of motion

of the previous section is reconsidered in its original form, that is:

$$\frac{4}{3}\pi a^3 \rho_p \frac{d\mathbf{v}_p}{dt} = 6\pi a \mu_f \left(\mathbf{u} - \mathbf{v}_p\right) + \frac{4}{3}\pi a^3 \rho_f \frac{D\mathbf{u}}{Dt} \tag{3.23}$$

where the right-hand side again consists of the Stokes drag and the fluid-stress force. The simulations based on the latter equation are compared to the same equation, however, where the the particle acceleration is submitted for the fluid acceleration on the right-hand side. This reads as:

$$\frac{4}{3}\pi a^3 \rho_p \frac{d\mathbf{v}_p}{dt} = 6\pi a \mu_f \left(\mathbf{u} - \mathbf{v}_p\right) + \frac{4}{3}\pi a^3 \rho_f \frac{d\mathbf{v}_p}{dt} \tag{3.24}$$

Two particles will be simulated using these equations of motion. The first is a fog droplet (diameter d_p=1 μm and specific density $\bar{\rho}$=816.33) and the second is a helium-filled soap bubble that is slightly heavier-than air (diameter d_p=400 μm and specific density $\bar{\rho}$=1.02). The quantity that for both particles will be compared is the ratio of the slip velocity over the particle acceleration, since this is supposed to equal the relaxation time (according to Scarano et al. (2015); see subsection 3.2.1). Figure 3.8-left shows the ratio of the slip velocity over the particle acceleration for the fog droplets.

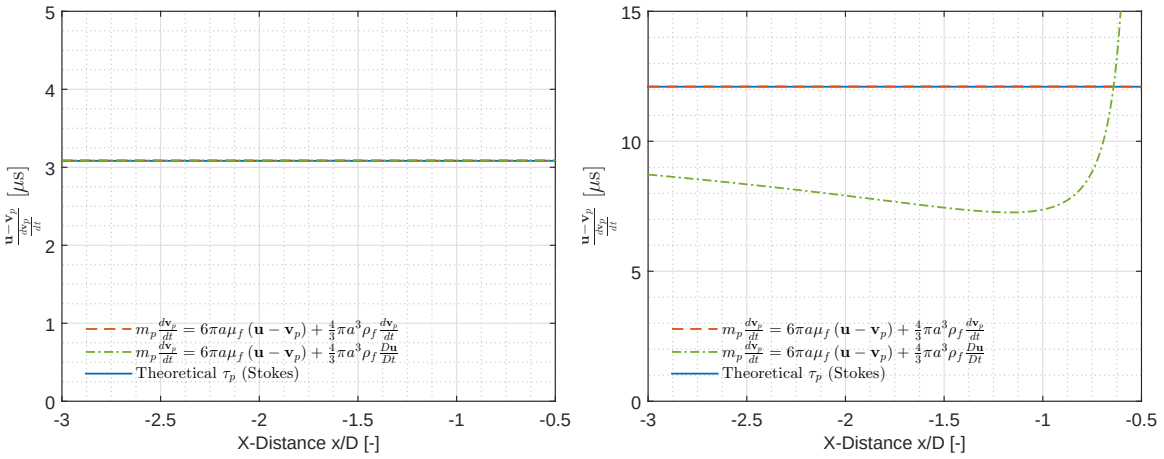

Figure 3.8: Simplified equation of motion. *Left:* fog droplet (d_p=1 μm and $\bar{\rho}$=816.33). *Right:* HFSB (d_p=400 μm and $\bar{\rho}$=1.02).

It can be seen that all the three lines lie exactly on top of each other. The assumption that the particle acceleration $d\mathbf{v}_p/dt$ and the fluid acceleration $D\mathbf{u}/Dt$ can be interchanged is valid and therefore does not affect the slip velocity over particle acceleration ratio. The latter ratio is then equal to the Stokes relaxation time τ_p. This is, however, not true for helium-filled soap bubbles. Figure 3.8 shows the same ratio for a particle with diameter d_p=400 μm and specific density $\bar{\rho}$=1.02. When the particle acceleration is substituted in the fluid-stress force term, the ratio slip velocity over particle acceleration equals the theoretical solution of the relaxation time τ_p. This is as expected and is in accordance with Figure 3.7-left. However, when the fluid acceleration term in the fluid-stress force is left untouched, the ratio slip velocity over particle acceleration is on average 33 % lower than the theoretical relaxation time τ_p and is no

longer constant along the stagnation streamline. Simulations for particles with a diameters of 100 μm and 900 μm show similar results. Therefore, the assumption of interchanging the particle and fluid acceleration is not valid for HFSBs with diameters in the range of 100-900 μm.

Simplified equation of motion: influence of drag correction factor

The effect of the drag correction factor on the relaxation time of a particle released in stagnant air is already discussed in subsection 3.1.5. Nevertheless, the effect of this correction term on the ratio slip velocity over particle acceleration for a particle moving through a non-stagnant velocity field is studied in this section. This is done by studying the same equations of motion as in the previous section, although this time including the drag correction term $\Phi(Re)$ in the quasi-steady drag force term:

$$\frac{4}{3}\pi a^3 \rho_p \frac{d\mathbf{v}_p}{dt} = 6\pi a \mu_f (\mathbf{u} - \mathbf{v}_p) \Phi(Re) + \frac{4}{3}\pi a^3 \rho_f \frac{D\mathbf{u}}{Dt} \tag{3.25}$$

The simulations based on Equation 3.25 are again compared to the same equation of motion with the particle acceleration is submitted for the fluid acceleration on the right-hand side. This reads as:

$$\frac{4}{3}\pi a^3 \rho_p \frac{d\mathbf{v}_p}{dt} = 6\pi a \mu_f (\mathbf{u} - \mathbf{v}_p) \Phi(Re) + \frac{4}{3}\pi a^3 \rho_f \frac{d\mathbf{v}_p}{dt} \tag{3.26}$$

For both the equations the results are plotted in Figure 3.9, with firstly the drag correction term activated and secondly the term forced to unity to retrieve the Stokes drag. Comparing the effect of the drag at finite Reynolds for Equation 3.26, the following can be noted: the effect of the correction far is small far from the cylinder, since the deceleration there and thus the slip velocity and particle Reynolds number is small. Closer the cylinder the deceleration is high, yielding a higher slip velocity and particle Reynolds number (maximum Re_p of around 10) and thus higher drag correction term influence. The detected ratio of slip velocity over the particle acceleration is maximum 25 % lower than the Stokes relaxation time. For Equation 3.25 the effect is less pronounced. The maximum difference between the ratios is less than 1 μs or less than approximately 8 % with respect to the Stokes relaxation time.

This analysis is not extended to fog droplets, since the maximum detected particle Reynolds number for fog droplets based on Equation 3.24 in the previous section was found to be 0.0035, which is well within the Stokes assumption.

Full equation of motion: influence of added-mass force

The final simulations that are performed, are those including the added-mass force term in the equation of motion. From the previous sections, it became clear that the difference between the particle accelerations and fluid acceleration and that the drag correction term cannot be neglected for tracer particles with the size as the HFSBs. They both affect significantly the ratio of slip velocity over particle acceleration. Including the added-mass force, the equation of motions reads as:

$$\frac{4}{3}\pi a^3 \rho_p \frac{d\mathbf{v}_p}{dt} = 6\pi a \mu_f (\mathbf{u} - \mathbf{v}_p) \Phi(Re_p) + \frac{4}{3}\pi a^3 \rho_f \frac{D\mathbf{u}}{Dt} + \frac{2}{3}\pi a^3 \rho_f \left(\frac{D\mathbf{u}}{Dt} - \frac{d\mathbf{v}_p}{dt} \right) \tag{3.27}$$

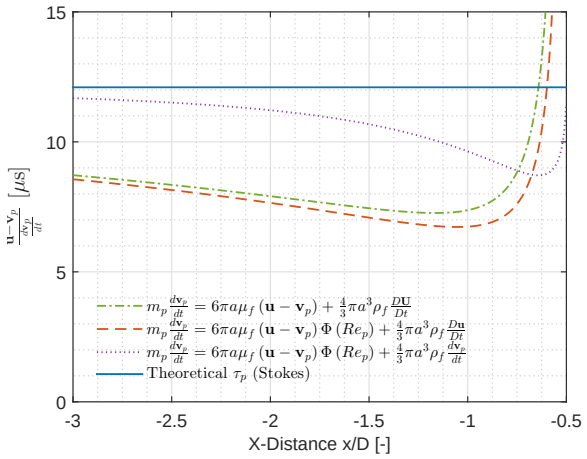

Figure 3.9: Influence of the drag correction factor on the ratio slip velocity over particle acceleration for HFSBs (d_p=400 μm and $\bar{\rho}$=1.02).

The difference between the above equation with and without the added-mass force term is illustrated in Figure 3.10-left.

The added mass force lowers the ratio of slip velocity over particle acceleration with approximately 1 μs. This is in fact a bit surprising, since the magnitude added-mass force is more than two orders of magnitude smaller than the fluid-stress force and thus seems negligible. Figure 3.10-right shows that the fluid-stress or pressure force is the dominant force in the equation of motion for a nearly neutrally buoyant HFSBs. The drag force is approximately two orders of magnitude smaller than the fluid-stress force. Since it is known from the previous sections that the simulations are very sensitive for changes in accelerations, the influence of the added-mass force on the slip velocity is investigated in Figure 3.10-bottom. It can be seen that the changes in the ratio slip velocity over particle acceleration are rather caused by changes in the slip velocity than by changes in the acceleration terms. The same variations as mentioned in Figure 3.10-left can be observed in Figure 3.10-bottom.

A similar analysis is made for an air-filled soap bubble. That is, when the bubble has a specific density $\bar{\rho}$ of approximately 1.8, keeping the diameter constant to 400 μm. The results are plotted in Figure 3.11. For air-filled soap bubbles, the fluid-stress force and the quasi-steady drag force are about the same order of magnitude, with the added-mass force being approximately one order of magnitude smaller than the former forces. Concerning the ratio of slip velocity over particle acceleration, the deviation from the Stokes drag is more pronounced. The simulated ratio is on average 50 % lower. The fluid and particle accelerations cannot be interchanged. The effect of the added-mass force is noticeable, but is less than 10 % with respect to the simulations without the added-mass force (green curve in Figure 3.11).

Discussion of the results

The differences between the different equations of motions are of huge importance for the remainder of this work. Based on the experimental measurements, discussed in chapter 6,

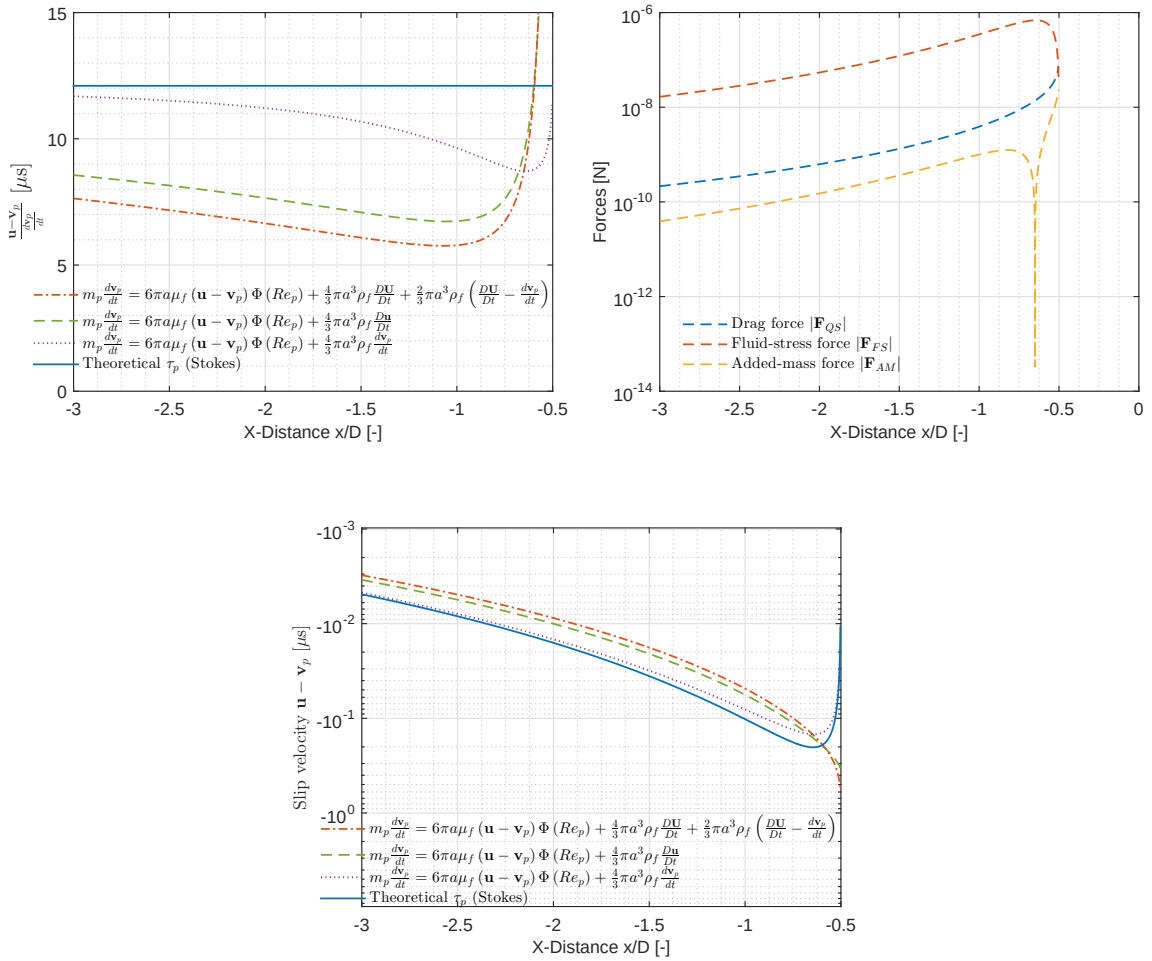

Figure 3.10: Full equation of motion of a HFSB (d_p=400 μm and $\bar{\rho}$=1.02). *Left:* ratio slip velocity over particle acceleration. *Right:* Forces.

an attempt to reconstruct of the density of the HFSBs and AFSBs based on the ratio of slip velocity over particle acceleration will be conducted. Recalling Equation 3.11 as:

$$\tau_p = \frac{d_p^2}{18}\frac{\rho_p - \rho_f}{\mu_f}\frac{1}{\Phi\left(Re_p\right)} = \frac{\mathbf{u}-\mathbf{v}_p}{\frac{d\mathbf{v}_p}{dt}} \tag{3.28}$$

the particle density can be reconstructed as:

$$\rho_p = \rho_f + \frac{18\left(\frac{\mathbf{u}-\mathbf{v}_p}{\frac{d\mathbf{v}_p}{dt}}\right)\mu_f\Phi\left(Re_p\right)}{d_p^2} \tag{3.29}$$

However, this methodology will only work correctly when the ratio of slip velocity over particle acceleration is determined by the equation of motion given in Equation 3.26. The real particle motion, that experimentally is measured in chapter 6 is best approximated by the equation

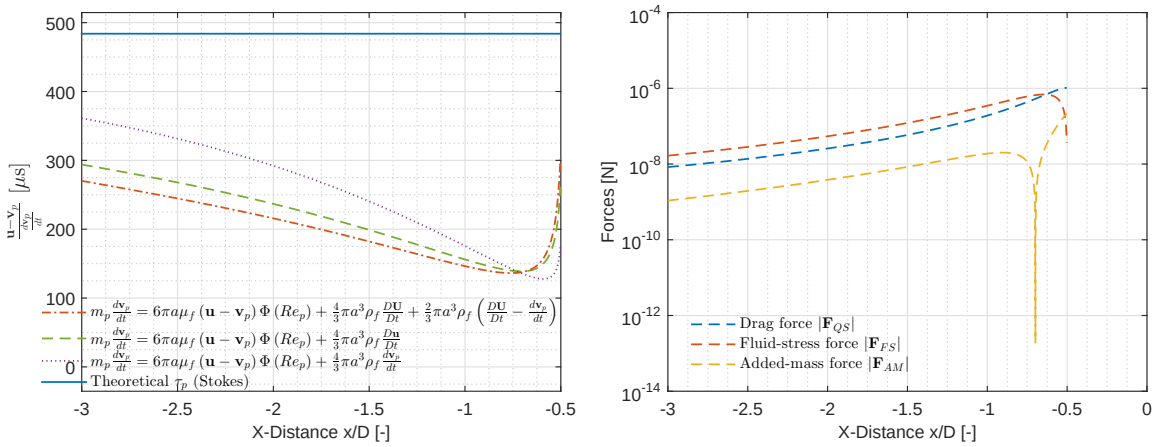

Figure 3.11: Full equation of motion for an AFSB ($\bar{\rho}$=1.80 and d_p = 400 μm). *Left:* ratio slip velocity over particle acceleration. *Right:* Forces.

of motion with all forces included (Equation 3.27). Any deviation of the ratio slip velocity over particle acceleration from the ratio given by the simulations with Equation 3.26 will propagate in the particle density calculation.

Chapter 4

Experimental methodology

This chapter discusses the experimental techniques and the experimental methodology that are used in the experiments to characterise the aerodynamic behaviour of the helium-filled soap bubbles. It deals as well with some statistical operators and data reduction techniques at the end of the chapter.

4.1 Experimental techniques

Two different velocity evaluation techniques are used: particle tracking velocimetry (PTV) and particle image velocimetry (PIV). In order to explain when each technique is to be used, it is useful to define the image density N_I. The image density N_I is a parameter expressing the mean number of particles that are present in a single interrogation window. It is defined as:

$$N_I = C\Delta Z_0 \frac{A_I}{M_0^2} \tag{4.1}$$

where C represents the mean number of particles per unit volume, ΔZ_0 is the laser sheet thickness, M_0 the magnification factor and A_I is the interrogation area in the image plane. When the image density is low, that is when $N_I \ll 1$ (Figure 4.1-left), individual particle image pairs can be recognised by visual inspection of the recordings and particle tracking velocimetry (PTV) is the preferred option to evaluate the velocity of the particles. When the image density is high, when $N_I \gg 1$ (Figure 4.1-right), it is still possible to recognize individual particles by visual inspection, however it is no longer possible to identify image pairs. Then, particle image velocimetry (PIV) is the preferred option to evaluate the particles' velocity. When using helium-filled soap bubbles as flow tracers, the images have a very low image density and PTV is used. When the flow is seeded with micron-sized fog droplets, the image density is high and PIV is applied to determine the velocity field. The next section elaborates on both the techniques.

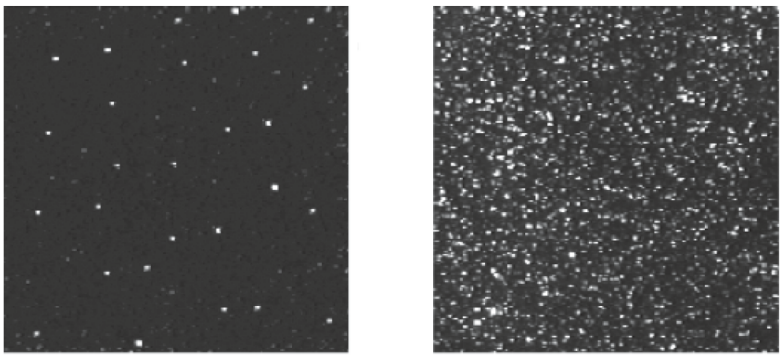

Figure 4.1: Example of an image with a low image density: $N_I \ll 1$ (left) and with a high image density: $N_I \gg 1$ (right). (Reproduced from Raffel et al. (2007)).

4.1.1 Particle Tracking Velocimetry (PTV)

Particle tracking velocimetry is an experimental technique that tracks the position of a particle over time and subsequently derives the particle velocity and acceleration. The main working principle was already shortly discussed in section 2.1, but a more detailed explanation of the PTV algorithm, based on the work of Malik et al. (1993) is given below.

Particles are identified in the images as local intensity maxima in a circular area with a radius of n pixels, where the value n is user-defined. A single threshold value is used to distinguish particle images from noise. Pixels with an intensity value below this threshold are considered as noise and are discarded. Next, the intensity maxima are coupled into bubbles by glare point matching. Since the orientation and the distance between two glare points can be estimated from the optical settings of the experimental apparatus, it suffice to define a search circle with a radius of n pixels around each particle and search within this area for another intensity maximum. Two glare points will be coupled into a single bubble if the glare points are the only intensity maxima found in both the search areas. Since the glare points are symmetric around the centre of the bubble, the exact bubble location (i.e. the centre) can be determined as the average of the two glare points' coordinates. Subpixel accuracy is obtained by fitting a Gaussian distribution through the glare points. The positions of bubbles in multiple consecutive images are used to identify bubble tracks. A velocity predictor is used to estimate the position of a bubble at time t_{i+1}, when its position is known at t_i. This predictor is inserted as a vector field that is known a priori, but in case no vector field is available it can be replaced by a search box. When the position of a bubble is known for m consecutive recordings, a polynomial in time with order n is fitted through each position dimension. Mathematically this reads as

$$\mathbf{x}_p = \sum_{i=0}^{n} \mathbf{a}_i t^i \tag{4.2}$$

where the dimension of the vectors $\mathbf{x}_p$ and $\mathbf{a}$ is two for a two-dimensional and three for a three-dimensional analysis of the particle motion. The bubble position, velocity and acceleration at t_i are evaluated in the middle of the series of recordings, that is when t_i is data point

number $(m+1)/2$ in the track. Therefore the number of consecutive recordings fitted in one polynomial should be preferably uneven. The first time-derivative of the polynomial yields the velocity and the second time-derivative the Lagrangian acceleration at the particle locations.

$$\mathbf{v}_p = \dot{\mathbf{x}}_p = \sum_{i=1}^{n} i\ \mathbf{a}_i t^{i-1} \tag{4.3}$$

$$\frac{d\mathbf{v}_p}{dt} = \ddot{\mathbf{x}}_p = \sum_{i=2}^{n} i\,(i-1)\,\mathbf{a}_i t^{i-2} \tag{4.4}$$

This working principle is illustrated in Figure 4.2. A one-dimensional deceleration of a single particle is simulated with synthetic data, recorded over a series of 15 points in time. A third-order polynomial (blue line) is fitted through the measured particle positions (red cross marks in Figure 4.2-left). The evaluation of velocity and acceleration will be at the location of the eight data point (the middle of the 15 data points). The first-order derivative (i.e. a second-order polynomial) equals the particle velocity (Figure 4.2-middle) and the second-order derivative (i.e. a first-order polynomial or straight line) represents the acceleration (Figure 4.2-right).

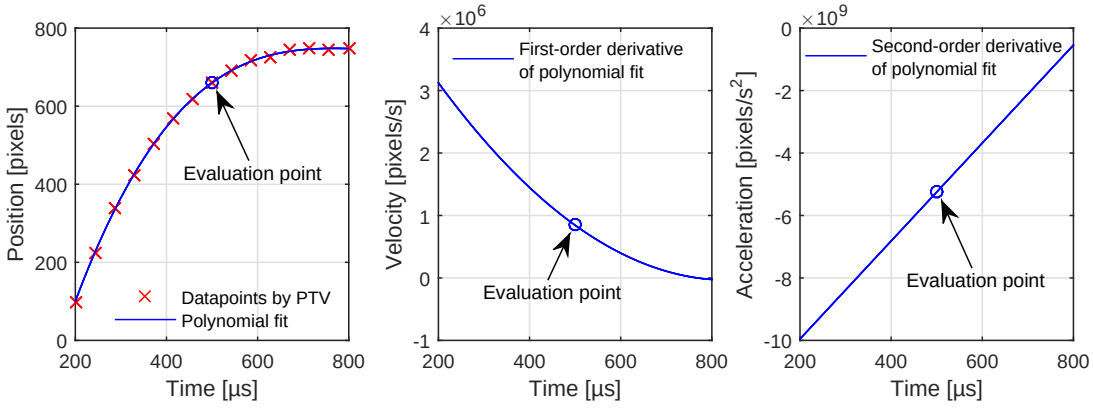

Figure 4.2: PTV track with a third-order polynomial fit through 15 datapoints (synthetic data of a one-dimensional deceleration). *Left*: Position (third-order polynomial). *Middle*: Velocity (first-order derivative). *Right*: Acceleration (second-order derivative).

4.1.2 Particle Image Velocimetry (PIV)

The working principle of particle image velocimetry was already shortly mentioned in section 2.1. This section will focus on the evaluation of the velocity field based on two consecutive images.

Each image is split up into different interrogation windows. An interrogation window is a smaller cell (typical size ranging from 16×16 to 128×128 pixels) that contains a statistically sufficient number of tracer particles. The velocity in each interrogation window is evaluated using a statistical cross-correlation analysis between two consecutive recordings of that interrogation window, resulting in one local velocity vector per interrogation window. It returns a

two-dimensional cross-correlation map with a strong peak of which the position with respect to the origin indicates the average particle displacement in pixels. Consider the interrogation windows $I(x, y, t)$ at time t and $I'(x, y, t)$ at time $t + \Delta t$. The cross-correlation algorithm is then given by

$$\phi(m, n) = \frac{\sum_{j=1}^{J} \sum_{k=1}^{K} I(j, k) \cdot I'(j + m, k + n)}{\sqrt{\sum_{j=1}^{J} \sum_{k=1}^{K} I^2(j, k) \cdot \sum_{j=1}^{J} \sum_{k=1}^{K} I'^2(j, k)}} \tag{4.5}$$

where J and K are the dimensions of the interrogation window. The accuracy of the position of the peak can be improved by fitting a Gaussian distribution through the peak. As such the exact peak location and thus the average particle displacement (expressed in pixels) can be estimated with sub-pixel accuracy. The velocity can be obtained by multiplying the average particle displacement by the pixel pitch and through division by optical magnification factor M_0 and time separation Δt between the two images. The working principle of the velocity evaluation by cross-correlation is illustrated in Figure 4.3.

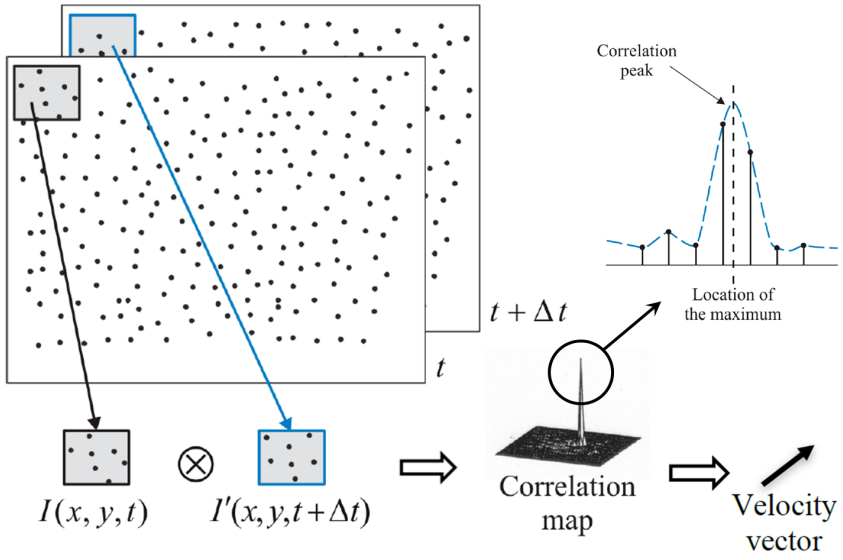

Figure 4.3: Velocity vector extraction using cross-correlation from PIV images (reproduced from Scarano (2013b)).

4.2 Cylinder experiment

A planar PIV experiment with a cylinder is conducted and aims to quantify the tracing fidelity and other physical properties of the HFSBs, such as bubble diameter, bubble density and soap film thickness. The methodology of the experiment is based on the one of Scarano et al. (2015). However, by simultaneous measurements of the bubbles' velocities and diameters, it is possible to not only derive information on the tracing fidelity of bubbles with different

densities and diameters, but also to retrieve the density and soap film thickness of the HFSBs. This approach is extended from measurements of the mean properties of all bubbles per measurement (as done by Scarano et al. (2015)) to an analysis of each bubble individually. This will give information on the dispersion of the properties of the HFSBs. A cylinder is chosen as test model, since its stagnation region in front features an irrotational, steady, two-dimensional and incompressible flow. This flow field can be easily modelled by theoretical models and has a high repeatability.

4.2.1 Bubble velocity and acceleration

The velocity and acceleration measurements of the HFSBs are carried out using particle tracking velocimetry (PTV). The particle tracking algorithm is based on that of Malik et al. (1993). A brief summary of the PTV technique was given in subsection 4.1.1. The acceleration computed by the PTV algorithm is the Lagrangian acceleration of the particles and is given by:

$$\frac{d\mathbf{v}_p}{dt} = \frac{\partial \mathbf{v}_p}{\partial t} + \mathbf{v}_p \cdot \nabla \mathbf{v}_p \tag{4.6}$$

where $\partial \mathbf{v}_p / \partial t$ is zero since the flow field in the stagnation region of a cylinder is assumed to be steady. Thus, the particle acceleration equals the convective term only. In this experiment a comparison of the velocity and acceleration profiles along the stagnation line of the cylinder is performed. Along the stagnation streamline, the fluid parcels undergo a one-dimensional deceleration. For the HFSBs, the mean velocity and acceleration of all the bubbles are computed by averaging the instantaneous values within a box of 24 pixels height (symmetric around the stagnation streamline) and 15 pixels streamwise length.

4.2.2 Reference velocity and acceleration

A reference velocity field is obtained by particle image velocimetry with fog droplets as tracer particles, as explained in subsection 4.1.2. The reference acceleration field is obtained by applying a second-order central finite difference scheme to the velocity vector field. Since the velocity field is assumed to be steady, the Lagrangian acceleration is calculated using the convective term only as:

$$\frac{D\mathbf{u}_i}{Dt} = \mathbf{u}_i \cdot \nabla \mathbf{u}_i = \mathbf{u}_i \cdot \left(\frac{\mathbf{u}_{i+1} - \mathbf{u}_{i-1}}{\mathbf{x}_{i+1} - \mathbf{x}_{i-1}} \right) \tag{4.7}$$

The resulting velocity and acceleration vector fields are interpolated to the measured position of each recorded bubble. The mean velocity and acceleration of all the bubbles along the stagnation line of the cylinder are computed identical as the HFSBs mean velocity and acceleration. Knowing the instantaneous bubble velocity (by PTV) and the reference velocity at the position of the bubble (by PIV), it is possible to calculate the relative velocity of the bubble with respect to the surrounding fluid, called the slip velocity $\mathbf{u}_s$ of the bubble as:

$$\mathbf{u}_s = \mathbf{u} - \mathbf{v}_p \tag{4.8}$$

4.2.3 Relaxation time

An expression for the particle relaxation time τ_p based the equation of motion of Mei (1996) (see section 2.4) was derived in subsection 3.2.1. In the derivation, it was assumed that the gravity force, the history force and the transverse lift force could be neglected. Moreover, it was assumed that the difference in particle and fluid acceleration is small and thus the particle acceleration could be substituted for the fluid acceleration. It was found that the definition of the relaxation time then equals:

$$\tau_p = \frac{d_p^2}{18}\frac{\rho_p - \rho_f}{\mu_f}\frac{1}{\Phi\left(Re_p\right)} = \frac{\mathbf{u} - \mathbf{v}_p}{\frac{d\mathbf{v}_p}{dt}} \tag{4.9}$$

Since both the slip velocity $\mathbf{u} - \mathbf{v}_p$ and particle acceleration $\frac{d\mathbf{v}_p}{dt}$ are measured in the experiment, the relaxation time for each particle at each time instant can be determined as the ratio of slip velocity over particle acceleration (see Equation 4.9).

4.2.4 Bubble diameter

At a high magnification, two glare spots per bubble can be distinguished. It was found by van de Hulst and Wang (1991) that a unique relation exists between the glare spots distance d_G, the angle the illumination axis makes with the imaging axis and the refractive indices of the different fluids the light rays pass through. Following the assumption that a HFSB from an optical point of view can be approximated by a sphere with an infinitesimal transparent coating filled with air (see subsection 2.5.4), the glare spots distance d_G becomes a function of the bubble diameter d_p only and reads as:

$$d_G = d_p \cos\left(\frac{\pi - \theta}{2}\right) \tag{4.10}$$

where θ is the angle between the axis of the illumination and imaging system. In the present experiment (planar PIV), this angle is 90 degrees and the above equation reduces then to:

$$d_p = \sqrt{2} d_G \tag{4.11}$$

The exact positions of the light rays and the glare points distance is illustrated in Figure 4.4-left for θ=90 degrees. Sub-pixel accuracy is obtained by fitting a Gaussian distribution through the glare points. The Gaussian fit is based on the work of Westerweel (1997) and reads as:

$$\hat{\epsilon}_G = \frac{\ln I_{-1} - \ln I_{+1}}{2\ln I_{-1} - 4\ln I_0 + 2\ln I_{+1}} \tag{4.12}$$

where I_{-1} and I_{+1} are the intensities of the pixels at both sides of the pixel with maximum intensity I_0. The equation returns the location of the top of the Gaussian $\hat{\epsilon}_G$ as the shift (in pixels) from the center of the pixel with the maximum intensity. Figure 4.4-right is a recording of the two glare points and shows the locations of maximum intensities with sub-pixel accuracy. Each bubble will be recorded multiple times due to the time-resolved

measurements. This allows to determine a reliable mean bubble diameter based on all the recordings of a single HFSB and to quantify the diameter measurement uncertainty, since it is assumed that the bubble diameter does not change over small time intervals. The measurement uncertainty ϵ_m can then be determined as:

$$\epsilon_m = \frac{\sigma_{d_p}}{\sqrt{N}} \tag{4.13}$$

with σ_{d_p} being the standard deviation of the diameter measurements and N the number of samples.

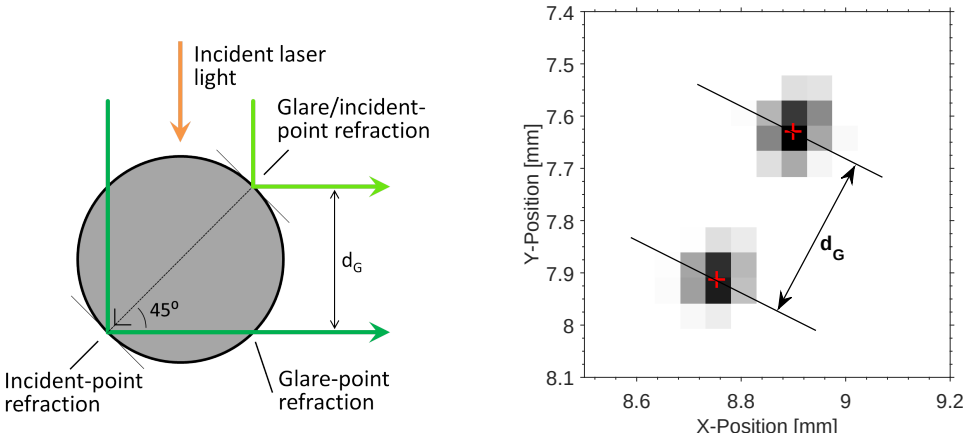

Figure 4.4: *Left*: Schematic overview of glare points distance for a HFSB in a planar PIV set-up. *Right*: Glare points as measured with planar PIV, red crosses indicate intensity maxima (Gaussian fit).

4.2.5 Bubble density

The bubble density can be derived from the definition of the relaxation time, which was obtained in subsection 4.2.3. Since the diameter, slip velocity and relaxation time are measured for each bubble at each time instant, the corresponding particle density can be extracted from Equation 4.9. Rewriting this equation gives:

$$\rho_p = \frac{18\mu_f \tau_p \Phi\left(Re_p\right)}{d_p^2} + \rho_f \tag{4.14}$$

In the latter, the correction factor $\Phi\left(Re_p\right)$ is given by the expression of Schiller and Naumann (1933) that reads as:

$$\Phi\left(Re_p\right) = 1 + 0.15 Re_p^{0.687} \tag{4.15}$$

but can be replaced by other correction factors available in literature. The density of the fluid (air) can be derived from the ideal gas law, since both the atmospheric pressure and

temperature were measured during the experiments. It is assumed that the density of the bubble stays constant during the time-resolved measurements. This assumption seems justified, since the time interval between the recordings (in the order of microseconds) is too small to experience any significant loss in helium or soap.

4.2.6 Bubble soap film thickness

The bubble film thickness can be estimated from the fact that the total bubble mass equals the sum of the mass of the soap film and the mass of the helium. Assuming that the HFSB has a constant film thickness t and can be modelled as a thin-walled sphere with radius a, Equation 4.16 holds and can be solved for film thickness t. A more in-depth analysis of this model was given in chapter 3.

$$\frac{4}{3}\pi a^3 \rho_\mathrm{p} = \frac{4}{3}\pi \left(a-t\right)^3 \rho_\mathrm{He} + \frac{4}{3}\pi \left(a^3 - \left(a-t\right)^3\right) \rho_\mathrm{bfs} \tag{4.16}$$

$$t = a\left(1 - \sqrt[3]{\frac{\rho_\mathrm{p} - \rho_\mathrm{bfs}}{\rho_\mathrm{He} - \rho_\mathrm{bfs}}}\right) \tag{4.17}$$

The particle diameter and density ρ_p are both measured (subsection 4.2.4 and 4.2.5 respectively). The density of helium can be approximated with the ideal gas law:

$$\rho_\mathrm{He} = \frac{p_\infty}{RT} \tag{4.18}$$

where p_∞ is the static pressure around the bubble, T the temperature of the surrounding fluid and R the gas constant of helium. The influence of the surface tension of the soap on the density of helium was proven to be negligible in chapter 3. The density of the BFS mixture ρ_bfs is measured to be 1,130 kg/m^3. It is assumed that the density of the soap is insensitive for changes in temperature and/or pressure.

4.3 Boundary layer experiment

The second experiment aims at testing the behavior of the helium-filled soap bubbles in a region of laminar shear. It will be investigated whether the transverse lift force due to the velocity difference on both sides of the HFSB is strong enough to influence the bubble trajectory. This will be examined by means of a laminar boundary layer on top of a flat plate. The literature survey in subsection 2.4.1 indicates that this lift force is dependent on the bubble diameter, the velocity gradient, the slip velocity of the particle and the viscosity of the surrounding fluid. The bubble diameter can be adapted by changing the mass flow rate of the second air flow in the nozzle. The velocity gradient in a laminar boundary layer is a function of the height normal to the flat plate surface, the position downstream on the flat plate and the freestream velocity. A slip velocity can be created by producing non-buoyant HFSBs.

The research will primarily focus on a qualitative assessment. If the transverse lift force exhibits a significant change in the bubbles' trajectories, it can be expected that the region

close to the flat plate (the region with the strongest shear) will be free of particles. By assessing the height normal to the flat plate surface of the empty region, the effect of the shear on the particles can be assessed in the qualitative way. A second, quantitative way of determining the effect of the shear, is by measuring the velocity component normal to the flat plate surface. Since this velocity component is zero in a boundary layer, it means that if any velocity component normal the plate is detected, this is caused by the transverse lift force minus the buoyancy-gravity force in the shear region.

The bubble velocity (measured by PTV), the reference velocity field (measured by PIV with fog droplets) and the bubble diameter will be determined in an identical way as explained in section 4.2.

4.4 Data reduction techniques

This section provides some statistical features that are used in this project to reduce the amount of data and to gain information on the properties of individual data points as well as full data sets. These techniques will be formulated for a data set with discrete data points x_i and sample size N.

The mean μ is the well known ratio of the sum of all the data points over the the number of data points.

$$\mu = \frac{1}{N}\sum_{i=1}^{N} x_i \tag{4.19}$$

The standard deviation σ is a measure the quantify the dispersion of a data set. A low standard deviation means that all data points are close to the mean, whereas a high value indicates that all data points are spread over a wide range of values. The standard deviation has the same unit as the data points themselves.

$$\sigma = \sqrt{\frac{1}{N}\sum_{i=1}^{N} (x_i - \mu)^2} \tag{4.20}$$

The meaning of the standard deviation can be better explained with the help of a normal or Gaussian distribution. The normal distribution is a popular distribution in statistics. The probability density function $f(x|\mu,\sigma)$ of a normal distribution $\mathcal{N}(\mu,\sigma)$ is given by:

$$f(x|\mu,\sigma) = \frac{1}{\sqrt{2\pi\sigma^2}} \mathrm{e}^{-\frac{(x-\mu)^2}{2\sigma^2}} \tag{4.21}$$

The latter returns the probability of the appearance of a variable x_i in a data set that is normal distributed with mean μ and standard deviation σ or in short $\mathcal{N}(\mu,\sigma)$. In the graphical representation of a normal distribution this corresponds to the height of the probability density curve at the location of x_i. The cumulative distribution function $F(x|\mu,\sigma)$ is the probability

density function that is integrated with respect to x. It returns the probability that a random sample X will have a value less than or equal to x.

$$F\left(x|\mu,\sigma\right) = \frac{1}{2}\left[1 + \text{erf}\left(\frac{x-\mu}{\sqrt{2}\sigma}\right)\right] \tag{4.22}$$

This allows to determine the probability of appearance in terms standard deviations. The probability of appearance in the interval $\mu \pm \sigma$ equals 68.2%, in $\mu \pm 2\sigma$ it equals 95.4 % and for $\mu \pm 3\sigma$ it is 99.7%.

This is explained by an example. Figure 4.5 illustrates the probability density function $f(x|\mu,\sigma)$ (left) and the cumulative distribution function $F\left(x|\mu,\sigma\right)$ (right) of a normal distribution $\mathcal{N}\left(0,1\right)$. The probability that a sample X out of a normal distributed data set $\mathcal{N}\left(0,1\right)$ is bigger than or equal to $\mu - \sigma$ and smaller than or equal to the value $\mu + \sigma$ can be calculated by the difference of the the cumulative distribution functions $F\left(\mu + \sigma|\mu,\sigma\right)$ - $F\left(\mu - \sigma|\mu,\sigma\right)$. In a similar way, the probabilities of appearance in each interval with length σ of the probability density function plot can be calculated.

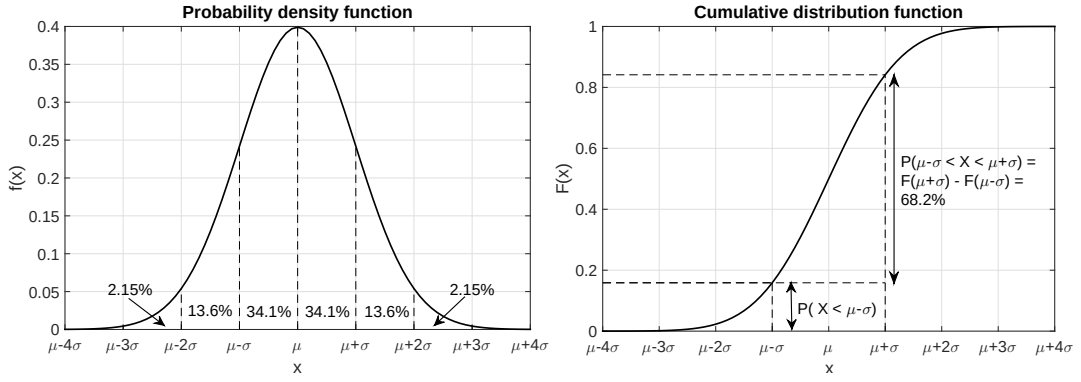

Figure 4.5: Normal distribution $\mathcal{N}\left(0,1\right)$. *Left:* Probability density function $f(x|0,1)$. *Right:* Cumulative distribution function $F(x|0,1)$.

Grubbs' test is an outlier detection algorithm. It is based on a t-distribution, that is used when estimating the mean of a normal distribution when the standard deviation is unknown and the sample size is small. The larger the sample size, the more the distribution resembles a normal distribution. The test detects the data point with the biggest deviation from the mean of the dataset per iteration. Mathematically this reads as:

$$G = \frac{\max\limits_{i=1,\ldots,N} |x_i - \mu|}{\sigma} \tag{4.23}$$

where μ and σ are respectively the mean and standard deviation from the dataset with N data points. This data point is considered as an outlier and thus removed from the data set if the following condition is met:

$$G > \frac{N-1}{\sqrt{N}}\sqrt{\frac{t^2_{\alpha/(2N),N-2}}{N-2+t^2_{\alpha/(2N),N-2}}} \tag{4.24}$$

In the latter the value $t_{\alpha/(2N),N-2}$ is the critical value of the t-distribution with significance level α. For more information on the t-distribution and its parameters, the reader is referred to Forbes et al. (2011). After every rejected data point the statistical properties (i.e. the mean, standard deviation and number of data points) are recalculated. The test is iterated until no more outliers can be detected.

Chapter 5

Experimental apparatus & set-up

During this research project one experimental campaign with two different test models was held to characterize the aerodynamic behavior of the helium-filled soap bubbles. This chapter aims to outline the experimental apparatus and set-ups of both the experiments. Also the data processing routines are shortly discussed at the end of this chapter.

5.1 Facility and models

5.1.1 Wind tunnel facility

The experiments are conducted in the W-tunnel, an open-jet open-return facility in the High Speed Laboratory (HSL) of the aerodynamics department of the faculty of Aerospace Engineering at TU Delft. The wind tunnel has a test section of 40×40 cm^2. The freestream velocity range of the wind tunnel is between 5 - 30 m/s and is measured using a pitot tube, connected to a digital pressure gauge (Mensor model 2101). The dynamic pressure is converted to flow velocity with an in-house developed Labview program.

The W-tunnel is preferred over other wind tunnels for its low turbulence level of 0.5% at 20 m/s due to the high contraction ratio of 1:9 between test section and the settling chamber and for the easy accessibility of the settling chamber to install the bubble generator. The closed test section is made out of plexiglass to have full optical access for illumination and imaging to allow particle image velocimetry (PIV).

5.1.2 Models

In the first experiment a circular cylinder with a diameter of 40 mm is tested. A 2 mm thick splitter plate with a length of 280 mm (seven cylinder diameters) is attached to the aft of the cylinder. It prevents the von Kármán vortex shedding and suppresses the resulting fluctuations of the stagnation position. The boundary layer on the cylinder is tripped to fully turbulent by applying carborundum grains on both sides at the quarter chord length to postpone flow separation. The model is painted black to damp laser light reflections. The stagnation region in front of the cylinder features an irrotational, steady, two-dimensional, incompressible flow. This flow field can easily be modelled with theoretical models and has a high repeatability.

For the second experiment a 90 cm long and 1 cm thick flat plate with a sharp leading edge is installed in the wind tunnel mid-section. The plate is inclined with -2 degrees with respect to the freestream velocity direction to prevent flow separation. A laminar boundary layer forms on the top surface of the flat plate, providing a region of steady shear, that can be modelled by the Blasius boundary layer for a horizontal flat plate and by the Falkner-Skan boundary layer for an inclined plate or wedge flow (White, 2005). A schematic overview of both the models is given in Figure 5.1.

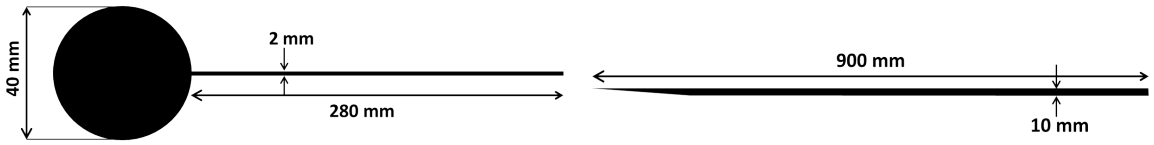

Figure 5.1: *Left*: Schematic overview of the cylinder model. *Right*: Schematic overview of flat plate model.

5.2 Cylinder experiment

5.2.1 Set-up

The laser is placed under the test section and the light beam is reflected upwards under an angle of approximately 60 degrees using a mirror. Cylindrical lenses expand the beam into a thin light sheet and illuminates the stagnation region in front of the cylinder in the middle of the test section. The laser sheet thickness is approximately 1-2 mm. The illumination system is a Quantronix Darwin-Duo Nd:YLF laser with a nominal pulse energy of 2×25 mJ at 1 kHz. It emits light at a wavelength of 532 nm (visible green light for the human eye).

The imaging system consists of one Photron Fast Cam SA1 camera (CMOS, 1,024×1,024 pixels, 12-bit, pixel pitch 20 μm). The camera is positioned with its sensor perpendicular to the cylinder axis. It is equipped with a 105 mm Nikkor objective with aperture settings of f/5.6 (for reference velocity field with fog droplets) and f/16 (for HFSBs). The lower aperture

for the HFSBs is because the excess of light made it impossible to distinguish glare points. The sensor is cropped to 704×336 pixels to allow acquisition of a higher number of images at a higher frequency. The field of view is 3.41×1.63 cm^2, yielding an optical magnification M_0 of 0.41. The set-up of this experiment is illustrated in Figure 5.2.

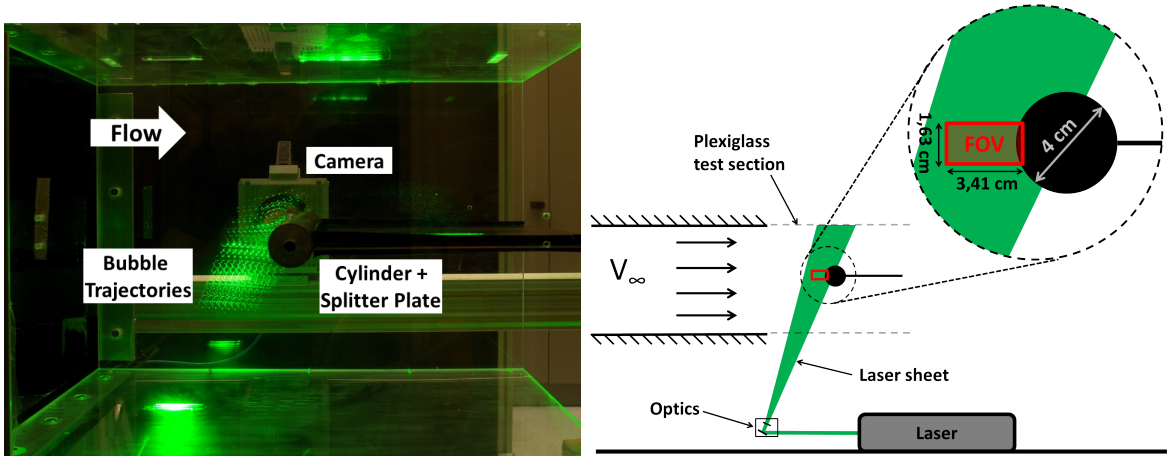

Figure 5.2: Set-up of the cylinder experiment. *Left*: Photograph. *Right*: Schematic overview.

For the HFSBs measurements at 10 m/s, 10,000 single-frame images were taken at an acquisition frequency of 10 kHz. This corresponds to a particle displacement of approximately 20 pixels. At a freestream velocity of 20 m/s, 10,000 double-frame images are acquired at an acquisition frequency of 10 kHz with a time separation of 50 μs, which is equivalent to 20,000 single frame images at 20,000 Hz. This is as well equivalent to a particle displace of approximately 20 pixels. At the highest velocity of 30 m/s, 12,000 double-frame images are acquired at an acquisition frequency of 10 kHz with a time separation of 50 μs, which is equivalent to 24,000 single frame images at 20,000 Hz and a particle displacement of approximately 30 pixels.

A bubble generator v2 from LaVision GmbH (Figure 5.3-left) is placed in the settling chamber of the wind tunnel. This nozzle design is identical to the one used by Bosbach et al. (2009), Kühn et al. (2011) and Scarano et al. (2015). The bubble generator is mounted in an aerodynamic rake (a vertical NACA0012 wing) to minimize the aerodynamic intrusiveness (Figure 5.3-right). The bubble diameter and density can be controlled by varying the supply pressure of the BFS mixture, the helium and secondary air flow in the bubble generator. For further information on the working principle of the bubble generator, the reader is referred to subsection 2.5.2 or to Bosbach et al. (2009).

The reference velocity field is obtained by planar PIV measurements with micron-sized fog droplets, generated by a SAFEX Twin Fog smoke generator (median particle diameter of 1 μm). This smoke generator was installed at the inlet of the wind tunnel and the seeding concentration was controlled manually. During the reference measurements the aerodynamic rake with nozzle was installed in the settling chamber and the helium and air supply in the bubble generator were turned on to create exactly the same flow conditions as in the HFSBs measurements. A set of 3,000 double-frame images is acquired at an acquisition frequency of

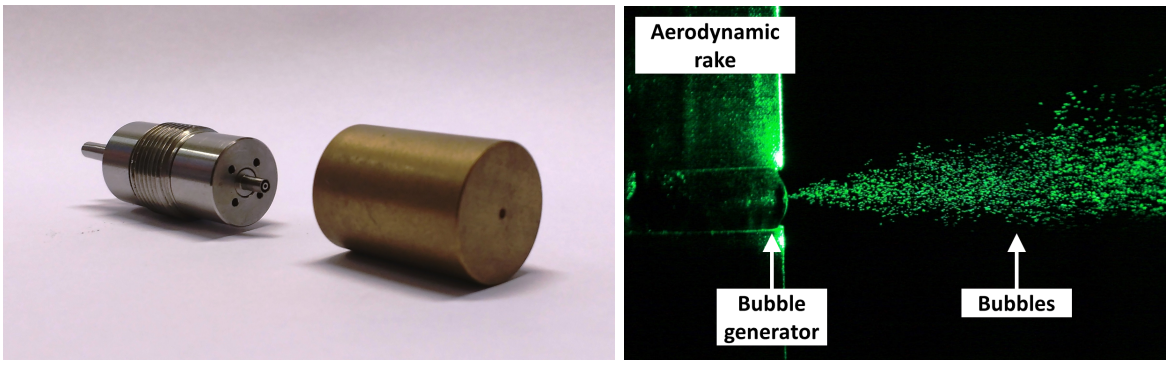

Figure 5.3: Bubble generator v2 from LaVision GmbH. *Left*: Nozzle. *Right*: Operating nozzle in aerodynamic rake installed in the settling chamber of the wind tunnel.

250 Hz with a time separation of 95, 38 and 30 μs for a freestream velocity of respectively 10, 20 and 30 m/s. This corresponds to particle displacements of approximately 20, 16 and 24 pixels respectively.

Table 5.1: Experimental parameters of experiment with cylinder.

Parameter	**Quantity**	
Seeding	Fog droplets	HFSBs
Velocity	10, 20, 30 m/s	10, 20, 30 m/s
Field of view, FOV	3.41×1.63 cm^2	3.41×1.63 cm^2
Sensor size	704×336 pixels	704×336 pixels
Magnification, M_0	0.41	0.41
Focal length, f	105 mm	105 mm
Numerical aperture, $f_\#$	5.6	16
Recording mode	Double frame	Single frame
PIV acquisition frequency	250 Hz	10, 20, 20 kHz
Pulse separation, Δt	95, 38, 30 μs	N/A
Number of images, N	3×3,000	10,000, 20,000, 24,000

5.2.2 Test matrix

The aerodynamic behaviour, as well as the other properties mentioned in section 4.2, will be analysed for bubbles with different densities and diameters at different velocities. As discussed in chapter 3, the density of the bubble can be adapted by changing the ratio $Q_{\text{helium}}/Q_{\text{bfs}}$. The bubble diameter is mainly controlled by the mass flow rate of the secondary airflow Q_{sa}, although it was found experimentally that also the volume flow rate of helium Q_{helium} has a small influence on the bubble diameter.

The HFSB test matrix (Table 5.2) is composed to have at least three different bubble densities and three different bubble diameters at each velocity. The density deviation from the neutrally buoyant condition should be more pronounced at lower velocities, since the forces acting on

the bubbles scale with the magnitude of the accelerations of the bubbles. Therefore, air-filled soap bubbles are used to study the behaviour of heaver-than-air particles. Furthermore, the range of stable production of the bubble nozzle was a major constraint during the test campaign.

The flow rates of the three fluids are regulated by the supply pressures on the FSU. The capillaries causing the main pressure drop (discussed in subsection 2.5.2) are 300 mm long with an inner diameter of 500 μm for the air supply, 350 mm long with an inner diameter of 150 μm for the BFS supply channel and 200 mm long with an inner diameter of 150 μm for the helium supply. The calibration between the volume flow rates of the BFS mixture, helium and secondary air flow was performed by LaVision GmbH for helium-filled soap bubbles. The calculation of the air flow through the helium capillary for air-filled soap bubbles is based on the helium calibration of LaVision GmbH. The volume flow rates of helium are multiplied by 1.0829 (=the ratio of μ_{He}/μ_{air}) to obtain the volume flow rates of air, through the same capillary with the same pressure difference. This calculation is based on a laminar flow through a pipe, as modelled by the Darcy-Weisbach equation.

Table 5.2: HFSB test matrix of cylinder experiment.

$\mathbf{p_{bfs}}$ [bar]	$\mathbf{p_{he/air}}$ [bar]	$\mathbf{p_{sa}}$ [bar]	$\mathbf{Q_{bfs}}$ [ml/h]	$\mathbf{Q_{He/air}}$ [l/h]	$\mathbf{Q_{sa}}$ [l/h]	Filled with:	10 [m/s]	20 [m/s]	30 [m/s]
2	2	2	4.78	4.83	115.30	Helium	✓	✓	✓
2.4	1.8	2	5.73	4.14	115.30	Helium		✓	✓
1.4	2	2	3.35	4.83	115.30	Helium		✓	✓
2	2	3	4.78	4.83	162.57	Helium		✓	✓
2	2	1.4	4.78	4.83	86.94	Helium		✓	
2	2	1.2	4.78	4.83	77.49	Helium			✓
2	2	2	4.78	5.23	115.30	Air	✓	✓	✓
2	2	3	4.78	5.23	162.57	Air	✓	✓	
2	2	1.6	4.78	5.23	96.40	Air	✓		
2	1.6	1.2	4.78	3.79	77.49	Air		✓	

5.3 Boundary layer experiment

5.3.1 Set-up

In this experiment, the laser is placed on the ground far downstream of the wind tunnel. The light beam is reflected upwards and illuminates the mid-section of the flat plate from above with an angle bigger than the -2 degrees inclination of the plate. The light sheet is again around 1-2 mm thick and the illumination system is again a Quantronix Darwin-Duo Nd:YLF laser. Two Photron Fast Cam SA1 cameras (CMOS, 1,024×1,024 pixels, 12-bit, pixel pitch 20 μm) are placed with their sensors parallel to the flow direction. The first camera is equipped with a 200 mm and the second with a 105 mm Nikkor objective. The aperture settings are f/8 (for reference velocity field with fog droplets) and f/22 (for HFSBs). The sensors of the cameras are cropped to 1024×400 pixels. Their field of view is 2.38×0.93

cm^2 and 3.68×1.44 cm^2, giving an optical magnification M_0 of 0.86 and 0.56 respectively. The first camera images the leading edge. The second camera is placed 30 cm downstream the leading edge. The higher focal length of the first lens is chosen to resolve the glare spot distance and the thin boundary layer on the leading edge with an higher spatial resolution. The same bubble generator is installed in a identical way in the wind tunnel as in the cylinder experiment. The experimental set-up is displayed in Figure 5.4.

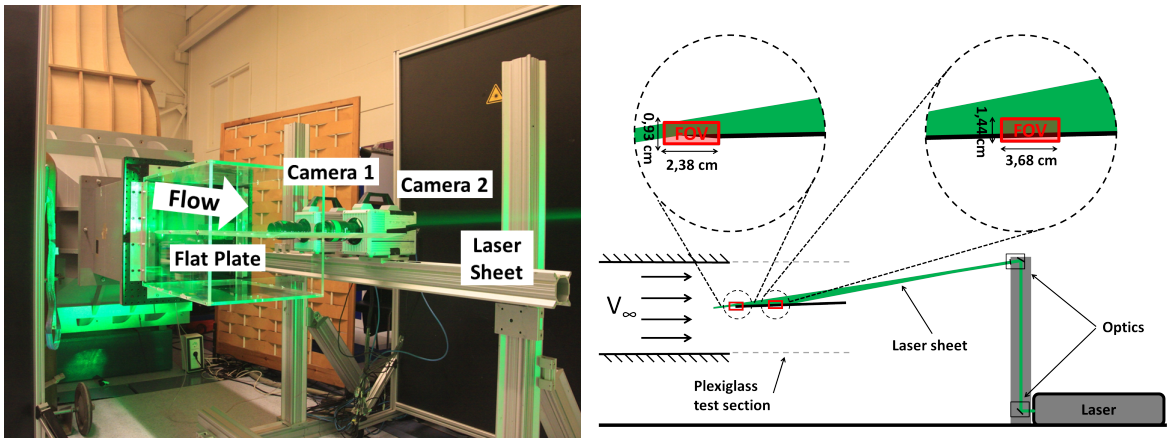

Figure 5.4: Set-up of the flat plate experiment. *Left*: Photograph. *Right*: Schematic overview.

HFSB measurements are performed at freestream velocities of 5 and 15 m/s. At a velocity of 5 m/s, 10,000 single-frame images are acquired at an acquisition frequency of 8,000 Hz (particle displacement of approximately 27 and 17 pixels for camera 1 and 2 respectively). At 15 m/s, 10,000 single-frame images are acquired at an acquisition frequency of 10,000 Hz (particle displacement of approximately 65 and 42 pixels for camera 1 and 2 respectively). The reference velocity fields are obtained by PIV measurements with micron-sized fog droplets, generated by a SAFEX Twin Fog smoke generator (median particle diameter of 1 μm). A set of 3,000 double-frame images is acquired at an acquisition frequency of 250 Hz with a time separation of 80 and 45 μs for freestream velocities of 5 and 15 m/s respectively. All the experimental settings and parameters are summarised in Table 5.3.

5.3.2 Test matrix

This experiment aims at examining the aerodynamic behaviour of HFSBs in a shear region. The literature survey in subsection 2.4.1 indicates that this lift force is dependent on the bubble diameter, the velocity gradient, the slip velocity of the particle and the viscosity of the surrounding fluid. The bubble diameter is mainly adapted by changing the volume flow rate of the second air flow in the nozzle. A slip velocity can be created by producing non-buoyant HFSBs with different densities.

An extended test matrix is designed with variations of all the nozzle flow rates at 5 m/s. At 15 m/s, the boundary layer is much thinner and it is more difficult to distinguish small variations in supply settings. Therefore, only HFSBs with three different diameters and one

type of air-filled soap bubbles (heavier-than-air bubbles) are studied at a freestream velocity of 15 m/s.

Table 5.3: Experimental parameters of boundary layer experiment with flat plate.

Parameter	**Quantity**	
Seeding	Fog droplets	HFSBs
Velocity	5, 15 m/s	5, 15 m/s
Field of view (FOV)	23.8×9.3 mm^2 and 36.8×14.4 mm^2	
Sensor size	1024×400 pixels and 1024×400 pixels	
Magnification, M_0	0.86 and 0.56	0.86 and 0.56
Focal length, f	200 mm and 105 mm	200 mm and 105 mm
Numerical aperture, $f_\#$	8 and 8	22 and 22
Recording mode	Double frame	Single frame
PIV acquisition frequency	250 Hz	8, 10 kHz
Pulse separation Δt	80, 45 μs	N/A
Number of images, N	2×3,000	8,000, 10,000

Table 5.4: HFSB test matrix of flat plate experiment.

$\mathbf{p_{bfs}}$ [bar]	$\mathbf{p_{He/air}}$ [bar]	$\mathbf{p_{sa}}$ [bar]	$\mathbf{Q_{bfs}}$ [ml/h]	$\mathbf{Q_{he/air}}$ [l/h]	$\mathbf{Q_{sa}}$ [l/h]	Filled with:	5 [m/s]	15 [m/s]
2	2	2	4.78	4.83	115.30	Helium	✓	✓
2.6	2	2	6.20	4.83	115.30	Helium	✓	
2.4	1.8	2	5.73	4.14	115.30	Helium	✓	
1.4	2	2	3.35	4.83	115.30	Helium	✓	
2.9	2	2	6.91	4.83	115.30	Helium	✓	
2	1	2	4.78	1.88	115.30	Helium	✓	
2	1.5	2	4.78	3.20	115.30	Helium	✓	
2	2.5	2	4.78	6.75	115.30	Helium	✓	
2	2	1	4.78	4.83	68.04	Helium	✓	✓
2	2	3	4.78	4.83	162.57	Helium	✓	✓
2	2	2	4.78	5.23	115.30	Air		✓
2.9	2	2	6.91	5.23	115.30	Air	✓	
2	2	1	4.78	5.23	68.04	Air	✓	
2	2	3	4.78	5.23	162.57	Air	✓	

5.4 Image and data processing

This section discusses the software, algorithms and settings that are used to pre-process the images and to evaluate the velocity by PTV and PIV.

5.4.1 Image pre-processing

Image pre-processing is executed with LaVision GmbH Davis 8.2.0. The reference velocity images of the cylinder experiment, i.e. the acquisitions with fog droplets, are pre-processed by subtracting a time filter. The average intensity of each pixel over a series of 13 images is subtracted in a symmetrical way and with the same output format as the input format. In the flat plate experiment, the image pre-processing consists of a subtraction of the average of all the acquired images.

For the HFSBs images of the cylinder and the flat plate experiment, first time series were created since some of the acquisitions were performed in double-frame mode to double the time-resolved, single-frame acquisition frequency (see section 5.2). Afterwards, the minimum intensity of each pixel over a series of 23 images were subtracted from the images. Finally, 20 intensity counts were subtracted from the whole image to filter out the remaining noise.

5.4.2 Helium-filled soap bubbles

The particle tracking velocimetry algorithm of Malik et al. (1993) (discussed in subsection 4.1.1) was implemented in Matlab R2012b. The settings of the PTV algorithm for both the cylinder and the flat plate experiment are summarised in Table 5.5. The velocity predictors are the processed PIV vector fields.

Table 5.5: PTV settings for both the experiments.

Parameter	**Quantity**	
Experiment	Cylinder	Flat plate
Intensity threshold [counts]	15	15
Particle detection search radius [pixels]	3	3
Glare point search radius [pixels]	10	15
Number of frames/track [-]	17	7
Polynomial fit order [-]	3	2

Helium-filled soap bubbles in the cylinder experiment are filtered with the Gubbs' outlier detection algorithm based on particle acceleration and diameter.

Velocity fields around the cylinder based on the HFSB measurements are created by a PIV time-series sum-of-correlation in LaVision GmbH Davis 8.2.0. The cylinder object is excluded from the images using a geometric mask. The vector calculation consists of a cross-correlation of each two consecutive frames. A multi-pass algorithm with decreasing window size is used. Two passes are performed with a window size up to 128×128 pixels with 50% overlap, followed by three passes with a window size up to 16×16 pixels with a (1:1)-round Gaussian weighting function and with 75% overlap. The final passes are performed with a high-accuracy mode (B-spline-6 reconstruction). The final vector fields are post-processed with the universal outlier detection (Westerweel and Scarano, 2005).

5.4.3 Fog droplets

The reference velocity fields of the cylinder and the flat plate, based on the fog droplets measurements, are calculated with the vector calculation - double frames toolbox of LaVision GmbH Davis 8.2.0. The vector calculation consists of a cross-correlation of the images, with a mask over the cylinder object. A multi-pass algorithm with decreasing window size is used. Two passes are performed with a window size up to 128×128 pixels with 50% overlap, followed by three passes with a window size up to 16×16 pixels with a 75% overlap and with a (1:1)-round Gaussian weighting function for the cylinder experiment and a (4:1)-elliptical Gaussian weighting function for the boundary layer on the flat plate. The final passes are done with a high-accuracy mode (B-spline-6 reconstruction). The final vector fields are post-processed with the universal outlier detection of Westerweel and Scarano (2005) and smoothing. Finally, the mean vector field is calculated for each experiment.

Chapter 6

Experimental results

Morias K, Caridi G, Sciacchitano A and Scarano F, Statistical Characterization of Helium-Filled Soap Bubbles Tracing Fidelity for PIV, *18th International Symposium on Application of Laser Techniques to Fluid Mechanics*, Lisbon, Portugal, 04-07 July, 2016

This chapter describes the experimental results of the experiment conducted with a cylinder and aims to address the tracing fidelity of helium-filled soap bubbles experimentally. Section 6.1 starts off with a flow visualization investigation to identify the different working conditions of a bubble nozzle. In section 6.2 the typical recorded images with HFSBs as tracers are described. Mean velocity profiles on the stagnation streamlines for different HFSBs are analysed in section 6.3. Finally, a statistical characterization of the bubble diameter, relaxation time, bubble density and soap film thickness is made in section 6.4 for individual bubbles.

6.1 Flow visualization of nozzle production [1]

The generation process of HFSBs has direct effects on PIV measurements where the bubbles are used as tracers. As discussed by Melling (1997), diameter and density of the seeding particles define their tracking capabilities. Consequently, tracers with monodisperse distribution in size and density are preferable for more accurate measurements. HFSBs are generated with an orifice-type nozzle, as described by Bosbach et al. (2009). The design of the present nozzle was developed in order to produce bubbles in a so-called co-flow configuration, also commonly used for air bubble production in water flows (Sevilla et al. (2005a,b); Gañán-Calvo et al. (2006)). Two different formation regimes are identified: bubbling and jetting. The latter is characterized by a long cylindrical ligament of the discrete phase that breaks up far from the exit of the generator. This results in an aperiodic and polydisperse bubble

[1] This section is a contribution of G.C.A Caridi (G.Caridi@tudelft.nl), for which the author gratefully acknowledges him.

production. Conversely, the bubbling regime features a fairly periodic and stable formation of the bubbles at the exit of the nozzle.

In the present work, the HFSB generator shows similar working regimes to those mentioned above. The details of HFSB formation at the exit of the nozzle are inspected with high-speed shadowgraphy at 90 kHz, with continuous illumination. The results in Figure 6.1 illustrate an example of the stable bubbling regime with rather monodisperse size distribution (Figure 6.1-left). The visualizations also reveal the formation of small droplets at the moment of detachment, either inside or outside the bubble. Although irrelevant for the bubble diameter, this phenomenon may affect the dispersion of bubble weight. In the observed bubbling regime, HFSBs are ejected with a velocity of 20 m/s and with an average separation distance of 440 μm between each other. Hence, the production rate is estimated to be approximately 50,000 bubbles per second. When the bubble generator operates in the jetting regime, a quasi-cylindrical interface of BFS protrudes from the exit of the nozzle. It was observed that the cylindrical film is affected by large scale fluctuations and occasionally breaks up into bubbles far from the orifice. The resulting bubbles are characterized by a broader distribution in diameter, as illustrated in Figure 6.1-right.

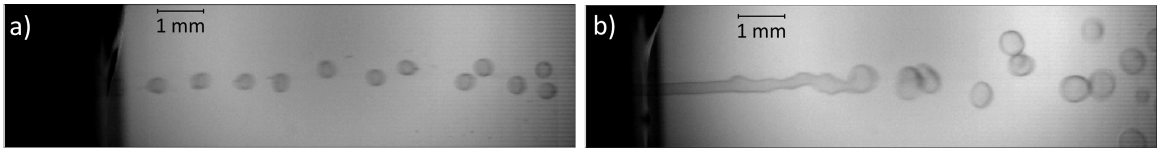

Figure 6.1: High speed visualization of HFSBs production in bubbling (left) and jetting regime (right).

6.2 Image recordings

Recorded images with HFSBs as flow tracers at high magnification look quite different than PIV images with more conventional tracers. First of all, each particle reflects two light spots, the glare spots (discussed in subsection 2.5.4). Secondly, the particle concentration is significantly lower than in PIV images with fog droplets. The latter has usually a particle per pixel *ppp* value between 0.01 and 0.2, which gives in the current frame of 336×704 pixels between 2,370 and 47,300 particles per image respectively. Conversely, in this experiment HFSBs only gave on average 7.43, 4.53 and 1.60 particles/image at freestream velocities of respectively 10, 20 and 30 m/s with a bubble diameter of 370 μm. These values are based on the bubble production of one single nozzle and the plane of illumination is only a fraction of the volume spanned by the HFSBs nozzle. Figure 6.2-top is a pre-processed raw image taken during the measurements at 10 m/s with an average bubble diameter of 370 μm. The contour of the cylinder was added artificially for clarity. Approximately 20 bubbles can be detected in the image. When 500 time-resolved images are summed up, Figure 6.2-bottom is obtained. The latter figure gives already a qualitative insight in the flow structure, since the path lines of the HFSBs can be recognised.

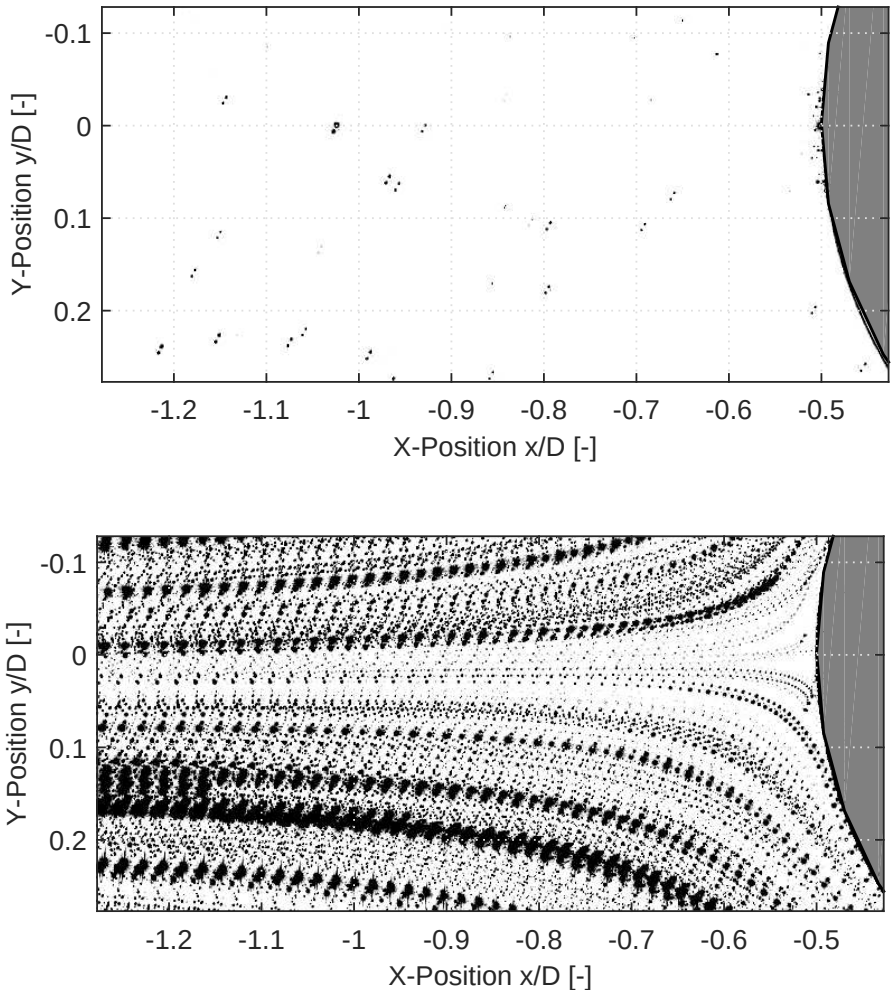

Figure 6.2: Image recordings at freestream velocity of 10 m/s. *Top:* single snapshot. *Bottom:* superposition of 500 time-resolved images.

6.3 Mean velocity fields

Before looking into the aerodynamic and physical properties of the helium-filled soap bubbles, the different test cases are defined. The different soap bubbles are characterized by the FSU supplying flow rates Q_{bfs}, Q_{He} and Q_{sa}, where *bfs*, *He* and *sa* indicate bubble fluid solution, helium and secondary air, respectively. The supply settings for the bubbles discussed in the section are given in Table 6.1. All the measurements are conducted at a freestream velocity of 20 m/s.

Due to the low particle concentration it is impossible to retrieve an accurate velocity field with a cross-correlation between two images. Instead, a mean velocity field is determined by the sum of correlation of all the images for bubbles with given supply flow rates, as discussed in chapter 4. Figure 6.3 shows the mean velocity profile of the stagnation streamline ahead

Table 6.1: Supply flow rates and terminology for different helium-filled soap bubbles (HFSBs) and air-filled soap bubbles (AFSBs).

Name	FSU settings			Terminology
	Q_{He} [l/h]	Q_{bfs} [ml/h]	Q_{sa} [l/h]	
HFSB 1	4.78 (He)	4.83	115.30	Neutrally buoyant bubbles
HFSB 2	4.14 (He)	5.73	115.30	Slightly heavier-than-air
HFSB 3	4.78 (He)	3.35	115.30	Slightly lighter-than-air
HFSB 4	4.78 (He)	4.83	162.57	Small helium-filled soap bubbles
HSFB 5	4.78 (He)	4.83	86.94	Large helium-filed soap bubbles
AFSB 6	5.23 (Air)	4.83	115.30	Heavier-than-air / Air-filled soap bubbles
AFSB 7	5.23 (Air)	4.83	162.57	Small air-filled soap bubbles
AFSB 8	3.79 (Air)	4.83	77.49	Large air-filed soap bubbles

a cylinder for helium-filled soap bubbles. Figure 6.3-left shows bubbles with four different densities and roughly the same diameter (HFSB 1-3 and AFSB 6). The neutrally buoyant HFSBs (HFSB 1) match very well the reference solution (black solid line) that was measured by PIV with fog droplets. The bubbles show a slightly lighter-than-air behaviour as it tends to decelerate earlier than the reference solution. It can be very well observed that when the volume flow rate of helium is lowered and the one of BFS is increased (HFSB 2), the bubbles show a delayed response to the deceleration, indicating they are heavier than air. When the BFS flow rate is lowered with respect to the neutrally buoyant bubble, the bubble becomes lighter than air. The yellow line (HFSB 3) indicates that the velocity is lower than the reference solution, indicating an earlier response to the deceleration on the stagnation streamline. These observations are in line with the results reported by Scarano et al. (2015).

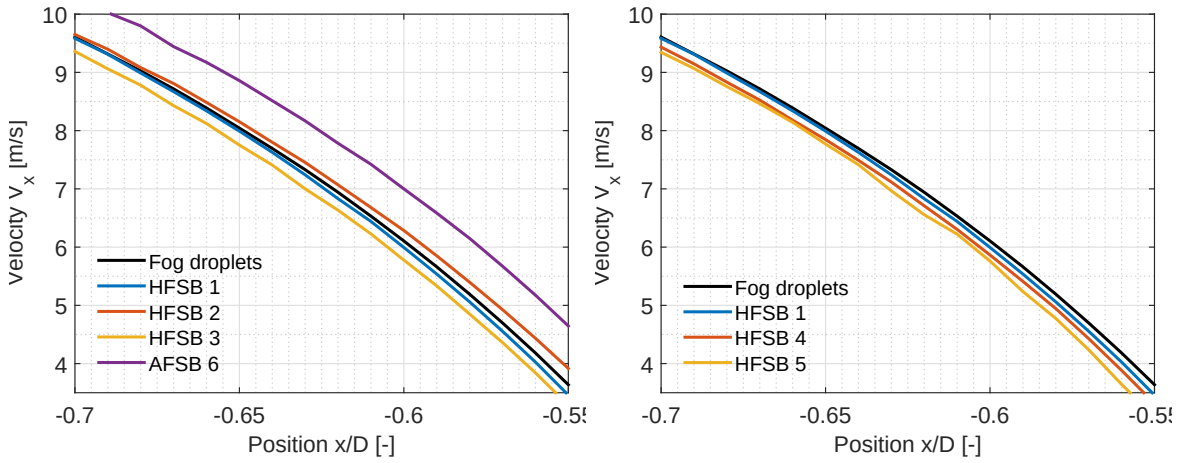

Figure 6.3: Mean velocity profile along the stagnation streamline ahead of a cylinder by sum-of-correlation of all the images.

Figure 6.3-right contains the velocity profiles of bubbles with three different diameters and roughly the same density. The bubbles with a lower secondary airflow rate (HFSB 5), i.e. larger bubbles, show lighter-than-air behaviour with lower velocities than the reference so-

lution. This can be explained by the fact that the neutrally buoyant bubbles (blue line in Figure 6.3-left) show some lighter-than-air behaviour as well. Assuming that the density of the bubbles stays constant (as explained in section 3.1), its influence on the aerodynamic behaviour is enlarged since the relaxation time τ_p scales with the second power of the diameter. In that sense, the bubbles with a higher secondary airflow rate (HFSB 4), i.e. smaller bubbles, were expected between the reference solution and the medium-sized bubbles. However, the red line (smaller bubbles) lies clearly in between the medium-sized and the large bubbles. The cause can probably be found in the fact that the bubble production was unstable (jetting regime) and thus soap droplets were formed and spit out of the nozzle, resulting in a significant loss of soap in the bubbles. This unstable behaviour is further investigated in subsection 6.4.3.

6.4 Individual bubble analysis

In order to be able to analyse each bubble individually, particle tracking velocimetry (PTV) is applied through the recorded bubble positions. In total 2,079 bubbles and thus tracks are detected in the field of view for neutrally buoyant bubbles. Each bubble is recorded on average 26 times in the field of view. Since each track consists of 17 consecutive exposures and is evaluated in the middle of the track, it means that there are on average 10 velocity and acceleration recordings of each bubble. Figure 6.4 is a superimposition of all neutrally buoyant bubble tracks, with the color indicating the total velocity of the bubble. The whole field of view is well covered by the tracks.

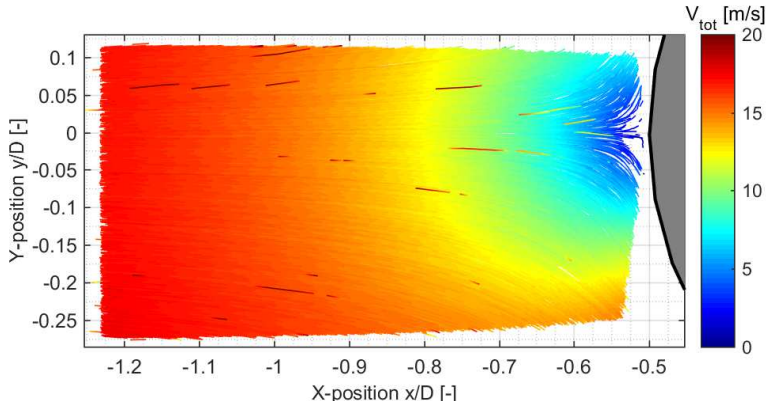

Figure 6.4: Superimposition of all tracks for neutrally buoyant bubbles (HFSB 1).

6.4.1 Mean velocity and acceleration profiles along stagnation line

The mean velocity and acceleration profiles of two different soap bubbles (HFSB 1 and AFSB 6) on the stagnation streamline at a freestream velocity of 20 m/s are illustrated in Figure 6.5. The results are shown with the reference data obtained by PIV measurements with fog droplets. The uncertainty is illustrated with error bars that represent the standard devi-

ations of the measurements. Figure 6.5 shows that the mean velocity and acceleration profile of the neutrally buoyant bubbles are in agreement with those of the fog measurements. The velocity difference in the X-direction up to x/D = -0.6 is at most 0.05 m/s. The heavier-than-air air-filled soap bubbles (AFSB 6) profile exhibits the expected offset, indicating a delayed response to the decelerating flow and confirming the observations of Scarano et al. (2015). This delay is also clearly visible in the acceleration profile, where heavier-than-air bubbles exhibit lower acceleration for x/D < -0.7.

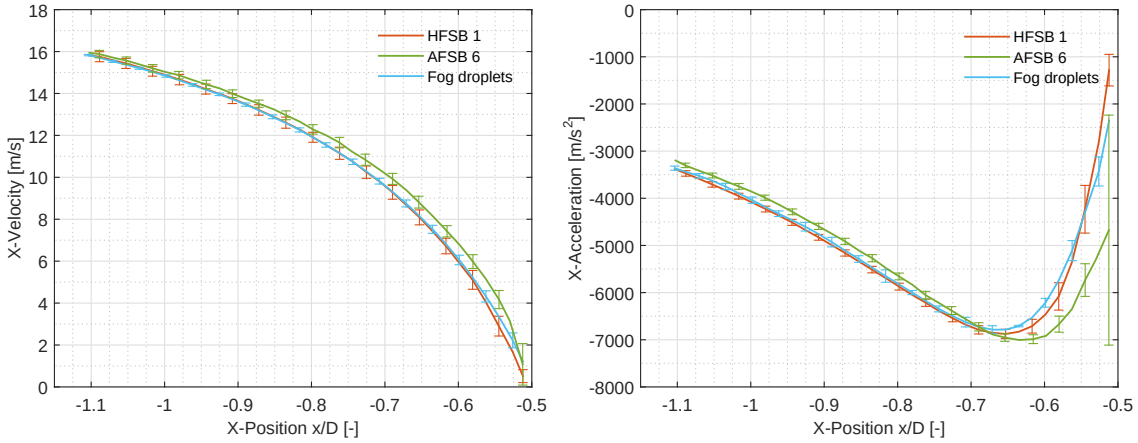

Figure 6.5: Mean velocity (left) and acceleration (right) profiles on the stagnation streamline ahead the cylinder.

6.4.2 Slip velocity, particle acceleration and relaxation time

Largely heavier-than-air (air-filled) soap bubbles (AFSB 6) are considered first. The slip velocity and relaxation time of these bubbles are showed in Figure 6.6. Since the bubble velocity and acceleration are determined by means of PTV, they feature low measurement uncertainty. Random measurement errors on the bubble position are strongly reduced by fitting a third-order polynomial through the series of seventeen data points. The reference velocity field is computed as the time-average of 3,000 instantaneous uncorrelated velocity fields. The turbulence intensity of the wind tunnel is measured to be 0.5% at a freestream velocity of 20 m/s. Since the bubble recordings and the fog droplet measurements are not made simultaneously, velocity differences up to ±0.1 m/s can occur that are not due the aerodynamic behaviour of the bubbles, but solely to the freestream turbulence intensity. This uncertainty in the slip velocity calculation is indicated by black dashed lines in Figure 6.6. The light-blue dots represent individual bubble recordings, while the red line is the mean of all recordings and the error bars indicate one standard deviation of the distribution.

In the range x/D=[-1.1 -0.7], the acceleration approximately doubles (see Figure 6.6-right). Since the correction factor Φ depends on the particle Reynolds number less than linearly Schiller and Naumann (1933), the relaxation time can be assumed constant for small variations of the slip velocity. Assuming a constant relaxation time τ_p, also the slip velocity is expected

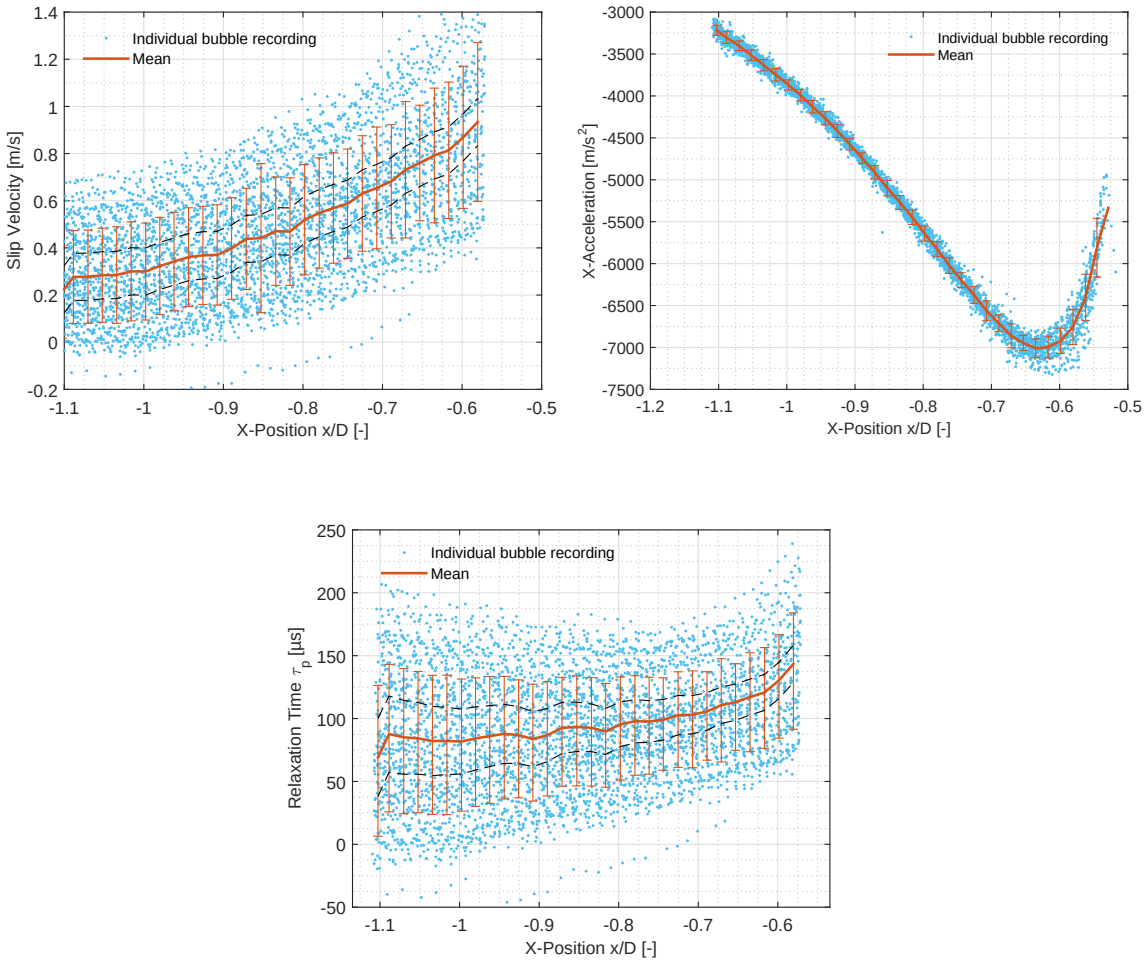

Figure 6.6: Slip velocity (left), acceleration (right) and relaxation time (bottom) of individual bubbles on the stagnation line of the cylinder for heavier-than-air air-filled soap bubbles (AFSB 6). Black dashed lines indicate the uncertainty due to the freestream turbulence intensity.

to double. The results of Figure 6.6-left show an approximately linear increase of the slip velocity. While the mean value of $\mathbf{u}_{\text{slip}}$ doubles in the considered x/D range, the standard deviation instead has a smaller increase. This result is ascribed to the slight overestimation of the slip velocity due to the effect of freestream turbulence. This effect is larger away from the cylinder (x/D < -0.9), where the slip velocity is expected to be lower. For the same reason, the standard deviation of the relaxation time is probably overestimated when computed far away from the cylinder (see Figure 6.6-bottom). The results are further analysed in the interval x/D=[-0.75 -0.65], where the flow deceleration is the strongest, resulting in the largest slip velocity and the lowest relative influence of freestream turbulence intensity. Here the average slip velocity is approximately 0.7 m/s with a standard deviation of 0.26 m/s, giving a mean relaxation time of approximately 98 μs with a standard deviation of 38 μs. This indicates the poor tracing fidelity of air-filled soap bubbles and further confirms the need of helium as filling gas to counterbalance the weight of the soap film. The slip velocity and relaxation time

of nearly neutrally buoyant HFSBs (HFSB 1) are analysed in Figure 6.7.

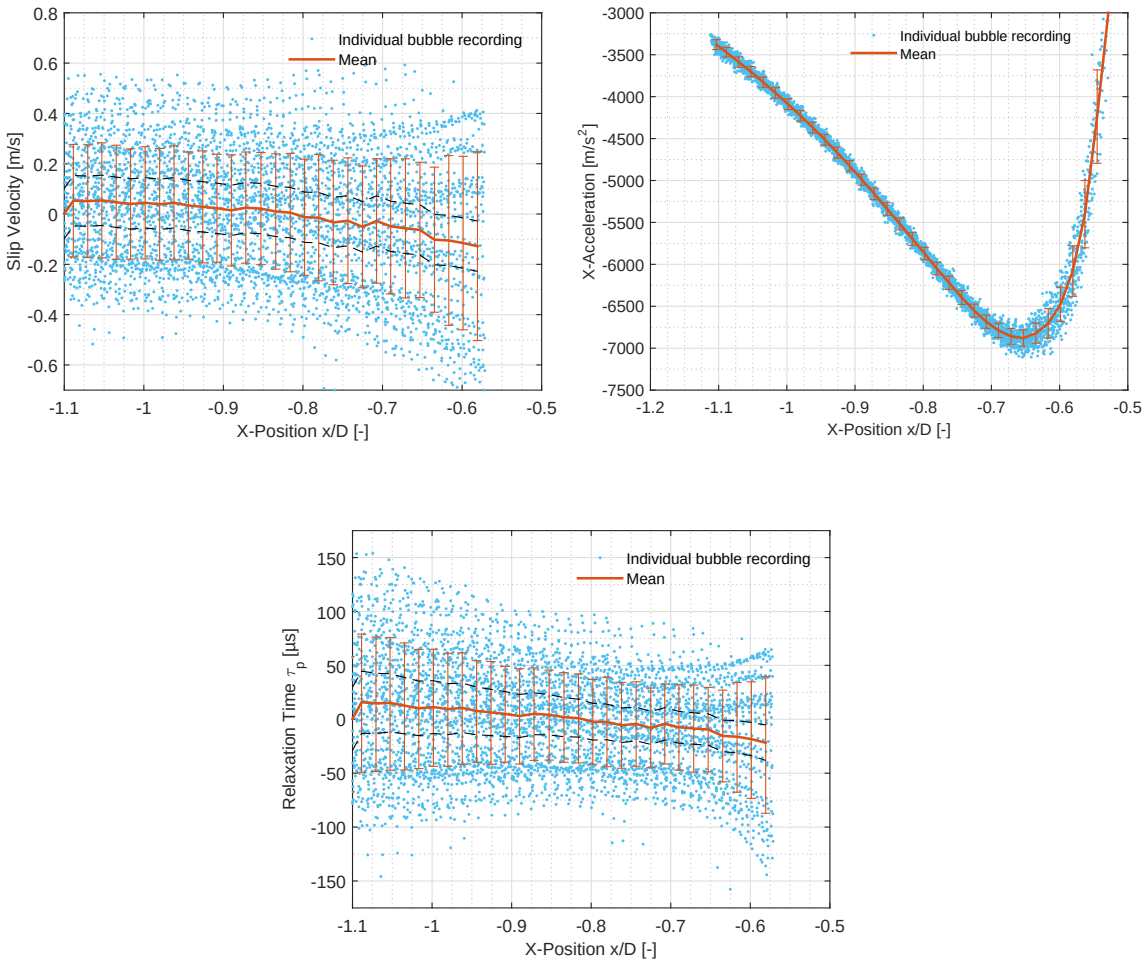

Figure 6.7: Slip velocity (left), acceleration (right) and relaxation time (top) of individual bubbles on the stagnation line of the cylinder for neutrally buoyant helium-filled soap bubbles (HFSB 1). Black dashed lines indicate the uncertainty due to the freestream turbulence intensity.

The mean slip velocity is approximately zero for x/D < -0.9 and slightly increases approaching the cylinder. The uncertainty due to the turbulence intensity is again indicated with black dashed lines. The magnitude of the slip velocity and the uncertainty due to the turbulence intensity are of the same order. For the same reason as before, the results are analysed in the interval x/D=[-0.75 -0.65]. The mean slip velocity is around 0.05 m/s with a standard deviation of 0.25 m/s, yielding a mean relaxation time of less than 10 μs, with a more significant standard deviation of approximately 40 μs. Remember that lighter than air HFSBs exhibit a negative response in Figure 6.7-bottom. The acceleration measurements in the X-direction yield a standard deviation of 60 m/s^2, slightly increasing closer the cylinder.

In a similar way the relaxation time of HFSB 2 and 3 is investigated. Figure 6.8 shows the distribution of the relaxation time of the particles along the stagnation line for both

bubble types. For Figure 6.8-left (HFSB 2) the time response indicate a slightly heavier-than-air particle, although still close to the neutral buoyancy condition. On the other hand, Figure 6.8-right (HFSB 3) indicates clear lighter-than-air bubbles with a relaxation time of on average -50 μs along the stagnation line. This proves the ability of the present nozzle to generate both lighter-than-air, neutrally buoyant and heavier-than-air bubbles.

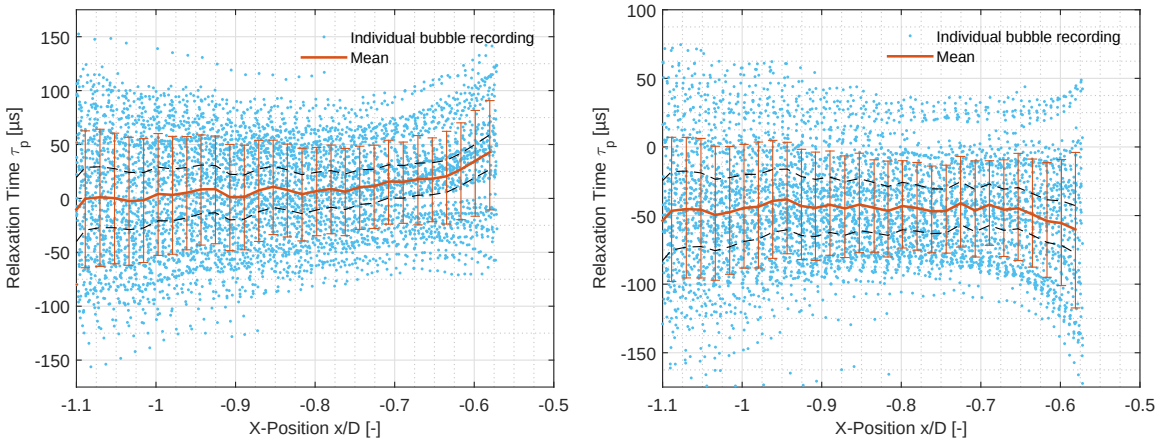

Figure 6.8: Relaxation time of individual bubbles on the stagnation line of the cylinder for neutrally buoyant helium-filled soap bubbles. Black dashed lines indicate the uncertainty due to the freestream turbulence intensity. *Left:* HFSB 2. *Right:* HFSB 3.

6.4.3 Bubble diameter statistics

For neutrally buoyant HFSBs (HFSB 1), the statistical distribution of the measured bubble diameter is approximately Gaussian, as depicted in Figure 6.9-left. The average bubble diameter is 370.7 μm. This corresponds to an average glare point distance of 5.42 pixels. The standard deviation of the distribution is 16 μm or 0.33 pixels. Therefore the distribution is monodisperse, indicating that the nozzle operates in the bubbling regime and produces bubbles within 5% variations in diameter. The uncertainty of the bubble diameter is determined by dividing the standard deviation of the diameters of all the recordings of each bubble by the square root of the number of recordings of that bubble. The histogram of the diameter measurement uncertainty in Figure 6.9-right approximates a Poisson distribution with its peak at 2.6 μm or 0.054 pixels. Hence, the measurement uncertainty is less than 1 % of the bubble diameter. As a result, the measured 5% variation in diameter showed in Figure 6.9-left is due to a bubble production process that is not perfectly repeatable.

However, for HFSBs with the same volume flow rates of helium and soap, but with a higher flow rate of the secondary air flow (Q_{sa}=162.57 l/h) the diameter distribution in Figure 6.10-right is not longer monodisperse. The distribution features a peak around 340 μm, but seems to have a secondary smaller peak with a higher standard deviation between 200 and 250 μm. Diameter variations up to 20 % of the mean diameter are observed. This unstable behaviour is caused by the nozzle operating in the jetting regime. The same approach is applied to

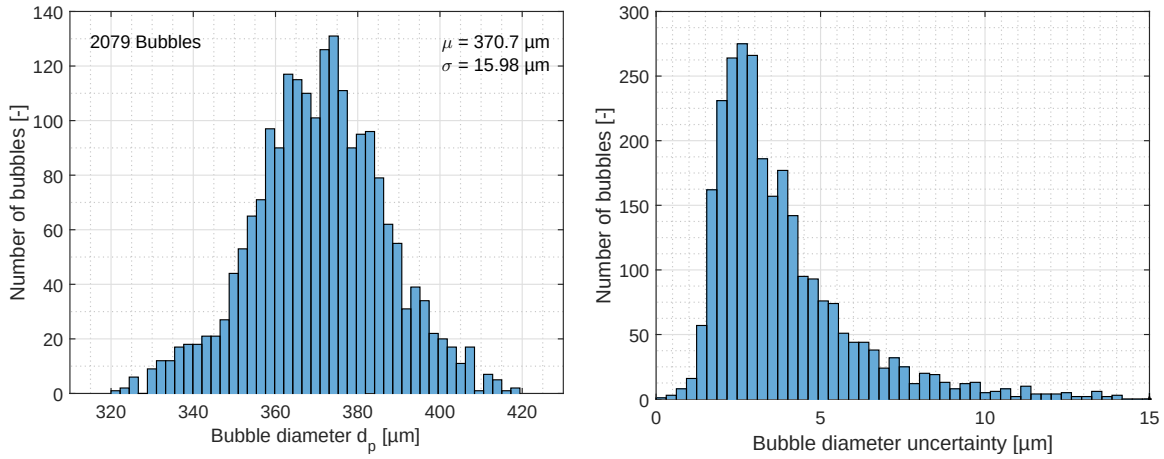

Figure 6.9: HFSB diameter statistics. Left: diameter distribution. Right: diameter uncertainty.

helium-filled soap bubbles and air-filled soap bubbles with different supply flow rates. The results are summarised in Table 6.2. A higher Q_{bfs} seems to have a stabilizing effect on the dispersion in bubble diameter for a constant flow rate of air. This is visualised in Figure 6.9-left, where an increase of Q_{bfs} results in a lower spread of the bubbles diameter. At Q_{sa}=163 l/h (HFSB 4 and AFSB 7), an unstable bubble production is reported, which is ascribed to the jetting regime. The bubble diameter distribution at this condition is rather broad and non-Gaussian, as illustrated in Figure 6.9-right for HFSB 4. As a result, the statistical values of bubble diameter exhibit a relatively large standard deviation.

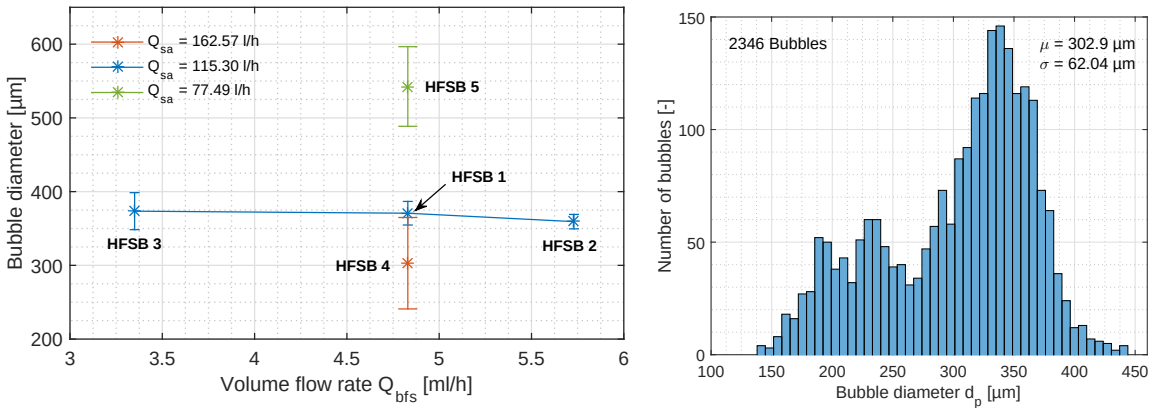

Figure 6.10: The influence of the Q_{bfs} on the bubble diameter statistics (left) and an example of the unstable bubble production for HFSB 4 (right).

From the diameter observations in HFSB 1,2 and 3, it is found that the volume flow rate of helium has a minor effect on the diameter. A higher helium flow rate will slightly increases the bubble diameter. In case of stable production, a higher volume flow rate of the secondary airflow in the nozzle induces smaller bubbles, while a lower volume flow rate makes the bubbles

bigger. This is confirmed by the diameter observations of HFSB 5 and HFSB 4, although the latter has an unstable production. Consequently, the production rate of the bubbles depends on the flow rate of air.

6.4.4 Bubble density statistics

Knowing the relaxation time and the bubble diameter, the bubble density can be determined (see section 4.2). The density is calculated for each bubble individually, with its own relaxation time as function in time and the mean diameter of that specific bubble. Figure 6.11-left illustrates the bubble density of each bubble along the stagnation line of the cylinder for neutrally buoyant bubbles (HFSB 1). The errorbars indicate again one standard deviation of the distribution. In the interval x/D=[-0.75 -0.65] the mean density value of the HFSBs is found to be 1.18 kg/m^3 and the standard deviation is measured to be 0.16 kg/m^3. The density of air in the laboratory was 1.213 kg/m^3, giving a specific density $\bar{\rho}$=0.97 $\pm$ 0.13. The same analysis is performed for air-filled soap bubbles (AFSB 6) in Figure 6.11-right. In the same interval, the mean specific density value is 1.59 kg/m^3 and the standard deviation is measured to be 0.16 kg/m^3, giving a specific density of $\bar{\rho}$=1.304 $\pm$ 0.14.

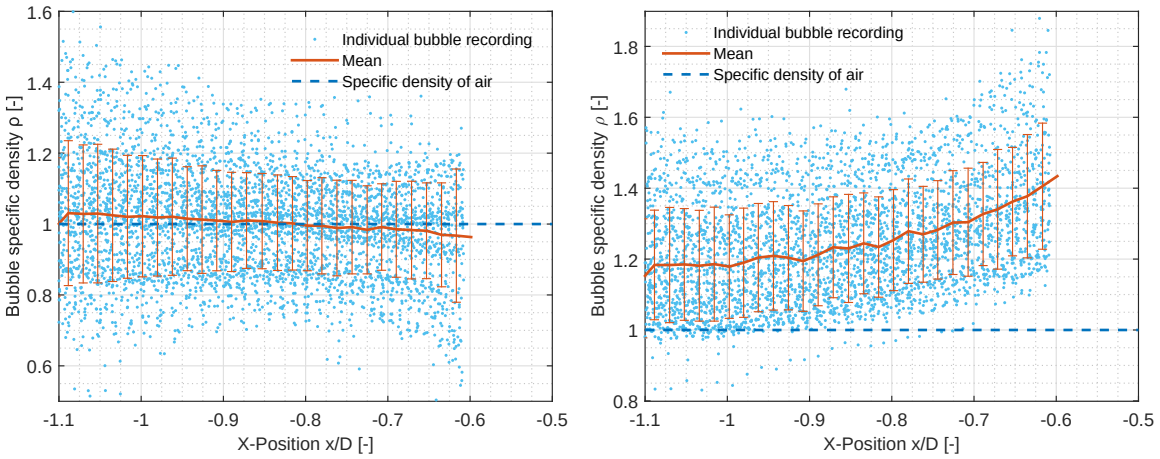

Figure 6.11: Bubble density of individual bubbles on the stagnation line of the cylinder. *Left:* Neutrally buoyant helium-filled soap bubbles (HFSB 1). *Right:* Air-filled soap bubbles (AFSB 6).

From Figure 6.11-left it can be seen that the bubble density is almost constant along the stagnation streamline. The small linear variation most likely originates from a small difference between the HFSBs and reference measurements. A nearly constant density is found for all the measurements with helium-filled soap bubbles, who all exhibit small deviations from the neutrally buoyancy condition. The air-filled soap bubbles, however, clearly do not have a constant density along the stagnation line. In the case of AFSB 6 (Figure 6.11-right), they experience an exponential increase in density along the streamline. This is of course not physical. Air-filled soap bubbles are much heavier than air and are therefore bad tracers. They will deviate from the reference streamlines and will experience different accelerations than the

reference accelerations. This makes the assumption of equal particle and fluid acceleration invalid and causes a significant violation from the constant particle density requirement. Figure 6.12 plots the specific density of all tested bubbles in function of the volume flow rate ratio $Q_{\text{He}}/Q_{\text{bfs}}$. The asterisks indicate the mean values and the error bars one standard deviation of the distribution.

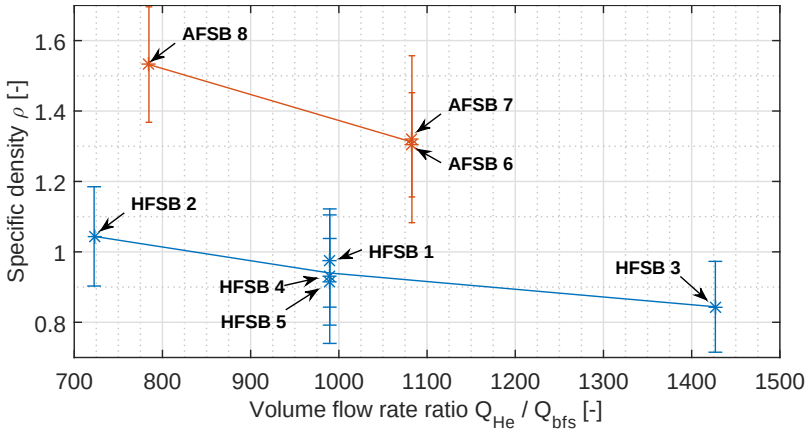

Figure 6.12: The influence of the ratio Q_{He}/Q_{bfs} on the bubble density statistics.

From the first three combinations a smaller ratio Q_{He}/Q_{bfs} (i.e. more soap per unit volume helium) increases the density of the bubble. As such, it is possible to generate heavier-than-air bubbles (HFSB 2), nearly neutrally buoyant bubbles (HFSB 1) and lighter than air bubbles (HFSB 2). Furthermore, it confirms the observations from section 3.1 that the particle density is independent of the bubble diameter for HFSBs, since HFSB 1, 4 and 5 are having different diameters, but still roughly the same specific density. Therefore, it can be safely concluded that the density of HFSBs are a function of the ratio Q_{He}/Q_{bfs} only. A comparison to the theoretical values reported in section 3.1 shows an experimental underestimation of the density in HFSB 2 of 27,5% with respect to the theoretical value, an underestimation of 10 % of HFSB 1 and an overestimation of the density for HFSB 3 with 6.25 %. The most likely causes are the errors made by the methodology (see section 3.2) and losses in the FSU, pipeline system and bubble nozzle that damp out big differences in density.

AFSBs 6 and 7 confirms the observations from the helium-filled soap bubbles that the density of (air-filled) soap bubbles is independent of the diameter. All the reported air-filled soap bubbles show an underestimation of approximately 29 % in specific density compared to the expected theoretical values. This difference is most likely due to the neglecting the added-mass force in the current analysis. Also the history force is neglected and is expected to play a more prominent role in case of bad tracers. Furthermore, since every measurement with air inside the bubbles is conducted after a measurement with helium. It might be possible that the helium was not yet fully removed out of the pipelines between the FSU and the nozzle. However this cause is considered unlikely, since then some of the helium-filled soap bubbles are expected to suffer from heavier-than-air behaviour, which is not the case. Lastly, this investigation considers a no-slip condition at the soap film. In other words: soap bubbles are approximated as solid particles in air for the drag term and not as gas bubbles in water. This assumption still seems valid from a physical point of view, but since the exact drag behaviour

for soap bubbles is unknown, it might have an unknown effect on the above mentioned data.

6.4.5 Bubble film thickness statistics

Based on the density of the bubbles and the theoretical model that was developed in section 3.1, it is possible to estimate the film thickness of the soap bubbles (see section 4.2). Figure 6.13 illustrates the soap film thickness of all the neutrally buoyant HFSBs (HFSB 1) along the stagnation streamline. In the interval x/D = [-0.75 -0.65] the mean soap film thickness is found to be 53.65 nm with a standard deviation of 9.24 nm.

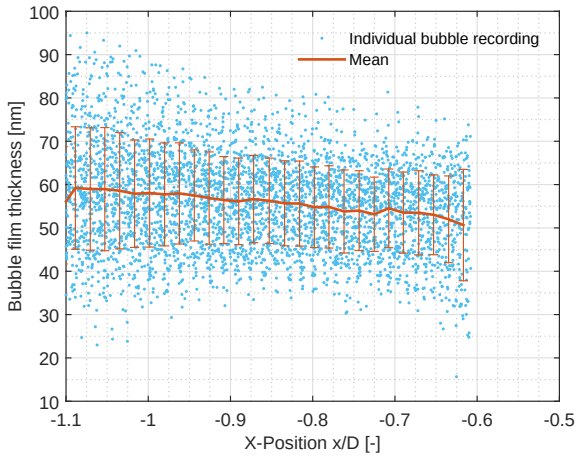

Figure 6.13: Bubble soap film thickness of individual bubbles on the stagnation line of the cylinder for neutrally buoyant helium-filled soap bubbles (HFSB 1).

This procedure is again repeated for all the different helium-filled soap bubbles and air-filled soap bubbles. The accuracy of the soap film thickness calculation depends on the accuracy of the particle density calculation. In the latter section, some doubts were raised on the accuracy of the AFSBs density results. Consequently, the reported film thickness values will also deviate from the theoretical results. The soap film thicknesses of each bubble together with all the results obtained so far are summarized in Table 6.2.

Table 6.2: Diameter, relaxation time and density statistics for different helium-filled soap bubbles.

Name	**FSU settings**			**Diameter [μm]**		**Relaxation time [μs]**	
	Q_{He} [l/h]	**Q_{bfs} [ml/h]**	**Q_{sa} [l/h]**	**Mean μ**	**SD σ**	**Mean μ**	**SD σ**
HFSB 1	4.78	4.83	115.30	370.7	16.0	-6.8	38.9
HFSB 2	4.14	5.73	115.30	359.3	9.8	12.8	39.3
HFSB 3	4.78	3.35	115.30	373.5	25.1	-44.4	33.7
HFSB 4	4.78	4.83	162.57	302.9	62.0	-24.6	32.5
HSFB 5	4.78	4.83	86.94	542.6	54.0	-39.6	51.5
AFSB 6	5.23	4.83	115.30	437.2	23.7	98.1	37.3
AFSB 7	5.23	4.83	162.57	365.3	71.3	89.4	23.8
AFSB 8	3.79	4.83	77.49	549.3	11.3	193.0	42.2

Name	**FSU settings**			**Specific density [-]**		**Film thickness [nm]**	
	Q_{He} [l/h]	**Q_{bfs} [ml/h]**	**Q_{sa} [l/h]**	**Mean μ**	**SD σ**	**Mean μ**	**SD σ**
HFSB 1	4.78	4.83	115.30	0.974	0.131	53.65	9.24
HFSB 2	4.14	5.73	115.30	1.044	0.141	56.58	9.87
HFSB 3	4.78	3.35	115.30	0.844	0.129	46.12	9.19
HFSB 4	4.78	4.83	162.57	0.931	0.191	42.87	7.36
HSFB 5	4.78	4.83	86.94	0.915	0.123	70.28	12.83
AFSB 6	5.23	4.83	115.30	1.304	0.148	23.26	11.62
AFSB 7	5.23	4.83	162.57	1.324	0.108	21.36	7.13
AFSB 8	3.79	4.83	77.49	1.532	0.164	51.10	16.34

Chapter 7

Experimental results: laminar boundary layer

In this chapter the results of the experiment with helium-filled soap bubbles as tracer particles in a laminar boundary layer on top of a flat plate are discussed. Section 7.1 discusses the reference solution of the boundary layer as determined by PIV measurements with fog droplets. Section 7.2 investigates the presence and behaviour of helium-filled soap bubbles as tracers inside the laminar boundary layer.

7.1 Reference solution

In this first section, the reference solution of the boundary layer on top of a flat plate with a freestream velocity of approximately 5 m/s is discussed. This solution is determined by PIV measurements with fog droplets as tracer particles, as discussed in chapter 5. The velocity vectors are determined by means of a standard FFT cross-correlation in LaVision GmbH Davis 8.2. Figure 7.1 shows the boundary layer 300 mm downstream the flat plate's leading edge. Since the flat plate is inclined with -2 degrees to prevent flow separation on the sharp leading edge and the plate is installed in a closed test section, the actual boundary layer is a flat plate boundary layer with a favourable pressure gradient. Figure 7.1-top shows the distribution of the velocity component parallel to the plate. Figure 7.1-bottom illustrates the strength of the shear in the boundary layer. Close to the flat plate, a velocity gradient up to 2150 s^{-1} is present, decreasing to approximately 0 in the freestream flow. The black dotted line in the two latter figures indicates the location where the velocity profile of the boundary layer is studied in Figure 7.2.

The velocity profile of the boundary layer is analysed along the black dotted line in Figure 7.1. This line is perpendicular to the flat plate surface, approximately 305 mm downstream the leading edge. Figure 7.2-left visualizes the velocity component parallel to the plate surface $u_{x'}$ along that black line. From this it is found that the freestream velocity U_0 equals 5.195 m/s at this location. The boundary layer thickness δ_{99}, based on a 99 % recovery of the velocity,

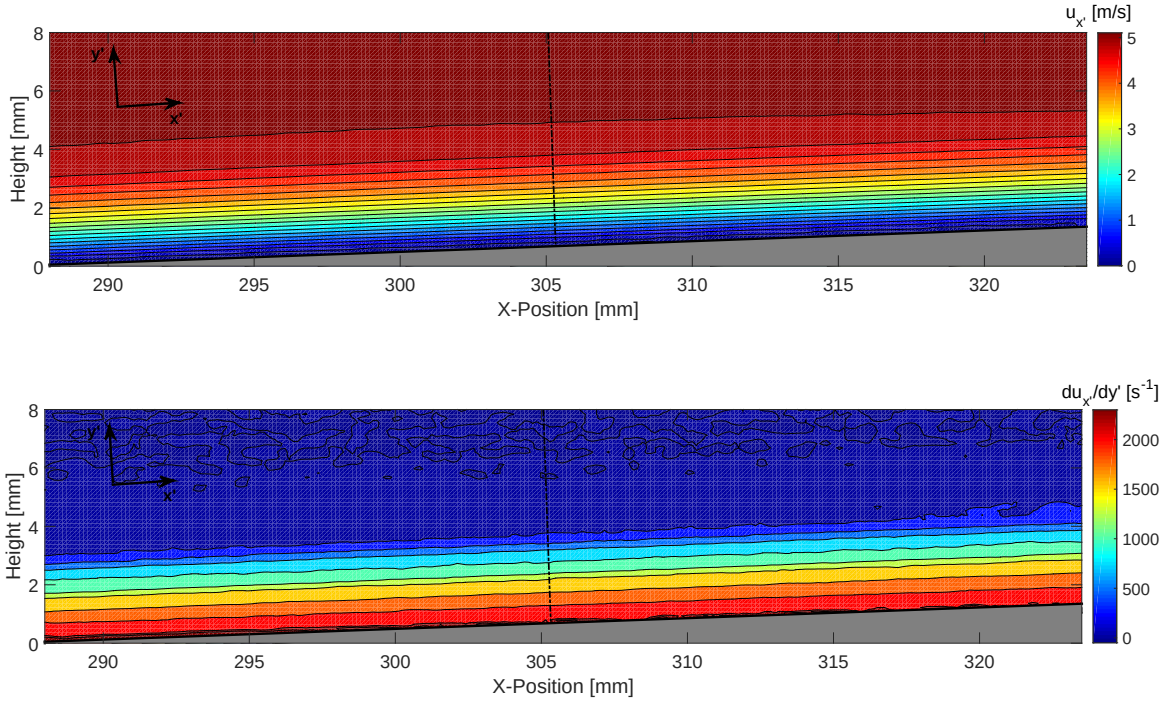

Figure 7.1: Boundary layer 300 mm downstream the leading edge, measured by PIV with fog droplets. *Top*: Velocity $u_{x'}$. *Bottom*: Shear $\frac{du_{x'}}{dy'}$.

equals 4.53 mm. The velocity profile between 0 and 0.35 m/s was extrapolated by means of a second order polynomial from the profile between 0.35 m/s and 4 m/s. Figure 7.2-right shows the velocity profile of the boundary layer in non-dimensional variables. The boundary layer features a displacement thickness δ^* of 1.30 mm and a momentum thickness θ of 0.51 mm. This renders a shape factor H of 2.53, which is slightly lower than the shape factor of the Blasius solution (H=2.61) and confirms the laminar regime of the current boundary layer (White, 2005). The slightly lower shape factor is according to expectations due to the favourable pressure gradient.

The second camera is used to visualise the flow field around the leading edge of the flat plate. Figure 7.3 shows the development of the thin boundary layer on top of the flat plate leading edge. It starts off as a boundary layer with a thickness of only 0.4 mm at a position of 2 mm downstream the leading edge, growing towards a boundary layer thickness of approximately 0.65 mm at 12 mm downstream the leading edge. The boundary layer is not well resolved close the flat plate surface due to limitation of spatial resolution in such a thin boundary layer and due to reflections of the laser light on top of the plate.

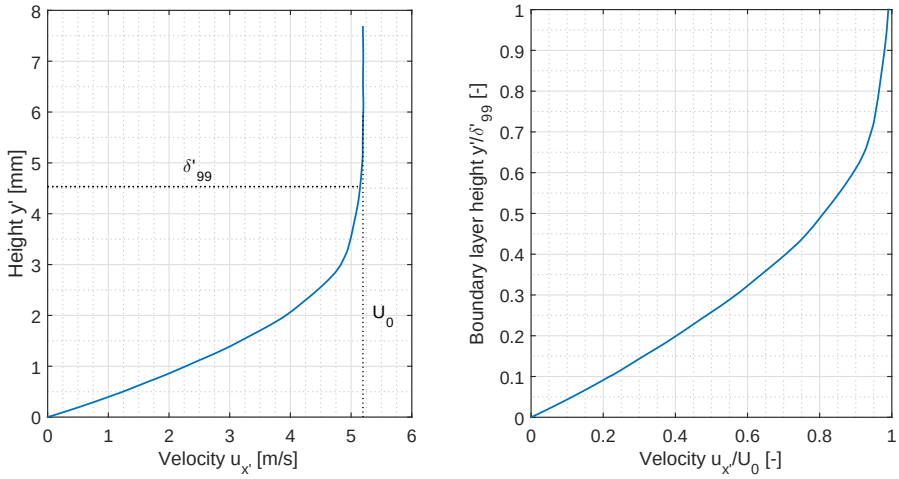

Figure 7.2: Velocity profiles along a line perpendicular to the flat plate, approximately 305 mm downstream the leading edge, measured by PIV with fog droplets. *Left*: full, dimensional velocity profile $u_{x'}$. *Right*: non-dimensional boundary layer velocity profile $u_{x'}/U_0$.

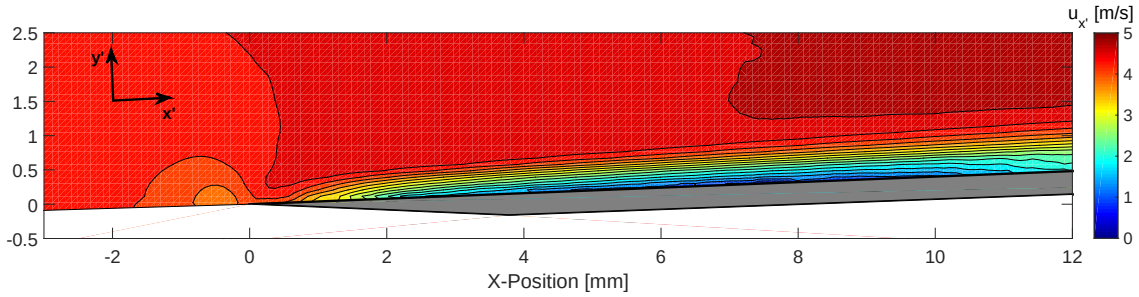

Figure 7.3: Boundary layer on the leading edge, measured by PIV with fog droplets: velocity $u_{x'}$.

7.2 Helium-filled soap bubbles inside a laminar boundary layer

Three different helium-filled soap bubbles are considered: small-sized, medium-sized and large-sized bubbles. They are created by applying FSU supplying volume flow rates Q_{He}=4.78 l/h, Q_{bfs}=4.83 ml/h and Q_{sa}= 162.57, 115.30 and 86.94 l/h respectively. For those three cases, the positions of all the bubble recordings are visualised with a blue dot on top of the contour plot of the fog droplets measurements in Figure 7.4. These positions indicate the center of the bubbles.

It can clearly be seen that all the three images have a region that is empty of particles close to the flat plate surface. The height of this region seems to strongly depend on the bubble diameter. Figure 7.4-top (small bubbles) has an empty region of less than approximately 1 mm, Figure 7.4-middle (medium-sized bubbles) approximately 1.25 mm and Figure 7.4-bottom (large bubbles) slightly more than 2 mm. A sliding average of the number of particles

along the middle black line perpendicular to the flat plate surface is performed. The number of particles in the sliding box divided by the number of the particles in the sliding box in the freestream is plotted in function of the height in Figure 7.5. Defining a threshold of 0.5 for the non-dimensional particle concentration, the same values as mentioned before are confirmed. Moreover, the particle concentration is increased to a value of approximately 1.4 just above the empty region, before the concentration drops back to the freestream value 1. This indicates that the particles missing in the empty region are concentrated just on top of that empty region. These empty regions can be an indication that a transverse lift force is present, that makes the particles move away from strong shear regions. There is, however, another physical phenomenon that needs to be taken into account first, before concluding on the effect of shear on the bubbles.

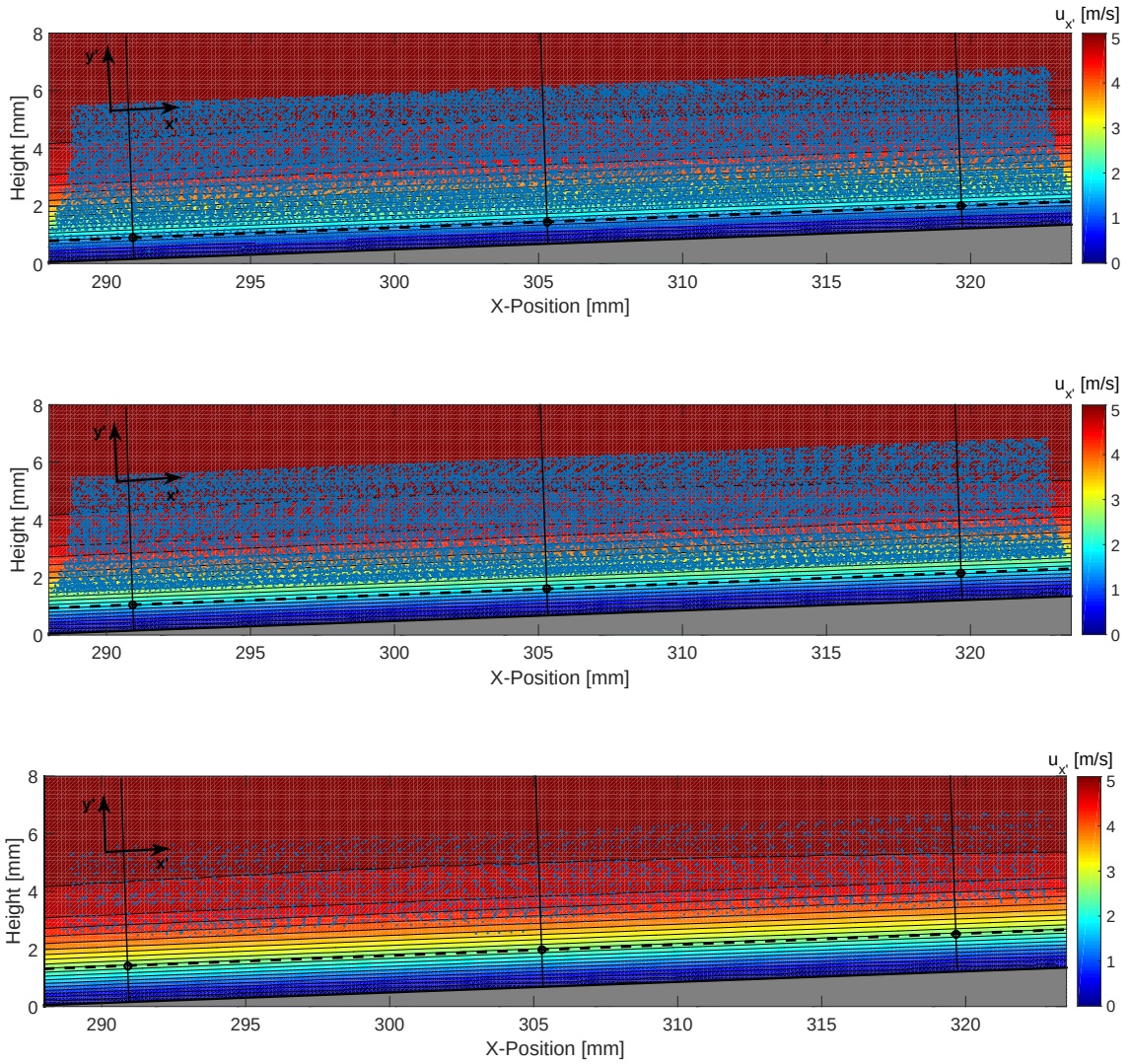

Figure 7.4: Boundary layer 300 mm downstream the leading edge. Contour levels are velocity $u_{x'}$ measured by PIV with fog droplets. *Top*: small bubbles (d_p=200 μm). *Middle*: medium bubbles (d_p=300 μm). *Bottom*: large bubbles (d_p=600 μm).

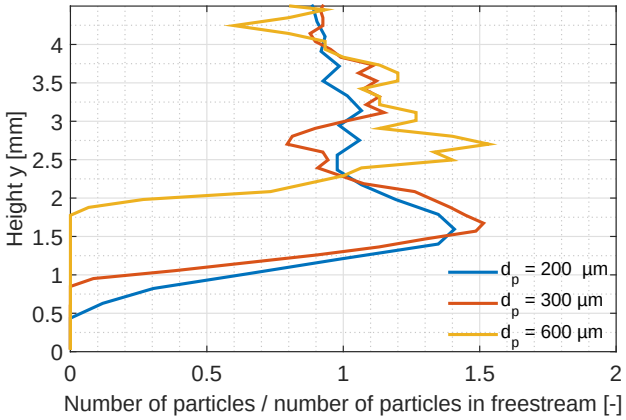

Figure 7.5: Particle concentration inside the boundary layer for different bubble diameters d_p.

Consider a spherical particle far upstream the leading edge of a flat plate. Then, define a streamtube with inner dimensions identical to those of the spherical particle radius and with a velocity equal to the freestream velocity u_0. The bottom of this streamtube is aligned with the flat plate surface. When the streamtube arrives at the flat plate, it will be slowed down by the friction between the airflow and the plate surface (no slip condition). In order to fulfill the conservation of mass principle, the streamtube has to expand inside the boundary layer. As such, it is possible to estimate the empty region inside the boundary for a particle of a given diameter d_p. A streamtube with a radius smaller than the particle radius $d_p/2$ will cause an empty region in the boundary layer, as it could not contain a single bubble upstream the leading edge. Mathematically the height of the empty region y_{empty} can be calculated from:

$$u_0 \frac{d_p}{2} = \int_0^{y_{\text{empty}}} u(y)dy \tag{7.1}$$

where u_0 is the freestream velocity, d_p the particle diameter and $u(y)$ the velocity profile inside the boundary layer. This theory is visualized in Figure 7.6. The red dotted line indicates a streamtube far upstream the flat plate en illustrates how this streamtube expands inside the boundary layer. The upper line can be considered as a streamline that coincidences with the center of the particle.

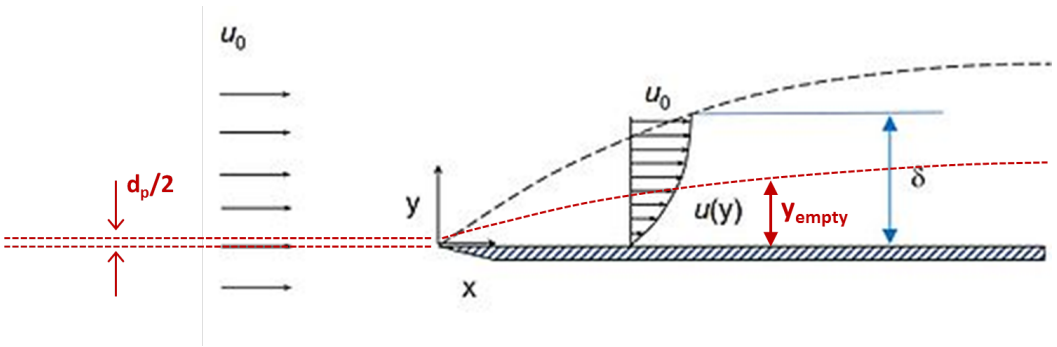

Figure 7.6: Expansion of a stream tube far upstream and inside a boundary layer of a flat plate, based on the conservation of mass.

This theory is applied to the images in Figure 7.4. The small-sized, medium-sized and large-sized bubbles have a mean diameter of 200 μm, 300 μm and 600 μm respectively (determined by glare-points distance). The corresponding expected empty region in the boundary layer is indicated with a dotted black line. The empty height was calculated along the three positions in the boundary layer that are indicated with solid black lines. The streamtube-theory seems to be under-predicting the empty region for all the three cases. The discrepancy between the predicted and the observed empty region is growing for increasing particle diameters d_p. Therefore, it can be concluded that for HFSBs in a laminar boundary layer, the shear might be an influencing factor and might cause the bubbles to move upward in the boundary layer, resulting in an empty region in the boundary layer that cannot be explained by any other theory. If that is the case, the bubbles would have moved upwards over a height of approximately 0.5 mm over a length of 300 mm for large-sized HFSBs.

A quick investigation of the HFSBs in the boundary layer at the leading edge is performed by inspecting Figure 7.7. For the large-sized bubbles (Figure 7.7-bottom) it seems that the bubbles are just outside the boundary layer or in the top layer of the boundary layer further downstream the leading edge. The medium-sized bubbles appear in the top layers of the boundary layer and the small bubbles can be found back in the top half of the boundary layer. At a position 4 mm downstream of the leading edge, the boundary layer thickness is estimated to be approximately 0.5 mm, while the bubble diameters in Figure 7.7 are 200 μm (top), 300 μm (middle) and 600 μm (bottom). This means that the HFSBs are half of the boundary layer thickness for the medium-sized bubbles and are even larger than the boundary layer thickness for the large-sized bubbles. The blue dots indicate the center of the bubbles. Calculating the estimated empty region inside the boundary layer due to the streamtube expansion is not possible, since the boundary layer is not well resolved close to the flat plate surface and since the boundary layer is so thin.

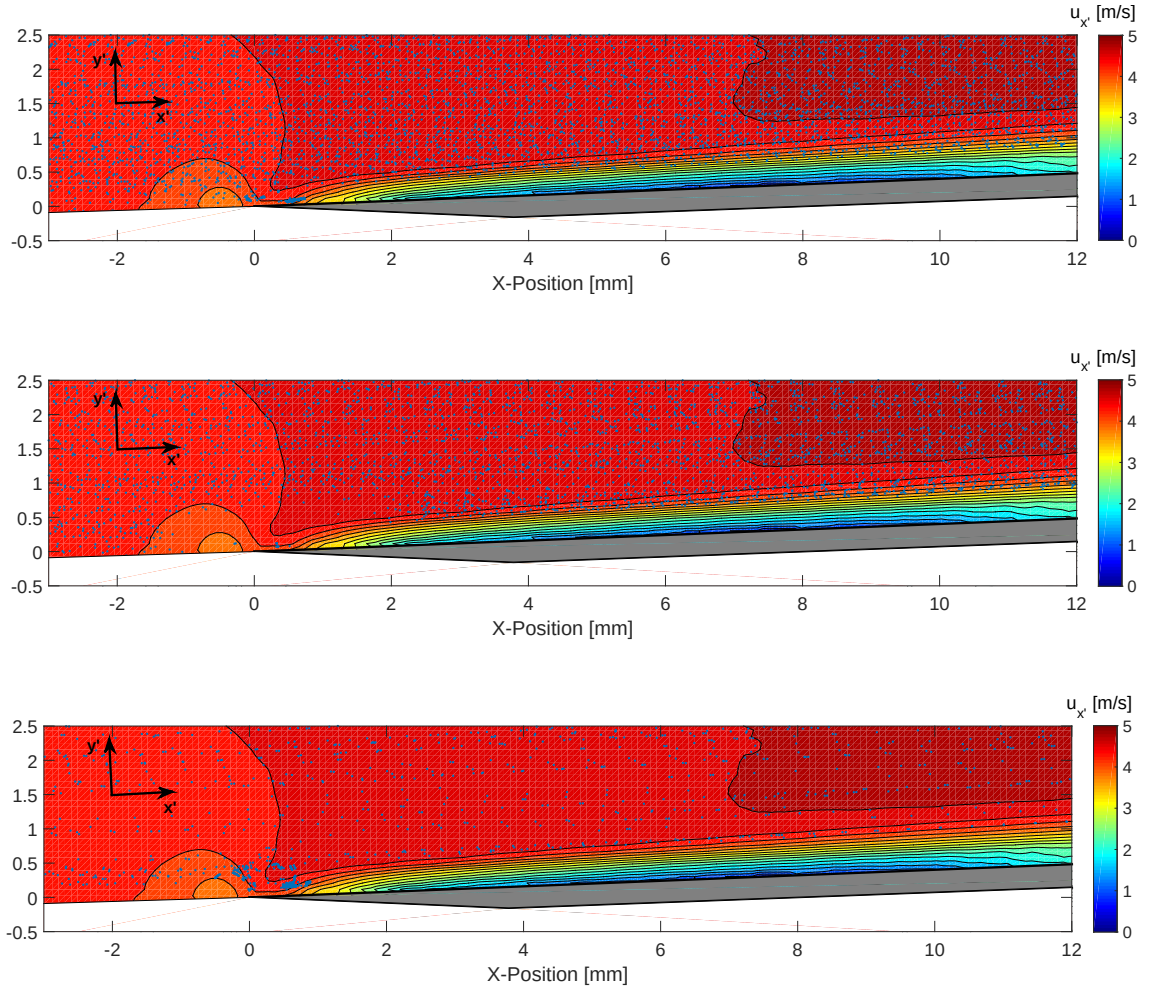

Figure 7.7: HFSBs in a laminar boundary layer at the leading edge. Contour levels are velocity $u_{x'}$ measured by PIV with fog droplets. *Top*: small bubbles (d_p=200 μm). *Middle*: medium bubbles (d_p=300 μm). *Bottom*: large bubbles (d_p=600 μm).

Chapter 8

Conclusion & Recommendations

8.1 Conclusion

A theoretical model is developed to determine the bubble density and production rate, based on the flow rates applied to the fluid supply unit (FSU). This model reveals that the bubble density is independent of the bubble diameter and is a function of solely the volume flow rate ratio of helium and bubble fluid solution. Furthermore, the production rate is estimated in function of the bubble diameter. A theoretical model that allows to predict the bubble diameter in function of the three fluid flow rates is currently not available, although it is known that the bubble diameter and bubble production rate are mainly dependent on the secondary airflow of the nozzle.

Numerical simulations of the equation of motion at finite Re_p of Mei (1996) are made, under the assumption that HFSBs can be modelled as solid particles. This model is used to estimate the magnitude of the forces acting on the bubbles and to determine which forces are the dominant ones. It is found that the fluid-stress force is dominant and that the drag force at finite Reynolds number cannot be represented by the Stokes drag force. The added-mass force is in general at least two orders of magnitude smaller than the fluid-stress force and has a negligible effect on the bubble trajectory for neutrally buoyant HFSBs. Furthermore, it is used the calculate the tracing fidelity of the HFSBs with different specific densities. Lastly, these simulations are used to determine the validity range of the methodology applied on the experimental data.

High-speed visualizations identify two different operating regimes of the bubble generator. In the bubbling regime, HFSBs are produced in a stable way and the bubbles properties are rather monodispersed. Conversely, the jetting regime is unstable with a broad distribution of the bubble diameter. The latter is measured independently from the distance of the glare points of individual bubbles. The relaxation time was calculated experimentally for the bubbles along the stagnation line of a cylinder as the ratio of slip velocity over particle

acceleration. Through measurements of the relaxation time and the bubbles diameter, the density of HFSBs was computed. Both stable and unstable production regimes were detected in the results. When the bubble generators operate in a stable production regime, variations of the bubble diameter below 5% are observed. For neutrally buoyant bubbles, the mean value of the relaxation time is of the order of 10 μs, which agrees well with the previous results of Scarano et al. (2015). However, even in these conditions, the standard deviation of the relaxation time exceeds 30 μs. When the bubbles production regime is unstable, the standard deviation of the bubble diameter and relaxation time can be as high as 70 μm and 50 μs, respectively. These results indicate that the current bubble production systems yield HFSBs allowing accurate measurements of the time-averaged velocity field. Conversely, caution should be taken concerning the accuracy of the instantaneous and fluctuating flow properties, which are directly linked to the spread of the relaxation time of individual bubbles and strongly depends upon the time scales of the specific flow that is investigated. The applied methodology shows agreements with the theoretical model for HFSBs close to the neutral buoyancy condition, but has deviations of over 30 % in the relaxation time and specific density for non-neutrally buoyant bubbles and air-filled soap bubbles.

In a second experiment helium-filled soap bubbles were used as flow tracers in a laminar boundary on top of a flat plate. An empty region close the flat plate surface is observed for three HFSBs with different diameters. The height of this empty region is a function of the bubble diameter and can partly be explained by the conservation of mass principle of a streamtube far upstream that expands inside the boundary layer. However, the other part of this empty region can most likely be explained by a transverse lift force due to the strong shear and increases for larger particles.

8.2 Recommendations

During the time frame of this project, significant advancements were made by both LaVision GmbH as the aerodynamics department of TU Delft in the design of the bubble generators. The stability of the nozzles is much improved compared to the experiments performed in this work. Therefore, it is recommended for the final, stable operating nozzle design to:

- Create a detailed mapping of the influence of the all the flow rates on the bubble diameter and production rate (in the whole operating range of the nozzle). This can be achieved with high speed flow visualization (shadowgraphy). This investigation can be combined by examining under which conditions the nozzle works in bubbling and jetting regime or does not work at all and as such map the full operating range of the nozzle.

- Perform a repetition of the experiment described in this work in a wind tunnel with lower turbulence level. The turbulence level is shown to cause some significant dispersion in the data. Reference data should be preferably time-resolved and simultaneously taken together with the bubble recordings. The latter forms a challenge to record the reference solution with fog droplets, without having saturated bubbles in the images. The state-

of-the art 'Shake-the-box' algorithm can be used to process the reference solution. As such, the equation of motion of the HFSBs can possibly be solved for the bubble density, eliminating the methodology applied in this work. Furthermore, more samples in the operating range should be taken to allow accurate mapping of the influence of each FSU flow rate on the HFSBs on the relaxation time and bubble density.

- Investigate the bubble forming process inside the nozzle. Literature already reports on the production of bubbles in a co-flow configuration with two fluids, but little is known about the same process with three fluids. This can be done by flow visualization inside the nozzle and by numerical simulations of the processes inside the nozzles. The latter can be used as well to optimize the nozzle design and reduce the dispersion in stable production.

When the individual nozzle design is completed and is perfected, the individual nozzles should be combined in an aerodynamic rake to increase the particle concentration in the wind tunnel. In this perspective, attention should be paid to:

- The bubble production of all the individual nozzles should be identical. Therefore, the volume flow rates of helium, the bubble fluid solution and the secondary airflow should be identical and should not be affecting each other. This requires as well that the nozzle production process is optimized and delivers identical bubble nozzles.
- The effect of the aerodynamic rake on the wind tunnel quality needs to be investigated, since it causes disturbances in the wind tunnel that might not be fully dissipated in the test section. Moreover, each nozzles has a small jet flow with a velocity of approximately 20 m/s which can affect the overall flow.

This work focussed primary on the aerodynamic behaviour of helium-filled soap bubbles in an incompressible and irrotational flow field. In a next step, its tracing fidelity in turbulence needs to be investigated. It is of huge importance to know which turbulent scales can be correctly traced by HFSBs and whether the bubbles might filter out some eddies due to their delayed reaction or due their larger size.

Bibliography

R.J. Adrian. Particle-Imaging Techniques for Experimental Fluid Mechanics. *Annual Review of Fluid Mechanics*, 23(1):261–304, 1991.

R.J. Adrian and J. Westerweel. *Particle Image Velocimetry*. Cambridge University Press, 2010.

R.J. Adrian and C-S Yao. Pulsed laser technique application to liquid and gaseous flows and the scattering power of seed materials. *Applied Optics*, 24(1):44–52, 1985.

ANSYS Fluent Inc. *ANSYS Fluent Theory Guide*. ANSYS, Canonsburg, United States of America, 2013.

C. Atkinson, S. Coudert, J-M Foucaut, M. Stanislas, and J. Soria. The accuracy of tomographic particle image velocimetry for measurements of a turbulent boundary layer. *Experiments in Fluids*, 50:1031–1056, 2011.

T.R. Auton, J.C.R. Hunt, and M. Prud'Homme. The force exerted on a body in inviscid unsteady non-uniform rotational flow. *Journal of Fluid Mechanics*, 197(1):241–257, 1988.

P. Bagchi and S. Balachandar. Effect of free rotation on the motion of a solid sphere in linear shear flow at moderate Re. *Physics of Fluids*, 14(8):2719–2737, 2002.

A.B. Basset. *A treatise on hydrodynamics, with numerous examples*. Deightion, Bell and Company, London, 1888.

G.K. Batchelor. *An Introduction to Fluid Dynamics*. Cambridge University Press, 1967.

J. Bosbach, M. Kühn, and C. Wagner. Large scale particle image velocimetry with helium filled soap bubbles. *Experiments in Fluids*, 46(3):539–547, 2009.

J.V. Boussinesq. Sur la résistance qu'oppose un fluide indéfini au repos, sans pesanteur, au mouvement varié d'une sphère solide qu'il mouille sur toute sa surface, quand les vitesses restent bien continues et assez faibles pour leur carrés et produits soient négligeables. *Comptes Rendu de l'Academie des Sciences*, 100:935–937, 1885.

G.C.A. Caridi, D. Ragni, A. Sciacchitano, and F. Scarano. A seeding system for large-scale Tomographic PIV in aerodynamics. In *11th International Symposium on Particle Image Velocimetry PIV15*, 2015.

D.S. Dandy and H. Dwyer. A sphere in shear flow at finite Reynolds number: effect of shear on particle lift, drag, and heat transfer. *Journal of Fluid Mechanics*, 216:381, 1990.

G.E. Elsinga, F. Scarano, B. Wieneke, and B.W. van Oudheusden. Tomographic particle image velocimetry. *Experiments in Fluids*, 41(6):933–947, 2006.

R. Empey and R. Ormiston. Tail-rotor thrust on a 5.5-foot helicopter model in ground effect. In *American Helicopter Society, 30th Annual National Forum*, 1984.

H. Faxén. Der Widerstand gegen die Bewegung einer starren Kugel in einer zähen Flüssigkeit, die zwischen zwei parallelen ebenen Wänden eingeschlossen ist. *Annalen der Physik*, 373 (10):89–119, 1922.

C. Forbes, M. Evans, N. Hastings, and B. Peacock. *Statistical Distributions*. John Wiley & Sons, Inc., fourth edition edition, 2011.

Y. Fukuchi. Influence of number of cameras and preprocessing for thick volume Tomographic PIV. In *16th International Symposium on Applications of Laser Techniques to Fluid Mechanics*, 2012.

A.M. Gañán-Calvo, Miguel A. Herrada, and P. Garstecki. Bubbling in Unbounded Coflowing Liquids. *Physical Review Letters*, 96(12):124504, 2006.

S. Ghaemi and F. Scarano. Multi-pass light amplification for tomographic particle image velocimetry applications. *Measurement Science and Technology*, 21(12):127002, 2010.

S. Ghaemi and F. Scarano. Counter-hairpin vortices in the turbulent wake of a sharp trailing edge. *Journal of Fluid Mechanics*, 689:317–356, 2011.

R. Hale, P. Tan, and D. Ordway. Experimental investigation of several neutrally-buoyant bubble generators for aerodynamic flow visualization. *Naval Research Reviews*, 24(6):19–24, 1971a.

R. Hale, P. Tan, R. Stowell, and D. Ordway. Development of an integrated system for flow visualization in air using neutrally-buoyant bubbles. Technical report, Sage Action, Ithaca, NY, 1971b.

R.A. Humble, G.E. Elsinga, F. Scarano, and B.W. van Oudheusden. Investigation of the Instantaneous 3D Flow Organization of a Shock Wave / Turbulent Boundary Layer Interaction using Tomographic PIV. *37th AIAA Fluid dynamics Conference and Exhibit*, 2007.

C. Kähler, B. Sammler, and J. Kompenhans. Generation and control of tracer particles for optical flow investigations in air. *Experiments in Fluids*, 33:736–742, 2002.

M.F. Kerho and M.B. Bragg. Neutrally buoyant bubbles used as flow tracers in air. *Experiments in Fluids*, 16(6):393–400, 1994.

P. Klimas. Helium bubble survey on an opening parachute flowfield. *Journal of Aircraft*, 10 (9):567–569, 1973.

M. Kühn, K. Ehrenfried, J. Bosbach, and C. Wagner. Large-scale tomographic particle image velocimetry using helium-filled soap bubbles. *Experiments in Fluids*, 50(4):929–948, 2011.

E. Lobutova, C. Resagk, R. Rank, and D. Müller. Extended Three Dimensional Particle Tracking Velocimetry for Large Enclosures. *Notes on Numerical Fluid Mechanics and Multidisciplinary Design*, 106:113–124, 2009.

K.P. Lynch. *Advances in Time-Resolved Tomographic Particle Image Velocimetry.* PhD thesis, TU Delft, 2015.

M. Machacek. *A quantitative visualization tool for large wind tunnel experiments.* PhD thesis, ETH Zürich, 2003.

G. Magnus. Über die Abweichung der Geschosse, und: Über eine abfallende Erscheinung bei rotierenden Körpern. *Annalen der Physik*, 164(1):1–29, 1853.

N. Malik, T. Dracos, and D. Papantoniou. Particle Tracking Velocimetry in 3-Dimensional Flows .2. Particle Tracking. *Experiments in Fluids*, 15:279–294, 1993.

J.S. Marshall and S. Li. *Adhesive Particle Flow.* Cambridge University Press, 2014.

M.R. Maxey and J.J. Riley. Equation of motion for a small rigid sphere in a nonuniform flow. *Physics of Fluids*, 26(4):883–889, 1983.

J.B. McLaughlin. Inertial migration of a small sphere in linear shear flows. *Journal of Fluid Mechanics*, 224:261, 1991.

R. Mei. An approximate expression for the shear lift force on a spherical particle at finite reynolds number. *International Journal of Multiphase Flow*, 18(1):145–147, 1992.

R. Mei. History force on a sphere due to a step change in the free-stream velocity. *International Journal of Multiphase Flow*, 19(3):509–525, 1993.

R. Mei. Velocity fidelity of flow tracer particles. *Experiments in Fluids*, 22(1):1–13, 1996.

A. Melling. Tracer particles and seeding for particle image velocimetry. *Measurement Science and Technology*, 8(12):1406–1416, 1997.

D. Michaelis, R. Bomphrey, P. Henningsson, and D. Hollis. Reconstructing the vortex skeleton of the desert locust using phase averaged POD approximations from time resolved thin volume tomographic PIV. In *16th International Symposium on Applications of Laser Techniques to Fluid Mechanics*, 2012.

D. Müller, B. Müller, and U. Renz. Three-dimensional particle-streak tracking (PST) velocity measurements of a heat exchanger inlet flow. *Experiments in Fluids*, 30(6):645–656, 2001.

R.H.G. Müller, H. Flögel, and T. Scherer. Investigation of large scale low speed air condition flow using PIV. In *9th international symposium on flow visualization (Edinburgh, Scotland)*, 2000.

Y. Okuno, T. Fukuda, Y. Miwata, and T. Kobayashi. Development Of Three-Dimensional Air Flow Measuring Method Using Soap Bubbles. *JSAE Review*, 14(4):50–55, 1993.

E. Pounder. Parachute inflation process Wint-Tunnel Study. Technical report, Equipment Laboratory, Wright-Patterson Air Force Base, Ohio, USA, 1956.

S. Pröbsting, F. Scarano, M. Bernardini, and S. Pirozzoli. On the estimation of wall pressure coherence using time-resolved tomographic PIV This article is part of the topical collection on application of laser techniques to fluid mechanics 2012. *Experiments in Fluids*, 54:1567, 2013.

M. Raffel, C.E. Willert, S. Wereley, and J. Kompenhans. *Particle Image Velocimetry - A Practical Guide*. Springer-Verlag Berlin Heidelberg, Berlin, Heidelberg, 2007.

D. Ragni, F. Schrijer, B.W. van Oudheusden, and F. Scarano. Particle tracer response across shocks measured by PIV. *Experiments in Fluids*, 50:53–64, 2011.

M.H. Redon and M.F. Vinsonneau. Etude de l'écoulement d'une maquette. *Aéronautique*, 18 (204):60–66, 1936.

S.I. Rubinow and J.B. Keller. The transverse force on a spinning sphere moving in a viscous fluid. *Journal of Fluid Mechanics*, 11(03):447, 1961.

P.G. Saffman. The lift on a small sphere in a slow shear flow. *Journal of Fluid Mechanics*, 22(02):385–400, 1965.

P.G. Saffman. The lift on a small sphere in a slow shear flow - Corrigendum. *Journal of Fluid Mechanics*, 31(03):624, 1968.

M. Samimy and S.K. Lele. Motion of particles with inertia in a compressible free shear layer. *Physics Of Fluids*, 3(8):1915–1923, 1991.

F. Scarano. Tomographic PIV: principles and practice. *Measurement Science and Technology*, 24(1):012001, 2013a.

F. Scarano. *Experimental Aerodynamics (lecture notes)*. TU Delft, Delft, The Netherlands, 2013b.

F. Scarano and C. Poelma. Three-dimensional vorticity patterns of cylinder wakes. *Experiments in Fluids*, 47(1):69–83, 2009.

F. Scarano, S. Ghaemi, G.C.A. Caridi, J. Bosbach, U. Dierksheide, and A. Sciacchitano. On the use of helium-filled soap bubbles for large-scale tomographic PIV in wind tunnel experiments. *Experiments in Fluids*, 56(2):42, 2015.

L. Schiller and A. Naumann. Über die gundlegenden Berechungen bei der Schwerkraftaufbereitung. *Zeitschrift des Vereines Deutscher Ingenieure*, 77:318–320, 1933.

J. Schneiders, G.C.A. Caridi, A. Sciacchitano, and F. Scarano. Instantaneous Pressure Measurements from Large-Scale Tomo-PTV with HFSB Tracers past a Surface-Mounted Finite Cylinder. In *AIAA SciTech*, 2016.

A. Schröder, R. Geisler, G.E. Elsinga, F. Scarano, and U. Dierksheide. Investigation of a turbulent spot and a tripped turbulent boundary layer flow using time-resolved tomographic PIV. *Experiments in Fluids*, 44(2):305–316, 2008.

A. Schröder, R. Geisler, A. Sieverling, B. Wieneke, A. Henning, F. Scarano, G.E. Elsinga, and C. Poelma. Lagrangian aspects of coherent structures in a turbulent boundary layer flow using TR-Tomo PIV and FTV. In *8th international symposium on particle image velocimetry*, 2009.

A. Schröder, R. Geisler, K. Staack, G.E. Elsinga, F. Scarano, B. Wieneke, A. Henning, C. Poelma, and J. Westerweel. Eulerian and Lagrangian views of a turbulent boundary layer flow using time-resolved tomographic PIV. *Experiments in Fluids*, 50:1071–1091, 2011.

A. Schröder, D. Schanz, B. Heine, and U. Dierksheide. Transitional flow structures downstream of a backward-facing-step - an investigation using high resolution tomo PIV. In *9th international symposium on PIV (Kobe, Japan)*, 2011.

G. Segré and A. Silberberg. Behaviour of macroscopic rigid spheres in Poiseuille flow Part 2. Experimental results and interpretation. *Journal of Fluid Mechanics*, 14(1):136, September 1962.

A. Sevilla, J.M. Gordillo, and C. Martinez-Bazan. Transition from bubbling to jetting in a coaxial airwater jet. *Physics of Fluids*, 17(1):018105, 2005a.

A. Sevilla, J.M. Gordillo, and C. Martinez-Bazan. Bubble formation in a coflowing airwater stream. *Journal of Fluid Mechanics*, 530:181–195, 2005b. doi: 10.1017/S002211200500354X.

Soapbubble.dk. Bubble science [Soapbubble.dk], 2016. URL http://soapbubble.dk/english/science/.

K. Staack, R. Geisler, A. Schröder, and D. Michaelis. 3D3C-coherent structure measurements in a free turbulent jet 2 . Experimental Setup and Measurement Procedure. In *15th International Symposium on Applications of Laser Techniques to Fluid Mechanics*, 2010.

G.G. Stokes. On the effect of the internal friction of fluids on the motion of pendulums. *Proceedings Cambridge Philosphical Society*, 9:8–106, 1851.

Y. Sun, Y. Zhang, A. Wang, J.L. Topmiller, and J.S. Bennet. Experimental characterization of airflows in aircraft cabins, Part I: Experimental system and measurement procedure. *ASHRAE Transactions*, 111(2):45–52, 2005.

C. Tropea. Optical Particle Characterization in Flows. *Annual Review of Fluid Mechanics*, 43:399–426, 2011.

W.D. Urban and M.G. Mungal. Planar velocity measurements in compressible mixing layers. *Journal of Fluid Mechanics*, 431:189–222, 2001.

H.C. van de Hulst and R.T. Wang. Glare points. *Applied Optics*, 30(33):4755–4763, 1991.

D. Violato, P. Moore, and F. Scarano. Lagrangian and Eulerian pressure field evaluation of rod-airfoil flow from time-resolved tomographic PIV. *Experiments in Fluids*, 50:1057–1070, 2011.

J. Westerweel. Fundamentals of digital particle image velocimetry. *Measurement Science and Technology*, 8(12):1379–1392, 1997.

J. Westerweel and F. Scarano. Universal outlier detection for PIV data. *Experiments in Fluids*, 39(6):1096–1100, 2005.

F. White. *Viscous fluid flow*. McGraw-Hill, United Kingdom, 2005.

Appendix A

Matlab code of particle trajectory simulator

```
%% This programs simulates the motion of a spherical particle in a flowfield around a cylinder.
%  The flowfield is calculated using the potential flow theory around a cylinder.
%  Koen Morias - August 2016 - TU Delft

clear all; close all; clc;
warning('off','all'); format long;

%% Input Parameters
a = 400/2*1e-6;          % Radius of a HFSB [m]
mu_fl = 1.8*1e-5;        % Dynamic Viscosity of fluid (air) [Pa*s]
rho_fl = 1.225;          % Density of fluid (air) [kg/m ]
mp_mfl = 1.02;           % Particle Mass over Fluid Mass Ratio [-]
g = 9.81;                % Gravitational Acceleration [m/s ]
U0 = 30.0;               % Freestream velocity [m/s]
R = 0.040/2;             % Radius of Cylinder in Test Section [m]
x_start = [-10 0.0];     % Start Point Calculation in x/R and y/R [-]
x_end = [-0 5.0];        % Stop Criterium in x/R and y/R [-].
dt = 1e-08;              % Time Step [s]

%% Memory Allocation
fprintf('Starting Memory Allocation & Initialization \n\tCalculating... \n');
Msize = round(2*(x_end(1,1)*R-x_start(1,1)*R)/(U0*dt));
X = zeros(Msize,2);
U = zeros(Msize,2);
V = zeros(Msize,2);
Re = zeros(Msize,1);
Phi = zeros(Msize,1);
t = zeros(Msize,1);
dVdt = zeros(Msize,2);
DUDt = zeros(Msize,2);
F_d = zeros(Msize,2);
F_bg = zeros(Msize,2);
F_am = zeros(Msize,2);
F_fs = zeros(Msize,2);
```

```
35 acc  = zeros(Msize,2);
36
37 tau  = 2/9*a^2*rho_fl*mp_mfl/mu_fl;
38 tau1 = 2/9*a^2*(rho_fl*mp_mfl-rho_fl)/mu_fl;
39
40 %% Initialization
41 X(1,:) = x_start.*R;
42 U(1,:) = PotentialCylinder(X(1,:), R, U0);
43 X(2,:) = X(1,:) + U(1,:)*dt;
44 U(2,:) = PotentialCylinder(X(2,:), R, U0);
45
46 DUDt(2,:) = U(2,:).*(U(2,:)-U(1,:))./(X(2,:)-X(1,:));
47 DUDt(2,isnan(DUDt(2,:))) = 0;
48
49 V(1:2,:) = U(1:2,:)-tau1.*[DUDt(2,:); DUDt(2,:)];
50 Re(1:2,1) = rho_fl.*2.*a.*norm(abs(U(1:2,:)-V(1:2,:)))./mu_fl;
51 t(1:2) = [0 dt];
52 i = 2;
53 fprintf('Ended Memory Allocation & Initialization \n\n');
54
55 %% Calculate Particle Path
56 fprintf('Starting Particle Path Calculation \n');
57 while (sum(X(i,:).^2) > (R + a/2)^2) && (X(i,1) < x_end(1,1)*R) && (abs(X(i,2)
       ) < x_end(1,2)*R) && (abs(V(i,1))>1e-5 || abs(V(i,2))>1e-5);
58
59 dVdt(i,:) = V(i,:).*(V(i,:)-V(i-1,:))./(X(i,:)-X(i-1,:)); % Particle
       acceleration
60 dVdt(i,isnan(dVdt(i,:))) = 0;
61 DUDt(i,:) = U(i,:).*(U(i,:)-U(i-1,:))./(X(i,:)-X(i-1,:)); % Fluid acceleration
62 DUDt(i,isnan(DUDt(i,:))) = 0;
63
64 %% Quasi-Steady Drag Force
65 F_d(i,:) = 18*mu_fl./(mp_mfl.*rho_fl.*(2*a)^2)*(U(i,:)-V(i,:));
66 Phi(i) = 1+0.15*Re(i)^0.687;
67
68 %% Buoyancy-Gravity Force
69 F_bg(i,:) = (mp_mfl-1)/mp_mfl.*[0 -g];
70
71 %% Added-Mass Force
72 F_am(i,:) = 0.5/mp_mfl*(DUDt(i,:) - dVdt(i,:));
73
74 %% Fluid-Stress Force
75 F_fs(i,:) = 1/mp_mfl*(DUDt(i,:));
76
77 %% History Force
78 % Is not included
79
80 %% Update the Velocities and Position
81 acc(i,:) = (F_am(i,:)+F_fs(i,:));
82
83 V(i+1,:) = U(i,:) + exp(-dt/(tau/Phi(i))).*(V(i,:)-U(i,:))-acc(i,:).*(tau/Phi(
       i)).*(exp(-dt/(tau/Phi(i)))-1);
84 X(i+1,:) = X(i,:) + dt.*(U(i,:)+acc(i,:).*(tau/Phi(i)))+(tau/Phi(i)).*(1-exp(-
       dt/(tau/Phi(i)))).*(V(i,:)-U(i,:)-acc(i,:).*(tau/Phi(i)));
85
86 U(i+1,:) = PotentialCylinder(X(i+1,:), R, U0);
87 Re(i+1,1) = norm(U(i+1,:)-V(i+1,:))*2*a*rho_fl/mu_fl;
```

```
88
89  t(i+1,:) = t(i,:) + dt;
90  i = i+1;
91
92  if (i/10000 == round(i/10000))
93      fprintf('\tTime Step: %9.0f \t Particle Position: %7.2f mm %7.2f mm \n', i
            , X(i,:)*1000);
94  end
95
96  end
97  fprintf('Ended Particle Path Calculation \n\n');
98  fprintf('Starting Post-Processing \n\tCalculating... \n');
99
100 %% De-Allocate Memory and reduce data-load
101 indices = find(~t);
102 t(indices(2:end)) = [];
103 X(indices(2:end),:) = [];
104 U(indices(2:end),:) = [];
105 V(indices(2:end),:) = [];
106 Re(indices(2:end),:) = [];
107 dVdt(indices(2:end),:) = [];
108 DUDt(indices(2:end),:) = [];
109 F_d(indices(2:end),:) = [];
110 F_bg(indices(2:end),:) = [];
111 F_am(indices(2:end),:) = [];
112 F_fs(indices(2:end),:) = [];
113 acc(indices(2:end),:) = [];
114 Phi(indices(2:end),:) = [];
```

```
1  function [U] = PotentialCylinder(X, R, U0)
2  % POTENTIALCYLINDER - Calculation of the velocity vector U = [u v] at the
3  % position X = [x y] around a 2D cylinder with radius R with horizontal
       freestream
4  % velocity U0 in cartesian frame using the potential flow theory.
5  % Koen Morias - August 2016 - TU Delft
6
7
8      x = X(1); y = X(2);
9
10     u = +U0*(R^2*(y^2-x^2)+(x^2+y^2)^2)/(x^2+y^2)^2;      % Velocity component
           in x-direction [m/s]
11     v = -U0*2*R^2*x*y/(x^2+y^2)^2;                        % Velocity component
           in y-direction [m/s]
12
13     U = [u v];                                            % Output in vector
           notation
14 end
```